

HYDROTHERMAL SYNTHESIS OF TiO₂ NANOSTRUCTURES FOR
PHOTOCATALITIC AND PHOTOVOLTAIC APPLICATIONS

A THESIS SUBMITTED TO
THE GRADUATE SCHOOL OF NATURAL AND APPLIED SCIENCES
OF
MIDDLE EAST TECHNICAL UNIVERSITY

BY

NURSEV ERDOĞAN

IN PARTIAL FULFILLMENT OF THE REQUIREMENTS
FOR
THE DEGREE OF DOCTOR OF PHILOSOPHY
IN
METALLURGICAL AND MATERIALS ENGINEERING

FEBRUARY 2017

Approval of the thesis:

**HYDROTHERMAL SYNTHESIS OF TiO₂ NANOSTRUCTURES FOR
PHOTOCATALITIC AND PHOTOVOLTAIC APPLICATIONS**

submitted by **NURSEV ERDOĞAN** in partial fulfillment of the requirements for
the degree of **Doctor of Philosophy in Metallurgical and Materials Engineering
Department, Middle East Technical University** by,

Prof. Dr. Gülbin Dural Ünver _____
Dean, Graduate School of **Natural and Applied Sciences**

Prof. Dr. C. Hakan Gür _____
Head of Department, **Metallurgical and Materials Engineering**

Prof. Dr. Abdullah Öztürk _____
Supervisor, **Metallurgical and Materials Eng. Dept., METU**

Prof. Dr. Jongee Park _____
Co-Supervisor, **Metallurgical and Materials Eng. Dept., Atılım Univ.**

Examining Committee Members:

Prof. Dr. Caner Durucan _____
Metallurgical and Materials Engineering Dept., METU

Prof. Dr. Abdullah Öztürk _____
Metallurgical and Materials Engineering Dept., METU

Prof. Dr. Hasan Göçmez _____
Metallurgical and Materials Eng. Dept., Dumlupınar University

Assoc. Prof. Dr. H. Emrah Ünal _____
Metallurgical and Materials Eng. Dept., METU

Assoc. Prof. Dr. Hilal Türkoğlu Şaşmaz _____
Metallurgical and Materials Eng. Dept., Atılım University

Date: 01.02.2017

I hereby declare that all information in this document has been obtained and presented accordance with the academic rules and ethical conduct. I also declare that, as required by these rules and conduct, I have fully cited and referenced all material and results that are not original to this work.

Name, Last name: Nursev Erdoğan

Signature:

ABSTRACT

HYDROTHERMAL SYNTHESIS OF TiO₂ NANOSTRUCTURES FOR PHOTOCATALYTIC AND PHOTOVOLTAIC APPLICATIONS

Erdoğan, Nursev

Ph.D., Department of Metallurgical and Materials Engineering

Supervisor: Prof. Dr. Abdullah Öztürk

Co-Supervisor: Assoc. Prof. Dr. Jongee Park

February 2017, 168 pages

Titanium dioxide (TiO₂) nanostructures with different crystal structures and various morphologies were synthesized by hydrothermal process to utilize them in photocatalytic and photovoltaic applications. The investigations were conducted in three different sets of systematic experimental studies. The first set of experiments was based on the synthesis of TiO₂ nanostructures in the presence of strong sodium hydroxide (NaOH) catalyzer. Temperature and molarity of NaOH were kept constant while hydrothermal reaction duration and precursor materials were changed during syntheses. The nanostructures obtained were in Na-titanate crystal structure, which were protonated for H-titanate and then calcined to get a TiO₂ powder. The synthesized products were characterized using X-ray Diffraction (XRD), Field Emission Electron Microscopy (FESEM), High Resolution Electron Microscopy (HRTEM), Differential Thermal Analysis (DTA) and Thermogravimetric Analysis (TGA) techniques. Photocatalytic properties of nanostructures were investigated using of methylene blue degradation in aqueous solution by a UV-Vis spectrophotometer. Best photoactivity was recognized in the products obtained when amorphous TiO₂ powders were used as precursor. Two of the powders with different morphologies were mixed to practice this mixture in the fabrication of dye-sensitized solar cell (DSSC).

The second set of experiments was performed using nitric acid (HNO_3) catalyzer to synthesize TiO_2 powder in one step. Various hydrothermal synthesis temperatures, durations, and acid concentrations were employed to obtain powders with different morphologies and crystal structures. Synthesized powders were characterized using FESEM, HRTEM, and XRD. An evolution mechanism was proposed for the resultant TiO_2 powders. Four different powders in terms of crystal structure and morphology were selected for the fabrication of DSSCs.

The third set of experiments was conducted to enhance the photoactivity of powders synthesized by HNO_3 catalyzed hydrothermal process via doping by iron (Fe) and/or molybdenum (Mo). It was realized that nitrogen (N) also doped into the TiO_2 structure as a third dopant during co-doping of Fe and Mo. Mono-, co-, and triple- doped TiO_2 powders were characterized using FESEM, XRD, HRTEM, X-ray Photoelectron Spectroscopy (XPS), Inductively Coupled Plasma Mass Spectroscopy (ICP-MS), and Brauner Emmett Teller (BET) surface area analyses. Doping caused to evolve rutile structure instead of anatase. Results revealed that photoactivity of rutile structure was enhanced by triple-doping.

Selected powders were used in the preparation of a paste for the photoanode component of DSSC. Photoanodes were characterized using UV-Vis spectrophotometer, surface profilometer, FESEM, XRD and Electrochemical Impedance Spectroscopy (EIS). Photovoltaic measurements revealed that best efficiency (2.86 %) among single layer photoanodes could be harvested by the photoanode composed of anatase and a small amount of rutile crystals. By titanium chloride (TiCl_4) treatment efficiency increased to 4.86 %. The highest efficiency harvested was 4.26 % by bi-layer photoanodes built using anatase and rutile electrode as down layer and another anatase and rutile electrode with different ratio as top layer.

Keywords: TiO_2 , hydrothermal process, doping, photocatalytic, dye-sensitized solar cells.

ÖZ

FOTOKATALİTİK VE FOTOVOLTAİK UYGULAMALAR İÇİN TiO₂ NANOYAPILARIN HİDROTERMAL SENTEZİ

Erdoğan, Nursev

Doktora, Metalurji ve Malzeme Mühendisliği Bölümü
Tez Yöneticisi: Prof. Dr. Abdullah Öztürk
Yardımcı Tez Yöneticisi: Doç. Dr. Jongee Park

Şubat 2017, 168 sayfa

Farklı kristal yapılarına ve çeşitli morfolojilerdeki titanyum dioksit (TiO₂) nanoyapılar fotokatalitik ve fotovoltaik uygulamalarda kullanılmak üzere hidrotermal yöntemle sentezlendi. Araştırmalar üç farklı sistematik deneysel çalışma serisi oluşturularak yapıldı. İlk deney serisi TiO₂ nanoyapıların kuvvetli sodyum hidroksit (NaOH) katalizörle sentezlenmesi esasına dayanmaktadır. Deneyler sırasında sıcaklık ve NaOH molaritesi sabit tutulurken hidrotermal reaksiyon süresi ve başlangıç prekürsör malzemeleri değiştirildi. Elde edilen nanoyapılar Na-titanat kristal yapısındaydılar. Bu yapılar protone edilerek H-titanat haline getirildikten sonra kalsine edilerek TiO₂ tozuna dönüştürüldü. Sentezlenen ürünler X-ışınları kırınımı (XRD), yüksek çözünürlüklü taramalı elektron mikroskobu (FESEM), yüksek çözünürlüklü geçirimli elektron mikroskobu (HRTEM), Diferensiyal Termal Analiz (DTA) and Termogravimetrik Analiz (TGA) teknikleriyle karakterize edildi. Nanoyapıların fotokatalitik özellikleri sulu çözeltideki metilen mavisinin parçalanma testi ile UV-Vis spektrofotometre kullanılarak belirlendi. En iyi fotokatalitik aktivite amorf başlangıç tozu kullanılarak elde edilen ürünlerde görüldü. Farklı morfolojideki iki toz karıştırılarak boya duyarlı güneş gözesi (DSSC) üretiminde denendi.

İkinci deney serisi nitrik asit (HNO₃) katalizör kullanılarak tek adımda TiO₂ üretimi için yapıldı. Farklı morfoloji ve kristal yapıda tozları elde etmek amacıyla

çeşitli hidrotermal sentez sıcaklıkları, süreleri, ve asit konsantrasyonları uygulandı. Sentezlenen tozlar FESEM, HRTEM ve XRD analiz teknikleri kullanılarak karakterize edildi. Elde edilen TiO_2 nanoyapılar için bir oluşum mekanizması önerildi. Morfolojileri ve kristal yapıları farklı olan dört toz DSSC üretiminde kullanılmak üzere seçildi.

Üçüncü deney serisi HNO_3 katalizörü kullanılarak hidrotermal yöntemle sentezlenen tozlara demir (Fe) ve/veya molibden (Mo) katkılanması suretiyle fotokatalitik aktivitelerinin artırılması için tasarlandı. Fe ve Mo'nun birlikte katkılanması sırasında azot'un (N) yapıya üçüncü bir katkı olarak girdiği fark edildi. Tek, birlikte ve üçlü katkılanmış tozlar FESEM, XRD, HRTEM, X-ışınları spektrofotometresi (XPS), indüktif olarak eşleştirilmiş plazma kütle spektrometresi (ICP), ve Brauner Emmett Teller (BET) yüzey alanı analizleriyle karakterize edildi. Katkılama anataz yerine rutil kristal yapının oluşmasına neden oldu. Sonuçlar rutil yapıdaki tozların fotoaktivitesinin üçlü katkılama ile artırıldığını ortaya koydu.

Seçilen tozlar DSSC'nin fotoanot bileşeni olarak macun hazırlanmasında kullanıldı. Fotoanotlar UV-Vis spektrofotometre, yüzey profilometresi, FESEM, XRD ve elektrokimyasal empedans spektrometre (EIS) analizleriyle karakterize edildi. Fotovoltaik ölçümleri tek katmanlı elektrotlar arasında en yüksek verimin (% 2,86) anataz ve az rutil karışımı fotoanotla sağlandığını gösterdi. Titanyum klorür ($TiCl_4$) işlemiyle verim % 4,86'e yükseldi. Çift katmanlı fotoanotlar arasında en yüksek verim anataz ve rutil karışımı alt katman üzerine farklı oranda anataz rutil karışımı üst katman uygulanmasıyla % 4,26 olarak ölçüldü.

Keywords: TiO_2 , hidrotermal proses, katkılama, fotokatalitik, boya duyarlı güneş gözesi

To my family,

ACKNOWLEDGEMENTS

Foremost, I would like to take this opportunity to express my sincerest gratitude to my thesis advisor, Prof. Dr. Abdullah Öztürk, for his immense knowledge, invaluable guidance, patience, and support during the course of this work. I also thank to my thesis co-advisor Assoc. Prof. Dr. Jongee Park who never ever complain but instead always find a solution for my never ending help requests with his extremely positive humor and creativity.

The members of my thesis supervising committee, Assoc. Prof. Dr. Emrah Ünal and Assoc. Prof. Dr. Hilal Şaşmazel have given their precious time and expertise to improve my work. I must thank them for their encouragement and insightful comments which helped me a lot for every step of my work. I also want to thank my thesis defense committee members Prof. Dr. Caner Durucan and Prof. Dr. Hasan Göçmez for the valuable time they allocated to evaluate my thesis.

My special thanks go to Prof. Dr. H. Aygül Yeprem, Prof. Dr. Cihangir Duran, Prof. Dr. İshak Karakaya, Prof. Dr. Hasan Göçmez and Assist. Prof. Dr. Volkan Kalem whose benevolent methodical approaches, technical support and advice were particularly important for me and have to be highly appreciated.

The technical assistance and suggestions of Serkan Yılmaz, Oğuz Daldal, and Nilufer Atak are also gratefully acknowledged.

I am grateful to my lovely friends Dilhun Örsler, Serpil Solum, Fatmagül Öztoprak, Özge Aytaş, Pelin Ergül and all friends in Gaziosmanpaşa Rotaract Club, which they supported and helped me prepare this thesis; and for conversations that clarified my thinking on this and other matters.

I thank my lab mates and other friends in the department Şahin Coşkun, Melis Kaplan, Şerif Kaya, Sıtkı Can Akkuş, Mustafa S. Aras, Derya Kapusuz, Taha Altıparmak, Burak Ertuş, Ziya Çağrı Torunoğlu, Başak Aysin and Lütfi Ağartan

for their help and comments that encouraged me to revise and improve my studies. I am also grateful to Seher etin and zge Bayraklı for technical assistance.

Last but not the least; I am deeply indebted to my husband Assist. Prof. Dr. Metehan Erdođan who really contributed to every stage of the study with his maximum effort and supported me both academically and emotionally. I am also always thankful to my mother Hatice Bilgin, my father Prof. Dr. Ali Bilgin, my brother Hseyin Bilgin and my cat Paŗa for their never-ending love and spiritual support.

TABLE OF CONTENTS

ABSTRACT.....	v
ÖZ.....	vii
ACKNOWLEDGEMENTS.....	x
LIST OF FIGURES.....	xvi
LIST OF TABLES.....	xxii
CHAPTERS	
1. INTRODUCTION.....	1
1.1 Objectives and outline of the study.....	3
2. OVERVIEW.....	7
2.1 Solar cells.....	7
2.2 Solar cell terminologies.....	8
2.3 Dye sensitized solar cell (DSSC).....	11
2.3.1 History.....	11
2.3.2 Operation mechanism.....	11
2.3.3 Excitation.....	12
2.3.4 Injection.....	13
2.3.5 Diffusion in semiconductor layer.....	13
2.3.6 Iodine reduction.....	13
2.3.7 Dye regeneration.....	14
2.3.8 Electrochemical Impedance Spectroscopy (EIS) of DSSC.....	14
2.3.9 Components of DSSC.....	15
2.3.10 Deposition of mesoporous oxide semiconductor layer onto TCO.....	18
2.3.11 Semiconductor photoanode materials used in DSSC.....	19

2.4 Titanium dioxide (TiO ₂) properties and synthesis	19
2.4.1 One dimensional TiO ₂ and titanate related nanostructures	23
2.4.2 Hydrothermal synthesis of TiO ₂ nanostructures using acid catalyzer	29
2.4.3 Doping of TiO ₂ nanostructures with metal and nonmetals	32
2.4.4 Application of TiO ₂ in DSSC	36
3. EXPERIMENTAL	39
3.1 Powder synthesis via hydrothermal method	39
3.1.1 Base assisted hydrothermal synthesis	39
3.1.2 Acidic hydrothermal synthesis	43
3.2 DSSC assembly	46
3.2.1 Photoanode preparation	47
3.2.2 Counter electrode preparation	50
3.2.3 Cell fabrication	50
3.3 Powder and electrode characterization and property measurement	51
3.3.1 X-ray diffraction (XRD) analysis	51
3.3.2 Field emission scanning electron microscopy (FESEM)	52
3.3.3 High resolution transmission electron microscopy (HRTEM)	52
3.3.4 Braunner - Emmett - Teller (BET) surface area analysis	53
3.3.5 Inductively coupled plasma mass spectrometry (ICP-MS) analysis	53
3.3.6 X-ray photoelectron spectroscopy (XPS) Analysis	53
3.3.7 Differential thermal analysis (DTA) and Thermogravimetric Analysis (TGA)	54
3.3.8 UV-Vis Spectrophotometer and Methylene Blue (MB) Photodegradation Test	55
3.3.9 I-V measurements of DSSCs	57
3.3.10 EIS measurements of DSSCs	57
4. RESULTS and DISCUSSION: SYNTHESSES of ONE DIMENSIONAL TITANATE and TiO ₂ NANOSTRUCTURES, THEIR CHARACTERIZATION and PHOTOACTIVITY	59
4.1 General	59

4.1.1 XRD analysis	60
4.1.2 EDS analysis	67
4.1.3 Morphological analysis.....	69
4.1.4 Thermal analysis	79
4.1.5 Photocatalytic activity.....	81
5. RESULTS AND DISCUSSION: HYDROTHERMAL SYNTHESSES OF TiO ₂ NANOSTRUCTURES USING ACID CATALYZER.....	85
5.1 General.....	85
5.1.1 XRD analysis	85
5.1.2 Morphological analysis.....	93
5.1.3 Evolution Mechanism of TiO ₂ nanostructures.....	102
5.1.4 Photocatalytic activity of powders.....	105
6. RESULTS and DISCUSSION: MONO-, CO- and TRIPLE-DOPING of TiO ₂ NANOSTRUCTURES with Mo, Fe and N	107
6.1 General.....	107
6.1.1 XRD analysis	107
6.1.2 ICP and XPS analysis	111
6.2 Microstructural analysis.....	115
6.2.1 UV-Vis spectrophotometer and methylene blue photo-degradation test.....	119
7. RESULTS AND DISCUSSION: APPLICATION of TiO ₂ NANOSTRUCTURES in DSSC	123
7.1 General.....	123
7.2 Photoanode characterization.....	124
7.2.1 Thickness of TiO ₂ films and dye loading	124
7.2.2 XRD analysis of TiO ₂ films.....	127
7.2.3 FESEM analysis.....	129
7.2.4 UV-vis spectrophotometer	136
7.3 Photovoltaic and EIS measurements.....	137
8. CONCLUSIONS	145
8.1 Syntheses of one dimensional titanate and TiO ₂ nanostructures	145

8.2 Hydrothermal syntheses of TiO ₂ nanostructures using acid catalyzer.....	145
8.3 Mono-, co- and triple-doping of TiO ₂ nanostructures with Mo, Fe and N	146
8.4 Application of TiO ₂ nanostructures in DSSC	146
9. FUTURE WORKS	147
BIBLIOGRAPHY	149
CURRICULUM VITAE	165

LIST OF FIGURES

FIGURES

Figure 2.1 Record efficiencies for different types of solar cells in the world [30]...8	8
Figure 2.2 Solar cell equivalent circuit [31].9	9
Figure 2.3 Basic device components and electronic band alignments for DSSC [37].....12	12
Figure 2.4 Crystal structures of TiO ₂20	20
Figure 2.5 A timeline describing the development of TiO ₂ related nanotubular structure [94].....24	24
Figure 2.6 a) Typical XRD pattern of Na ₂ Ti ₃ O ₇ and (b) Crystal structure of Na titanate [109].....26	26
Figure 2.7 Mechanism of TiO ₂ photocatalysis: hv ₁ : pure TiO ₂ ; hv ₂ : metal-doped TiO ₂ and hv ₃ : nonmetal-doped TiO ₂ [156].33	33
Figure 2.8 Schematic representation of the band structure of pure and N-doped anatase and rutile TiO ₂ [92].....35	35
Figure 3.1 Schematic illustration of 1 D TiO ₂ synthesis following titanate production by base assisted hydrothermal synthesis.40	40
Figure 3.2 Some of the products synthesized by hydrothermal treatment.....41	41
Figure 3.3 Flowchart showing synthesis of TiO ₂ nanostructures by acid assisted hydrothermal process.44	44
Figure 3.4 Cells prepared for efficiency analysis.51	51
Figure 3.5 Equivalent circuit model used for fitting EIS data [208].58	58

Figure 4.1 XRD patterns of samples (a) P36-0, (b) 36-0, and (c) A36-0.	60
Figure 4.2 XRD patterns of samples (a) P36-2 (b) 36-2 (c) A36-2.	62
Figure 4.3 XRD patterns of samples (a) P6-2, (b) P12-2, (c) P36-2, (d) P48-2, and (e) P60-2.....	64
Figure 4.4 XRD patterns of samples (a) 36-2, (b) 36-3, (c) 36-4.	65
Figure 4.5 XRD patterns of samples calcined at 450 °C (a) PC36-2, (b) C36-2, and (c) AC36-2.	66
Figure 4.6 XRD patterns of calcined nanostructure after several protonation (a) PC24-0, (b) PC24-1, (c) PC24-2, and (d) PC24-3.	67
Figure 4.7 EDS spectra of samples (a) P36-0, (b) P36-1, (c) P36-2.....	68
Figure 4.8 Representative FESEM images of samples (a) P12-0, (b) P12-2, (c) 12- 2, (d) 24-2, (e) A24-2, (f) A36-2.....	69
Figure 4.9 FESEM images showing the dissolved aggregates synthesized using different precursors for samples (a) P6-2, (b) 6-2, (c) A6-2.....	71
Figure 4.10 FESEM images of nanostructures synthesized using P25 powder as precursor (a) P12-2, (b) P24-2, (c) P36-2, (d) CP36-2.	72
Figure 4.11 FESEM images of powders synthesized using anatase precursor (a) 12-2, (b) 24-2, (c) 36-2, (d) C36-2.....	74
Figure 4.12 FESEM images of powders synthesized using amorphous precursor (a) A12-2, (b) A24-2, (c) A36-2, (d) AC48-2.	74
Figure 4.13 HRTEM images of sample P36-0 (a) tube image, (b) lattice fringes of tubular structure, (c) Lattice fringes of sheet structure (d) SAED pattern taken from tubes and sheets.....	76

Figure 4.14 HRTEM images of sample P36-2 (a) General image of sample P36-2, (b) lattice fringes parallel to growth direction, (c) lattice fringes perpendicular to growth direction, (e) SAED analysis.	76
Figure 4.15 Ribbon structure of sample PC36-2 (a) Fringes of unit structure, (b) agglomerated ribbons in different diameter and length, (c) stacked ribbons with fringes, (d) SAED pattern of sample.....	77
Figure 4.16 Representative high resolution EDS spectra of sample PC36-2.	78
Figure 4.17 DTA (μV), TG (μg) and DTG ($\mu\text{g}/\text{min}$) curves of sample (a) P36-2, (b) 36-2, and (c) A36-2.....	80
Figure 4.18 Absorbance spectra of solutions containing MB and (a) P36-0, (b) P36-2, (c) PC36-2, (d) P36-0, (e) 36-2, (f) C36-2, (g) A36-0, (h) A36-2, and (i)AC36-2.....	82
Figure 4.19 Variation in concentration of methylene blue with respect to time.....	83
Figure 4.20 Band gaps as calculated by Kubelka Munk transformation of absorption data of the samples synthesized using (a) P25, (b) anatase, and (c) amorphous precursor.....	83
Figure 5.1 XRD patterns of samples synthesized using 1 M acid catalyzer at (a) 110 °C, (b) 140 °C, (c) 180 °C, for different durations, 3 M acid catalyzer at (d) 110 °C, (e) 140 °C, (f) 180 °C for different durations, and 8 M acid catalyzer at (g) 110 °C, (h) 140 °C, (i) 180 °C for different durations.....	86
Figure 5.2 XRD patterns of (a) sample N800, inset shows photograph of precipitated powder, (b) H-titanate nanoribbons inset shows FESEM image of nanoribbons.....	91
Figure 5.3 XRD patterns of samples N843 and HN843.	92

Figure 5.4 FESEM images of powders synthesized using 1 M acid catalyzer at (a) 110 °C for 3 h, (b) 140 °C for 3 h, (c) 140 °C 6 h, (d) 180 °C for 1 h.....	94
Figure 5.5 FESEM images of samples synthesized using 3 M acid catalyzer at (a) 110 °C for 1 h, (b) 110 °C for 6 h, (c) 140 °C for 3 h, (d) 140 °C for 6 h, (e) 180 °C for 3 h, and (f) 180 °C for 6 h.	95
Figure 5.6 FESEM images of samples (a) N811, (b) N813, (c) N816, (d) N841, (e) N843, (f) N846, (g) N881, (h) N883, and (i) N886.	97
Figure 5.7 HRTEM image anatase, rutile and brookite region of sample N116 showing anatase, rutile and brookite region. Inset is the SAED pattern.....	98
Figure 5.8 HRTEM image of sample N386 (b) Bright field image of powder inset SAED pattern showing (111) family of rutile (004) family of anatase.	100
Figure 5.9 HRTEM images of sample N843 showing (a) general view, (b) rods, (c) fringes, (d) magnified view of the selected area given in (c) and inset image SAED pattern (diffraction planes are shown in Table 2), (e) growth of rutile on anatase, (f) view of the selected area in (e).	101
Figure 5.10 HRTEM images of sample powder HN843 (a) lattice fringes on the rods above picture histogram taken from the image, and (b) whole structure of one grain of sample HN843 consisting of small crystallizes.....	102
Figure 5.11 Absorbance spectra of solutions containing MB and powders.	106
Figure 6.1 XRD patterns of un-doped, mono-doped and co-doped powders.	108
Figure 6.2 XPS spectra of powders Mo ₀ Fe ₀ , Mo ₁ Fe ₀ , and Mo ₂ Fe _{0.5} (a) Ti2p, (b) O1s, (c) Mo3d, and (d) Fe2p.....	112
Figure 6.3 N1s XPS spectra of samples.....	114
Figure 6.4 FESEM images of powders (a) Mo ₀ Fe ₀ , (b) Mo ₁ Fe ₀ , (c) Mo ₂ Fe ₀ , (d) Mo ₂ Fe _{0.5} , (e) Mo ₂ Fe ₁	116

Figure 6.5 HRTEM images of un-doped and co-doped powders (a) Mo ₀ Fe ₀ , (b) Mo ₂ Fe _{0.5} , (c) lattice fringes of unit rod in Mo ₂ Fe _{0.5} , (d) lattice fringes of edge of unit rod in Mo ₂ Fe _{0.5} inset shows SAED pattern, (e) lattice fringes of unit rod in sample Mo ₂ Fe ₁ , inset shows SAED pattern, and (f) enlarged rods of Mo ₂ Fe ₁	117
Figure 6.6 EDS analysis of sample Mo ₂ Fe ₁	118
Figure 6.7 UV-visible absorption spectra and Kubelka-Munk transformed band gaps of samples (a) Mo ₀ Fe ₀ , (b) Mo ₁ Fe ₀ , (c) Mo ₂ Fe ₀ , (d) Mo ₂ Fe _{0.5} , and (e) Mo ₂ Fe ₁	119
Figure 6.8 Variation of MB degradation rate with respect to UV exposure time and absorption curves of samples after 90 min UV exposure.	121
Figure 7.1 Thickness of coatings in different layers (a) single layer PN846, (b) bi-layer PN846 and PHN843, (c) single layer P1-2D, and (d) single layer PHN843.	125
Figure 7.2 (a) Absorbance of dye solutions with different molarities in a particular range of light spectrum and (b) Change in absorbance at 532 nm of dye solutions with changing molarities.....	126
Figure 7.3 XRD patterns of semiconductor layers sintered at 500 °C (a) PN116, (b) P1-2D, (c) PN846, (d) PHN843, and (e) PN843.....	128
Figure 7.4 FESEM images of (a) paste PN846 prepared by using Pechini method, (b) Surface of the film, (c) paste PN846 prepared by Grätzel approach, (d) surface of the film.....	130
Figure 7.5 Cross section of semiconductor layer obtained by PN843 inset image surface morphology of coating.	131
Figure 7.6 FESEM images taken from two different regions (a) cross section of paste P1-2D, (b) morphology of P1-2D, (c) cross section of paste P1-2D, (d) morphology of paste P1-2D.....	132

Figure 7.7 FESEM images of (a) PN116 (b) PHN843 inset image cross section view of the coating (c) cross section of PN116 (d) PN846-p pechini with decreased viscosity.	133
Figure 7.8 FESEM images of PN846-t (a) general surface view, (b) High magnification surface morphology, (c) thickness of paste with cross section view, and (d) low magnification view of the surface.	135
Figure 7.9 Bi-layer photoanodes (a) PN846-P1-2D, (b) PN846-PN116 (c) N846-PN843.	135
Figure 7.10 Transmission spectra of single layered pastes (a) PHN843, (b) PN843, (c) PN846, (d) PN116, (e) P1D and (f) P2D.....	137
Figure 7.11 J-V curves of DSSCs with single layer photoanode.....	137
Figure 7.12 J-V curves of DSSCs built by composite pastes.	140
Figure 7.13 Nyquist plots of DSSCs built by different pastes (a) P1-2D, PN116, PN843, PHN843, (b) PN846, PN846-t, PN846-p, (c) PN846-PHN843, P1-2D-PHN843, PN86-PN843, PN846-P1-2D, (d) PN846-PN843 signal enlarged view (dots represent fitting curve while solid lines represent raw data).	142

LIST OF TABLES

TABLES

Table 2.1 Classification of structural properties of anatase, rutile and brookite using the Pseudopotential Hartree-Fock (PHF) calculations [85].	20
Table 2.2 Physical properties of anatase and rutile [88].	21
Table 2.3 Phase variations using base assisted hydrothermal process, crystal structure and some of the diffraction angles [95].	25
Table 3.1 Supplier and product number of chemicals used for synthesis of the nanostructures.	40
Table 3.2 Coding of the samples with respect to their synthesis procedure.	42
Table 3.3 Supplier and product number of chemicals used for synthesis.	43
Table 3.4 Sample coding in terms of their synthesis conditions.	45
Table 3.5 Code of Mo and Fe doped TiO ₂ powders.	46
Table 3.6 Materials used for DSSC fabrication.	47
Table 3.7 Coding of pastes according to powder content and formation method.	48
Table 3.8 Heat treatment program used for the sintering of pastes.	49
Table 4.1 SAED analysis data for sample PC36-2.	78
Table 4.2 Band gaps of samples calculated by Kubelka Munk transformation of absorption data.	84
Table 5.1 Phase share and crystallite size of selected powders.	88
Table 5.2 Data obtained from SAED analysis of sample N843.	101

Table 6.1 Codes, crystal structures, crystallite size values and BET surface area of the samples.....	110
Table 6.2 Crystallographic data of the powders synthesized.....	110
Table 6.3 Bulk and surface elemental compositions according to ICP and XPS analyses of powders.....	112
Table 6.4 MB degradation rate after 90 min UV illumination, and band gaps as determined by using the Kubelka-Munk transformation of absorption data.	120
Table 7.1 Thickness and dye loading amounts of the cells.....	127
Table 7.2 Crystal structure, weight percentages of phases and crystallite size. ...	128
Table 7.3 Data obtained by solar simulator measurements for 1 cm ² exposed area.	138
Table 7.4 Data of cells built by paste composites obtained by solar simulator measurements for 1 cm ² exposed area.	141
Table 7.5 Fitted resistances for EIS measurements of electrodes.....	142

CHAPTER 1

INTRODUCTION

Worldwide energy consumption mostly depends on fossil fuels like oil, gas, or coal. However, the reserve of fossil fuels is limited while the demand for energy is still on the rise. Environmental hazardous of fossil fuels that causes climate change by CO₂ emission is another issue making the source disadvantageous. Thus, there is a pressing challenge to develop new strategies for clean energy. The next generation of clean energy needs to be safe, environmentally friendly, and low-cost to harvest. Nuclear energy, wind energy, and solar energy have attracted enormous research interests and become potential candidates for solving the current energy crisis. When the three types of energy are compared, nuclear energy is rather unsafe and the nuclear plants are very expensive to build. On the other hand, wind energy is time dependent and needs lots of maintenance for the facilities of high cost. Direct conversion of solar energy to electrical energy is the best approach to overcome the current heavy dependence on fossil fuels. Sunlight delivers 4.3×10^{20} J energy to earth in one hour. This giant energy is very attractive for energy demand of the world that is 4.1×10^{20} for one year in 2001 [1]. Solar energy conversion techniques, such as photovoltaic cells among the best candidates for the next generation energy.

Dye-sensitized solar cell (DSSC) is considered to be the most promising candidate among various types of solar cells such as Si solar cells, thin film solar cells and organic solar cells, achieving a high efficiency with low cost [2]. The highest efficiency reported for DSSCs is 13 % [3, 4]. In a typical dye-sensitized solar cell, the excited electrons were generated in the sensitizer/dye molecule, then collected by the semiconductor and transferred to the counter electrode [5]. The semiconductor layer plays two roles in DSSCs. It allows excited electrons to be injected from the dye molecule; and it provides a pathway to transfer the electron

through the Fluorine doped tin oxide (FTO). Titania (TiO_2) is the most widely used semiconductor material for DSSCs, because its conduction band position allows the electrons to be quickly injected from the dye molecule before they recombine with holes. TiO_2 nanoparticles may be used in various crystal structures and morphologies in the DSSC application [6, 7, 8, 9]. TiO_2 nanoparticle-based porous films can provide large surface area for dye adsorption and improve efficiency [10, 11].

TiO_2 has three polymorphs namely: anatase, rutile and brookite. Anatase is the commonly used structure of TiO_2 in optoelectronic applications due to high diffusion of electron inside the structure without recombination, large band gap energy of this phase which may raise the valence band maximum to higher energy levels [9, 12, 13]. However, recently rutile structure was also reported to be a good candidate for opto-electronic applications due to some superior properties like high light scattering ability and stability [14, 15]. Brookite is a transition phase between anatase and rutile. This phase is generally ignored for applications due to the difficulty in synthesizing [16].

Various TiO_2 nanostructures in the forms of spheres, tubes, wires, rods, sheets, belts, flowers, and trees have been reported until now [17]. Every structure has its own sophisticated properties like high surface area, low recombination, high diffusion of charge carriers and/or light scattering ability [18]. These structures may be used as photocatalyst or photovoltaics alone or two or more in a row to benefit different properties of different morphologies [6, 19].

Various morphologies and crystal structures of TiO_2 have been synthesized using a variety of synthesis methods such as hydrothermal process [20], solvothermal method [21], sol-gel method [22], direct oxidation method [23], chemical vapor deposition (CVD) [24], electrodeposition [25], sonochemical method [26] and microwave assisted method [27]. Among the methods applied, hydrothermal process is a rather feasible one for the synthesis of nanostructures with controlled morphology, good crystallinity with precise crystal structure and determined

composition at one step without further treatment. It is a widely used method for synthesizing many ceramic nano particles with excellent chemical homogeneity and offering the possibility of achieving unique metastable structures. In a typical hydrothermal process, a precursor material of the final oxide (metal salts, oxides or alkoxides), water, catalyzer material are used. Also alcohol, oxidizing agents, seeds of surfactant materials may be used.

Use of acid or base catalyzer in hydrothermal process results in the evolution of TiO₂ nanostructures with different morphologies and crystal structures. While the use of alkali hydroxides as catalyzer may result in titanate structure that needs further treatment for TiO₂ achievement, acid catalyzers may result in the evolution of TiO₂ nanostructures directly [28]. However, other parameters like precursor type, pH, temperature, pressure, dwell time, and other post treatments are highly important for the properties of final product. The properties yielded by hydrothermal treatment are very important for the performance of TiO₂ nanostructures to be used either photocatalytic or photovoltaic applications. In order to increase the photoactivity of TiO₂, other than synthesis with specific crystal structure and morphology, doping of metals and/or nonmetals is frequently used. Recently, doping TiO₂ with nonmetals and transition metal ions is an attractive strategy in terms of engineering the band gap for getting higher efficiency in opto-electronic activities.

1.1 Objectives and outline of the study

Although there are several publications reporting the results for improvement in properties of semiconductor layer of DSSCs, the relation between optical to electrical conversion efficiency and properties of TiO₂ are not fully understood. The subject keeps its interest and popularity. Even 1 % enhancement of efficiency is a huge achievement for DSSC technology and energy harvesting. Any improvement of efficiency resulting from powder characteristics and construction of the cells is valuable. The objective of the present work is to synthesis TiO₂

nanopowders with various phases and morphologies using hydrothermal process and to use the powders synthesized in the fabrication of DSSC. Also, triple-doping of titania by N, Mo and Fe was investigated to improve the photocatalytic activity of DSSC.

In Chapter 1, an introduction to the study, which explains briefly the issues important for this study, is given. Chapter 2 briefly reviews the literature on background and working principles of DSSCs and followed by main topic semiconductor photoanode. In this chapter the properties, synthesis and application of titanate and TiO₂ nanostructures, as well as doping effect on the properties of TiO₂ are explained. Previous studies reported by other researchers are outlined. The experimental procedure for synthesis of titanates and TiO₂ nanostructures is explained in detail in Chapter 3. Characterization tests including x-ray diffraction (XRD) analysis, field emission electron microscope (FESEM) analysis, high resolution transmission electron microscope (HRTEM) analysis, x-ray photoelectron spectroscopy (XPS), brunauer emmett teller (BET) surface analysis, UV-Vis spectrophotometer, energy-dispersive x-ray spectroscopy (EDS), and inductively coupled plasma-mass spectroscopy (ICP-MS) are explained. Then, measurements of optical band gap energy and photocatalytic test using methylene blue as an organic pollutant of powders are explained in Chapter 3. Preparation of DSSC is also explained in this chapter including paste formation, photoanode and counter electrode preparation using scotch tape casting and spin coating, respectively and assembly of the cell. Photovoltaic measurements and electrochemical impedance spectroscopy (EIS) were explained in Chapter 3. Chapter 4 gives the results for structural and morphological analysis of titanate and TiO₂ nanostructures synthesized using base assisted hydrothermal method and discusses the findings with reference to the values given in the literature. This chapter also gives the results of band gap measurements and photocatalytic tests of representative powders. Chapter 5 presents the results for structural and morphological analysis of TiO₂ nanostructures synthesized using acidic hydrothermal method. An evolution mechanism was proposed for flower like rutile

structures in this chapter. Chapter 6 reports the results and discussion of TiO₂ and doped TiO₂ nanostructures synthesized using acid assisted hydrothermal synthesis and gives the results of band gap measurements and photocatalytic tests of representative powders. Chapter 7 reports the results of photovoltaic measurements and (EIS) of DSSCs prepared by as synthesized TiO₂ pastes following by typical characterization of anode part of the cell. Finally, Chapter 8 gives the main conclusions of the whole study and Chapter 9 touches upon the future work.

CHAPTER 2

OVERVIEW

2.1 Solar cells

Solar energy is the most abundant, sustainable and clean one of all the renewable energy resources. In fact, renewable energy has reached a maxima and its share in the energy supply is growing. International and national policies of countries are paying attention and support the growth for a variety of reasons including climate change, fossil fuel cost, and social demand. Photovoltaic technology is one of the efficient ways to harvest the solar energy. Since the discovery of the photovoltaic effect by Alexandre-Edmund Becquerel in 1839, researches have been increased in this field. Capturing solar energy and converting it to a quality energy like electricity is still a huge challenge. Photovoltaic devices known as solar cells are the primary solar energy conversion systems. They convert solar energy into electricity through generation and collection electron-hole pairs. Some challenges for wide application of solar energy are like being low cost, stability, high efficiency, and nontoxic raw material employment.

Solar cells are generally categorized into three groups based on generations, performance, and cost. The first generation solar cells are conventional Si solar cells that were already commercialized. The second generation solar cells are thin film based solar cells, which are much cheaper to produce, compared to 1st generation solar cells. However, both 1st and 2nd generation solar cells suffers from limited efficiency by Shokley Quasier theoretical limit of 30 % [29]. The 1st and 2nd generation solar cells are p-n junction solar cells on which an electric field is formed without existence of external bias due to inter-diffusion of majority and minority charges (Depletion region). These charges are formed by separating with photon absorption. As long as the separated charges arrives out of the depletion region then they are majority carrier and can be collected on the positive and

negative edges giving rise to the current. Lastly, the third generation solar cells are any kind of solar cell other than 1st and 2nd generation solar cells. These solar cells employ many different technologies and they do not suffer from Shockley Quasier limit. Furthermore, many of these solar cells have not been commercialized yet. The graph of efficiency achievements with respect to years of different photovoltaic cells is shown in Figure 2.1 [30]. Dye sensitized solar cells (DSSCs) are one of the 3rd generation solar cells.

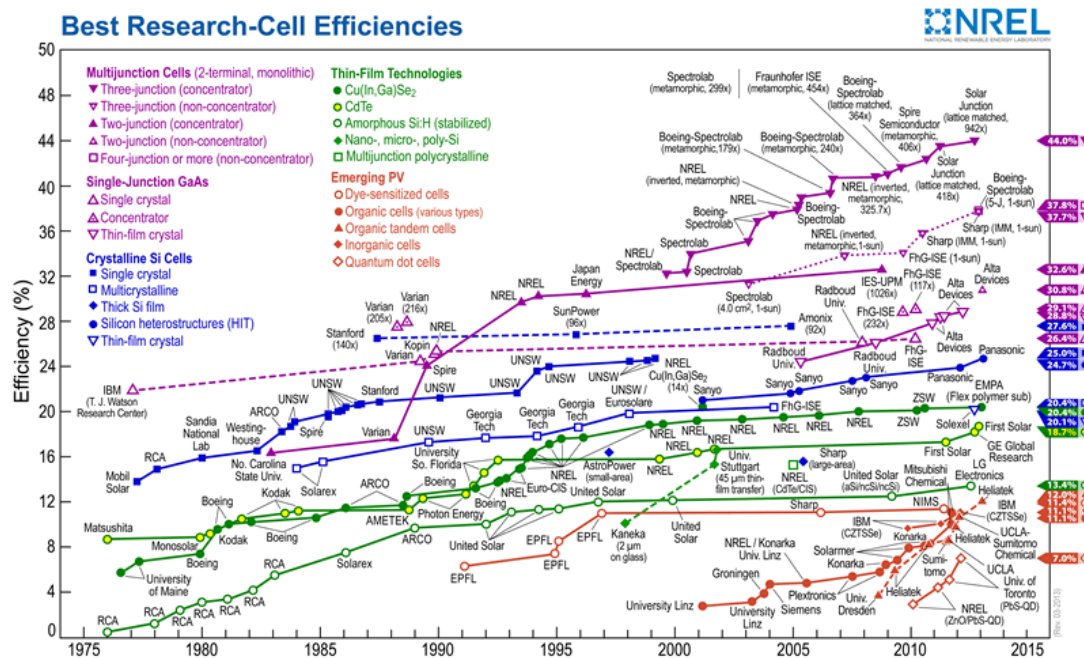


Figure 2.1 Record efficiencies for different types of solar cells in the world [30].

2.2 Solar cell terminologies

A current source with a forward biased diode in parallel indicates the equivalent circuit of an ideal solar cell which is shown in Figure 2.2. Series and parallel resistances are combined to accounted for various loss mechanisms.

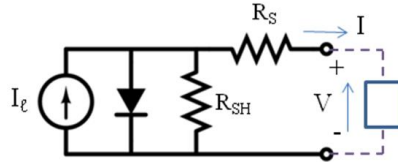


Figure 2.2 Solar cell equivalent circuit [31].

Short circuit current (I_{sc})

I_{sc} is the current obtained from the cell when the load resistance is zero. A solar cell current (J_{sc}) can be calculated by;

$$J_{sc} = I_{sc}/A \text{ (mA/cm}^2\text{)} \quad (1)$$

where, A is the effective area of the solar cell. I_{sc} depends on solar illumination, dye loading for DSSC, optical properties and charge transfer characteristic of the cell.

Open circuit voltage (V_{oc})

Open circuit voltage is the maximum voltage can be yielded with a solar cell and it is obtained by inserting a load with infinite resistance. This term depends on semiconductor band gap and charge recombination of the cell. For DSSCs, V_{oc} can be calculated by following equation.

$$V_{oc} = \frac{E_{cb}}{q} + \frac{kT}{q} \ln\left(\frac{n}{N_{cb}}\right) - \frac{E_{redox}}{q} \text{ (volts)} \quad (2)$$

Series resistance (R_s)

Series resistance can be considered as contact resistance and charge transfer resistance in the semiconductor material. Increasing series resistance decreases the fill factor affecting the maximum efficiency which was explained below. R_s also decreases I_{sc} . However, it does not affect V_{oc} that the total current flow through the cell which makes R_{sc} zero.

Shunt resistance (R_{sh})

Shunt resistance is important. Because it provides an alternate path for current which causes reduced efficiency. The low shunt resistance causes low fill factor and low V_{oc} . J_{sc} does not get affected by shunt resistance since the total current flows through the outer path at short circuit conditions.

Fill factor (FF)

FF is the maximum power output of a solar cell which is the ratio of the maximum power to the product of V_{oc} and I_{sc} of the solar cell. It can be calculated by the area under the current voltage diagram. It has not a unit and a function of series and shunt resistance of the solar cell. For DSSC it represents the extent of electrical and electrochemical loses. In order to obtain a high fill factor, one may increase shunt resistance and decrease series resistance with reduction of overvoltage for diffusion and charge transfer.

$$FF = \frac{V_m \times I_m}{V_{oc} \times I_{sc}} \quad (3)$$

Efficiency (η)

The efficiency of the solar cell is the ratio of maximum electrical energy obtained to the energy input from the sun.

$$\eta = \left(\frac{V_{OC} \times I_{SC} \times FF}{P_{in}} \right) \quad (4)$$

where, P_{in} is the incident photon energy. Besides the solar cell performance, it depends also on the light spectrum supplied. The international condition for the efficiency measurement is AM 1.5 Global at room temperature.

2.3 Dye sensitized solar cell (DSSC)

2.3.1 History

The electricity generation by organic dyes has already been known since 1960s. However, the first electricity generation by dye sensitized semiconductor film was done using ZnO semiconductor and Chlorophylls [32]. The dye sensitized solar cells are generally known as “synthetic photosynthesis” due to mimicking photosynthesis. The first dye sensitized solar cells were built in 1980s [33]. However, the first real DSSC were done by Grätzel and O’Regan in 1991 [34]. Thus it was shown that DSSC may be a good alternative to conventional solar cells. The highest efficiency reported until now was 13 % with Zn based dye and Co based electrolyte system [35, 4].

2.3.2 Operation mechanism

DSSC works with the same principle as plant photosynthesis to harvest energy from solar energy. Even though plant leafs work with only 0.02-0.05 % efficiency,

the food being produced is 100 times more than man necessity [36]. The chlorophyll in green leaves generate electron by solar energy and starts the subsequent reactions to complete photosynthesis process. Typical DSSC configuration can be seen in Figure 2.3.

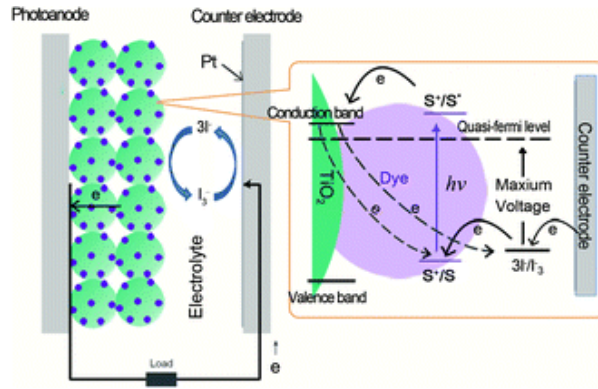


Figure 2.3 Basic device components and electronic band alignments for DSSC [37].

The DSSCs are the only photovoltaic devices which separately does the absorption (dye), generation and carrier transport (TiO_2). The operation steps can be listed as below;

2.3.3 Excitation

Photon energy is absorbed by sensitizer and it continues an electronic state from the ground (S) to the excited state (S^*). Most of the dyes has an absorption onset in the range of 720 nm which corresponds to 1.72 eV photon energy. The lifetime of the excited state is in the order of nanoseconds.



2.3.4 Injection

The sensitizing dye molecules are adsorbed to the surface of a wide band gap semiconductor nanoparticles such as TiO₂. Upon absorption, dye molecules gain the potential to transfer an electron to the conduction band of semiconductor. The internal electric field of the nanoparticles causes the electron extraction and the dye becomes oxidized. For efficient electron injection the lowest unoccupied molecular orbital (LUMO) of the dye has to be about 0.3 eV above the TiO₂ conduction band. The injection rate constant is in the femtosecond range which is shorter than lifetime of excited state of sensitizer.

2.3.5 Diffusion in semiconductor layer

The nanoporous TiO₂ film consists of nanoparticles with large surface area. The presence of oxygen vacancies in the lattice makes the material a weak n-doped semiconductor material. By the effect of nano size, the diameter of particles is too small to build up an electric field and thus the dominant electron transport mechanism is diffusion.

2.3.6 Iodine reduction

The electron travels the outer circuit to create work and reaches the back FTO electrode. The Pt layer acts as a catalyst for reduction and lastly reduces the iodine in the electrolyte. The cathodic reaction is as follows;



2.3.7 Dye regeneration

The reduced iodide ion regenerates the highest occupied molecular orbital (HOMO) of the dye-replenishing its original form, and makes it ready for electron generation again. The reaction in the photoanode is as follows,



This prevents creating S^* which would lead to the conduction band electrons going back to the dye molecules. The maximum output voltage equals to the difference between Fermi level of the semiconductor and the redox potential of the mediator [38].

2.3.8 Electrochemical Impedance Spectroscopy (EIS) of DSSC

EIS is a powerful technique to study the electrical charge transfer and accumulation in the cell upon functioning [39]. EIS is often measured by applying a small (3-20 mv) sinusoidal potential excitation signal (ΔV), at certain potential, V ;

$$V = V_o + \Delta V = V_o + v \sin(\omega t) \quad (9)$$

with v is amplitude of the signal and (ω) is the angular frequency when a certain voltage is applied. The response to this signal is a pseudo-linear AC current signal, ΔI , that will be a sinusoid at the same frequency but phase shifted (ω) and with a different amplitude as following;

$$I = I_o + \Delta I = I_o + i \sin(\omega t + \varphi) \quad (10)$$

Electrical impedance (Z) is defined as the measure of the opposition that a circuit which presents when a voltage is applied. It can be assumed as resistance within DC circuit. The difference is that impedance has both magnitude and a phase component. It is formulated as;

$$Z(\omega) = \frac{\Delta V}{\Delta I} \quad (11)$$

$$Z = |Z|e^{j\varphi(\omega)} = Z' + jZ'' \quad (12)$$

2.3.9 Components of DSSC

Dye:

The sensitizer dye is one of the important components of DSSC. By sensitization of semiconductor film, dye molecules cover the nanoparticles forming a monolayer which is nearly with a ratio of 1 to 100 for Ru to Ti [40]. Alternative sensitizers must give efficient light absorption, charge injection and collection. The most importantly, spectral response should be in the visible range. The excited state should be replaced with respect to semiconductor band alignment. The reduced state of dye should be tuned to the reduction potential of the electrolyte in order to transfer holes efficiently. A suitable potential is approximately 0.3 eV for minimum recombination as mentioned earlier [41]. Another important parameter is the stability of dye molecules onto the surface of semiconductor particles which is expected minimum 20 year or 10^8 redox cycle. Another important parameter is good adsorption to titania nano particles [42, 43]. The most efficient dyes are metal-organic ruthenium complexes until now [44, 45]. The common dyes used in DSSC are Ru based N3, N719, N749 (black dye) and recently cobalt based Z907 in which a new record of 12.3 % was broken. Research on metal free sensitizers is also done [35, 41, 46].

Electrolyte:

The voltage produced in DSSC is determined by the difference between the chemical potential (Fermi level) that the electrons acquire in the TiO₂ nanoparticles and the hole chemical potential in the hole conducting medium (for redox electrolytes, the Nernst potential). Most of the DSSC was manufactured using iodide/triiodide electrolyte in terms of a redox couple dissolved in a dipolar aprotic solvent to improve the properties of DSSC. Electrolyte regenerates dye hence the performance of DSSC highly depends on this element. The maximum current is limited by electrolyte and Fermi potential of the electrolyte affects the open circuit potential [47]. The electrolyte should be inert to be reversible in the counter electrode. Another important property is not absorbing visible light. The electrolyte should not cause removal of dye from semiconductor surface. Additionally, the electrolyte should have less viscosity for fast charge transfer. However, low viscosity also results in short life due to evaporation. For that reason solid electrolytes are highly researched to date [11, 48].

Counter Electrode:

At counter electrode, electrolyte reduction is done. Carbon black, carbon nanotube, graphite, graphene inorganic compounds, composites and conductive polymers are being used as catalyzer [49, 50, 51, 52]. Platinum (Pt) is the most commonly used catalyst for counter electrode application due to its high performance [50]. The deposition method of Pt on transparent conducting oxide (TCO) is important for high efficiency. The coating can be done by electrochemical method, chemical vapor deposition method, spin coating and sputtering. In this study, spin coating method was used to prepare Pt counter electrode.

Mesoporous oxide semiconductor layer (Working electrode):

The mesoporous oxide semiconductor layer is the heart of DSSC. TiO₂, zinc oxide (ZnO), tin dioxide (SnO₂), indium oxide (In₂O₃), yttrium oxide (Y₂O₃) and niobium oxide (Nb₂O₅) are the mostly used semiconductor materials for

fabricating DSSC. Among many wide band gap oxide semiconductors, TiO_2 is the most versatile semiconductor material due to highest efficiency. It is chemically stable, non toxic and available. It has also a suitable HOMO and LUMO levels with respect to electrolyte and dye [53]. Extensive research has been done for higher light harvesting efficiency of TiO_2 which is influenced by crystalline phase, particle size, surface properties, dye affinity and porosity [54, 55]. Photogenerated current from the solar cell increases with the increase of surface area due to increasing of adsorption of dye. However, increasing porosity decreases the current due to the decreasing of mass of TiO_2 per area. However, small pores cause slow diffuse of charge carriers due to small volume for electrolyte fill. Surely, electrolyte viscosity is also important [56]. The average pore size depends on paste formation and annealing profile. Increasing annealing temperature increases porosity until particular temperature for different structures [57]. TiO_2 particle size is another parameter for DSSC efficiency. An optimum particle size is needed for DSSC application. Electron diffusion coefficient increases with larger particle size due to decrease of surface area and grain boundaries. However, electron recombination life time decreases with increasing particle size [58].

Typical film thickness for DSSC is 5-20 μm with semiconductor material amount of 1-4 mg/cm^2 . Semiconductor thickness is important for efficient photon absorption [59]. V_{oc} decreases by increasing thickness. As the light is transmitted into the depth of an electrode, the light intensity gradually decreases. Therefore, as thickness increases, the excessive electron density becomes lower, resulting in a lower V_{oc} . The higher serial resistance of thick electrodes also contributes to the reduction of photo voltage. The decrease in V_{oc} can also be attributed to the increased charge recombination and restricted mass transport in thicker films [60]. Current depends on electrolyte viscosity. If the viscosity of electrolyte is low then electrolyte can support higher photocurrent generated from thick semiconductor layer [61]. However, there are studies which report opposite of the above finding [62]. For a maximum performance, layers may be as following: blocking layer, absorption layer, scattering layer and over coating.

Charge recombination is one of the reasons for lower current for DSSCs. Recombination may occur at the electrolyte/TCO and/or semiconductor/electrolyte interface. A blocking layer may effectively prevent the recombinations occurring between TCO and electrolyte which increases J_{sc} and V_{oc} [63]. In this study, instead of blocking layer, a cost effective way of decreasing recombination at the interface of TCO and electrolyte is $TiCl_4$ treatment was adopted for one sample. $TiCl_4$ treatment also reduces recombinations between TiO_2 /electrolyte interface by increasing contacts between nanoparticles which reduces resistance decreasing dark current and increasing photocurrent. Also it improves surface roughness factor and light absorbance [64]. The other limitation is the weak performance of the dye under infrared radiation. A scattering layer using 200-400 nm sized particles on the top of the absorption layer allows scattered photons to be kept with several reflections especially in the red or infrared region. Several mA/cm^2 increment of J_{sc} was reported using scattering layer [65, 66]. In this study, 3D rutile submicron structures built by porous nanocrystallites as units was studied as scattering layer.

2.3.10 Deposition of mesoporous oxide semiconductor layer onto TCO

Semiconductor nano particles are often turned into a paste using binder. There are different recipes for paste formation in the literature such as using polyethylene glycol, ethylene glycol and ethyl cellulose as binder; Triton X, terpineol, α -terpineol as solvent and acids such as acetic acid, hydroxybenzoic acid, nitric acid. The paste then deposited on FTO using one of the doctor blade, spin coating, scotch, screen printing method. After deposition the film is sintered and ready to use as photoanode of the cell. Instead of deposition of nanoparticles in paste form, recently TiO_2 particles were grown on FTO glass directly in appropriate solutions with or without templates. This process is beneficial for taking advantage of one dimensional structures which will explain further in this chapter. However, efficiency values were limited due to decreasing surface area of these structures. Other deposition techniques of semiconductor particles are electrochemical

anodization [67], electrospinning [68], spray pyrolysis [69] and atomic layer deposition [70]. In this study, synthesized powders were turned into pastes for screen printing and/or scotch deposition.

2.3.11 Semiconductor photoanode materials used in DSSC

Variety of oxide materials have been developed and applied for crafting a diverse assortment of nanostructured semiconductor photoanodes such as TiO_2 , ZnO , SnO_2 and Nb_2O_5 , including variations of crystal structures and morphologies like nanorod [71], nanotube [72], nanosheet [73], mesoporous 3D hierarchical architectures [74] of these materials. Most of these structures offer considerable efficiency improvements compared to nanoparticle systems. For example, 1D semiconductor nanostructures exhibit excellent charge transport properties [71]. Additionally, 3D mesoporous nano/microspheres, by virtue of their larger surface area ($>100 \text{ m}^2/\text{g}$), possess better light scattering properties [71].

2.4 Titanium dioxide (TiO_2) properties and synthesis

Titanium (Ti) is one of the mostly available material in the earth crust (ninth). The common raw materials are rutile, ilmenite and leucosene. Ti may have been in the oxide form of TiO , Ti_2O_3 , TiO_2 , Ti_3O_5 , Ti_4O_7 ; $\text{Ti}_n\text{O}_{2n-1}$ where, n ranges between 3–9 [75, 76]. The most stable form is TiO_2 (Titanium (IV) oxide or titania) which is used in cosmetics, drugs, pigment, paper, and semiconductor [77]. The reason of application of TiO_2 as a semiconductor is due to its many advantages like low cost, wide abundancy, nontoxicity, biocompatibility, stability, proper band gap energy and photocatalytic activity [50, 78]. After discovery of water splitting by Fujishima and Honda, TiO_2 was mostly studied for photocatalytic applications [79]. The photocatalytic ability of TiO_2 depends on its crystallinity, crystal structure, grain size, surface properties, morphology and composition [71, 80].

TiO₂ has three main crystal structure which are anatase, rutile and brookite as seen in Figure 2.4. The structural properties of the phases calculated by Pseudopotential Hartree-Fock model and some physical properties are tabulated in Table 2.1. It has also other synthetic forms in monoclinic, tetragonal and orthorhombic structures [81, 82]. Also it has five high pressure forms which are α -PbO₂-like, baddeleyite-like, cotunnite-like, orthorhombic and cubic phase [82, 83, 84].

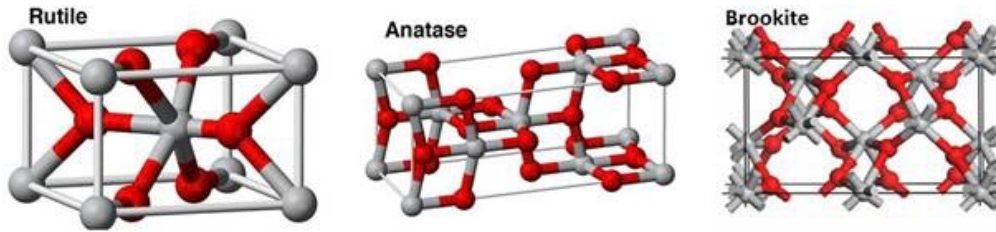


Figure 2.4 Crystal structures of TiO₂.

Table 2.1 Classification of structural properties of anatase, rutile and brookite using the Pseudopotential Hartree-Fock (PHF) calculations [85].

Property	Rutile	Anatase	Brookite
Crystal structure lattice constants (Å)	Tetragonal a=4.5936 c=2.9587	Tetragonal a=3.784 c=9.515	Orthorhombic a=9.184 b=5.447 c=5.145
Space group	<i>P4₂/mnm</i>	<i>I4₁/amd</i>	<i>Pbca</i>
Molecule/cell	2	4	8
Volume/molecule (Å ³)	31.2160	34.061	32.172
Density (g/cm ³)	4.13	3.79	3.99
Ti-O bond length (Å)	1.949(4) 1.980(2)	1.937(4) 1.965(2)	1.87~2.04

Rutile is the most stable form of TiO₂. Anatase phase of TiO₂ is a metastable one, which is widely used for photocatalytic applications due to its wide band gap, surface properties, proper structure for electron diffusion [86, 87]. In general,

majority of TiO₂ synthesis processes result in rutile formation. It is mostly used in high temperature conditions such as gas sensors. Brookite is another metastable phase of TiO₂ between anatase and rutile. It is generally ignored due to difficulty of synthesis. Ti⁴⁺ atoms are coordinated to six oxygen atoms to form TiO₆ octahedra in all three forms of TiO₂. Anatase phase is formed by corner sharing octahedras, rutile is formed by edge sharing of octahedras, and brookite is formed by both edge and corner sharing of octahedras [88]. Some physical property classification of anatase and rutile are shown in Table 2.2.

Table 2.2 Physical properties of anatase and rutile [88].

Property	Anatase	Rutile
Molecular Weight (g/mol)	79.88	79.88
Melting point (°C)	1825	1825
Boiling point (°C)	2500~3000	2500~3000
Specific gravity	3.9	4
Light absorption (nm)	<380	<415
Mohr's hardness	5.5	6.5-7.0
Refractive index	2.55	2.75
Dielectric constant	31	114

TiO₂ could be recognized as an insulator material due to its wide band gap energy (3 eV for rutile, 3.2 eV for anatase) [89]. However, TiO₂ becomes in oxygen deficiency when it is equilibrated under low oxygen atmosphere. Thus, it becomes an n-type semiconductor with free electrons as charge carriers. The defects in oxygen deficient form could be caused by both intrinsic and extrinsic types which are controlled by experimental conditions and foreign anions and/or cations, respectively [90, 91]. The deviation from stoichiometry in TiO_{2-x} depends on x, which may be attributed to be a function of oxygen partial pressure P(O₂) as:

$$x \propto P_{O_2}^{-1/mx} \quad (13)$$

where, mx signifies the characteristic of defect [91].

The reduced charge regime is mainly a function of Ti^{+3} interstitials, which are compensated by electrons. The strongly reduced part is due to doubly ionized oxygen vacancies and reduced regime is dominated by ionic charge compensation. The oxidized part could be achieved by high oxygen partial pressure. All these defects have a significant importance on electrical properties of TiO_2 . The valance band corresponds to O related states and the conduction band corresponds to Ti related states. Anatase possesses a narrower 3d band compared to rutile, which is the result of localization of Ti 3d states due to large Ti-Ti atomic distances in this polymorph [92].

In photocatalytic process, an electron excites to the conduction band and leaves a hole in valance band under light illumination. Electron illumination is based on proper band gap that is light energy greater than band gap energy of semiconductor excites electron from valance band to conduction band. Relatively larger band gap energy of TiO_2 makes it active only under UV illumination (<387 nm for anatase and 410 nm for rutile). After excitation, formed charge carriers (electron and hole) can be trapped by Ti^{3+} and oxygen defect sites and/or recombination occurs. Separated charge carriers diffuse to the surface and initiates photocatalytic reactions. Holes are trapped by surface adsorbed H_2O and oxidizes H_2O to form H^+ and OH^- radicals that are very powerful oxidants. These strong oxidants oxidize adsorbed organic species. Consequently, CO_2 and H_2O are being formed. If the electrons are trapped by the adsorbed oxygen molecule reducing O_2 to O_2^- , forms peroxide radicals like OOH^- and H_2O_2 by reacting with H^+ .

Photocatalytic and photovoltaic properties of TiO_2 highly depend on its synthesis method that has a direct influence on electronic configuration, crystal structure, and morphology. TiO_2 suitable for optoelectronic applications can be synthesized by several methods like sol-gel, solvothermal, hydrothermal, atomic layer deposition (ALD), chemical vapor deposition (CVD), micro emulsion, micelle and inverse micelle processes.

2.4.1 One dimensional TiO₂ and titanate related nanostructures

One-dimensional TiO₂ or titanate related nanomaterials with high morphological specificity, such as nanotubes, nanosheets, nanoribbons, nanowires, nanofibers and nanorods, have attracted considerable attention due to their interesting chemical and physicochemical properties. The high interest to the one dimensional materials was initiated by first carbon nanotube discovery in the early 1990s [93] which is promising for many applications due to their excellent mechanical, optical, electrical and/or chemical properties. Nevertheless, materials other than C are much easier to synthesize due to diverse chemistry [94, 95, 96]. The 1D structures may be used in a wide range of applications such as medical purpose [97], electrochemistry [98, 99], environmental purification [100, 101], gas sensors [102]. A time line showing briefly the historical background of TiO₂ related nanotubular structures can be seen in Figure 2.5.

The first TiO₂-based nanotubes was reported by Hoyer in 1996 [103] via an electrochemical deposition using naturally occurring porous aluminum oxide. Up to now 1D TiO₂ nanostructures were synthesized using three different methods which are chemical template synthesis [104], electrochemical anodic oxidation method [105] and alkaline hydrothermal treatment [96]. The preparation of TiO₂ 1D structure by chemical templating usually involves controlled sol-gel hydrolysis of Ti compounds in the presence of templating agents followed by polymerization of TiO₂ in the self-assembled template or deposition of TiO₂ on the surface of the template [94]. The procedure ends by removing templating agent and calcination. Although the template assisted method attracted much attention in the early 2000s which makes possible to prepare numerous materials with a regular and controlled morphology by adjusting the template morphology, this method is mostly disadvantageous because of the high cost of template material separating [95, 104].

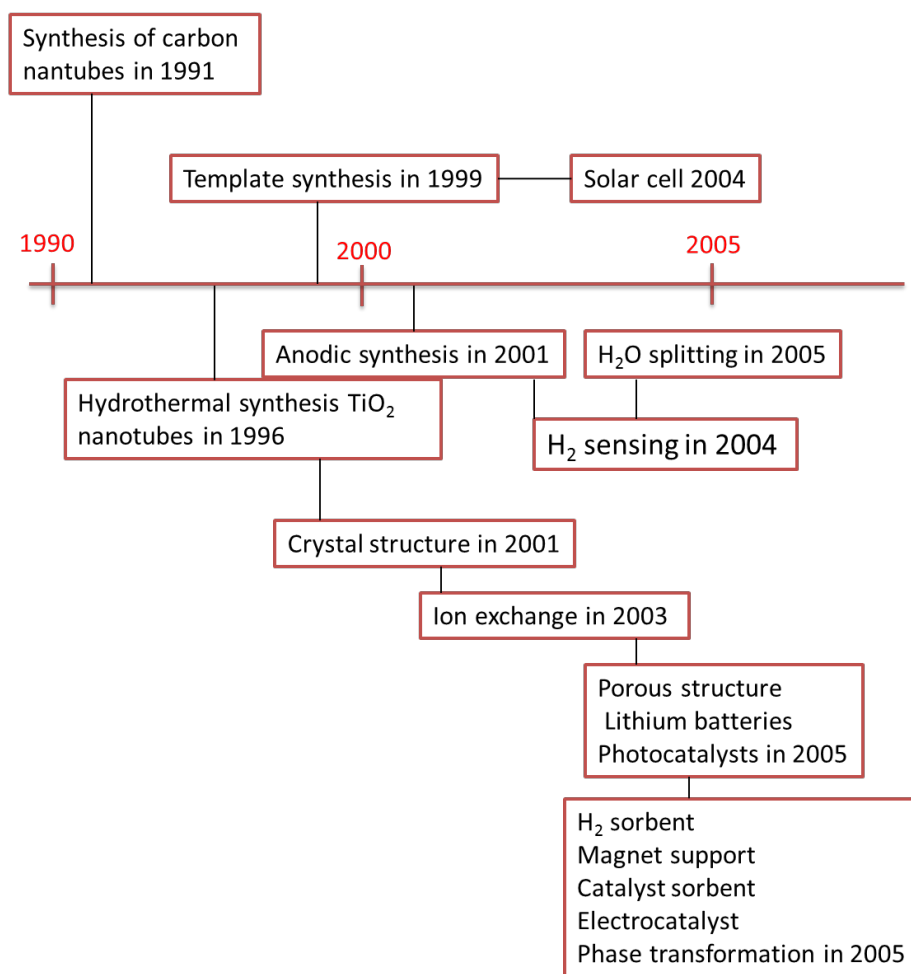


Figure 2.5 A timeline describing the development of TiO₂ related nanotubular structure [94].

In 2001, Grimes and co-workers [105] reported the self-organized TiO₂ nanotube arrays by direct anodization of Ti foil in a H₂O-HF solution at room temperature. The nanotubes were oriented in the same direction. The thickness of the film was only 200 nm. One end is open while the other end in contact with foil was always closed. However, nanotubes cannot be separated from each other and should be calcined for crystalline material. In 1998, Kasuga and co-workers [96] first reported a simple method for the preparation of TiO₂ nanotubes by hydrothermal process using precursor TiO₂ in a strong alkaline solution (KOH or NaOH) at high temperature for a long time followed by a washing step with water or acidic solutions. In a typical process, several grams of TiO₂ can be converted to any 1D

structure at temperatures in the range 110-150 °C [96]. It has been shown that any TiO₂ structure (anatase, rutile, brookite, amorphous forms) can be transformed into 1D structure. There are a large number of crystal modifications after hydrothermal treatment. Several titanate structures achieved after hydrothermal treatment and/or post treatments were summarized by Bavykin et al. [94]. These structures are given in Table 2.3.

Table 2.3 Phase variations using base assisted hydrothermal process, crystal structure and some of the diffraction angles [95].

Crystallographic phase	Symmetry	2θ (degree)					
H ₂ Ti ₃ O ₇	Monoclinic	11		24.4	29	48.4	62
H ₂ Ti ₂ O ₄ (OH) ₂	Orthorhombic	9		24.3	28	48	62
H ₂ Ti ₄ O ₉	Monoclinic	10		24	28	48	
H ₂ Ti _{2-x/4} □ _{x/4} O ₄ .H ₂ O	Orthorhombic	9.5		24.5	28	48	62
TiO ₂ B	Monoclinic		15	25	29.5	48	62
H ₂ Ti ₅ O ₁₁ .H ₂ O	Monoclinic	10	14			46	

□: vacancy

Layered titanate nanostructures are promising not only because of the advantage of easy and cheap production, but also because of the intriguing hydrated structure and morphological changes induced by surface chemistry. However, there are several problems for determining the crystal structure of alkaline hydrothermal product. The most important problem is instability. Structure easily transforms by washing with distilled water, acidic treatment, and calcination. The other one is small crystals cause small coherent area which results in broadening of the peaks forming reflections in the XRD data. Furthermore, wrapping or spreading along a certain crystallographic axis during the formation of 1D structure, results in widening of peaks making assignment difficult. Initially, Kasuga and co-workers [96] suggested that their product is anatase. Peng and co-workers [106, 107] proposed that the crystal structure of titanate nanotubes corresponded to the layered trititanic acid (H₂Ti₃O₇) with a monoclinic crystal structure. A schematic

showing the crystal structure of monoclinic trititanic acid in a TiO_6 edge-sharing octahedron representation is shown in Figure 2.6 [94]; the three different projections corresponding to crystallographic axes. A nanotubular morphology of layered trititanic acid may be formed by obtained by rolling several (100) planes around axis [010] or [001] [94]. It has been propose that rolling of the plane occurs around the [010] axis such that the axis of the nanotube is parallel to the b-axis of monoclinic $\text{H}_2\text{Ti}_3\text{O}_7$ [94]. Wu et al. [108] have proposed that rolling of the (100) plane could occur around axis [001]. In both cases, the walls of the nanotubes consist of several layers, typically separated by 0.72 nm. The structure of each layer corresponds to the structure of the (100) plane of monoclinic titanates, which is a set of closely packed TiO_6 , edge-sharing octahedral.

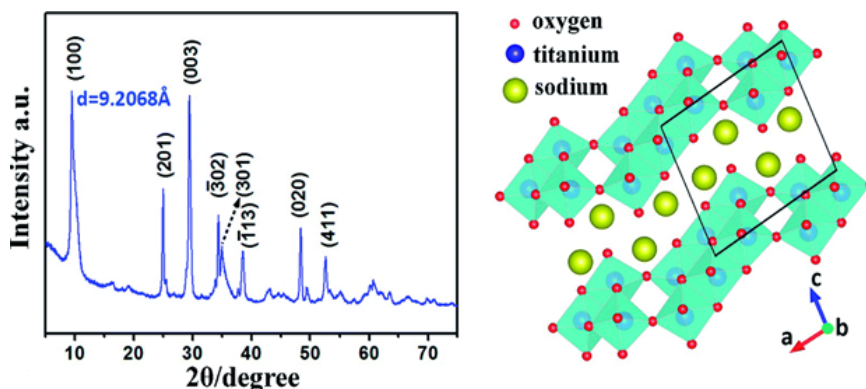


Figure 2.6 a) Typical XRD pattern of $\text{Na}_2\text{Ti}_3\text{O}_7$ and (b) Crystal structure of Na titanate [109].

Zhang et al. [110], based on the studies of Na content, suggested the crystal structure of $\text{H}_2\text{Ti}_2\text{O}_4(\text{OH})_2$. It was demonstrated that bulk layered protonated titanates could be transformed to the metastable monoclinic modification of TiO_2 (TiO_2 -B) under calcination [95]. This modification of TiO_2 has a lower density than anatase or rutile and has a monoclinic unit cell. The structure of TiO_2 -B is characterized by a combination of edge- and corner-sharing TiO_6 octahedra forming a structure with channels in which transport and exchange of small cations can occur [94]. Indeed, washing of sodium titanate nanotubes with acid or water

results in the formation of the protonated form of titanate nanotubes [94]. Following drying at increased temperatures, dehydration of solids and formation of TiO₂-B nanotubes could occur, the product having a density in the range 3.64–3.76 g cm⁻³, which is less than the density of anatase or rutile (3.9 and 4.25 g cm⁻³, respectively) [94]. The XRD pattern of TiO₂-B crystals, however, is a little different from that of TiO₂ nanotubes, especially at small 2θ values (see Table 2.3). The calcination of titanate nanofibers results in consecutive transformation from titanate to TiO₂-B (at 400 °C), then to anatase (at 700 °C) and rutile (at 1000 °C). Nanofibrous morphology disappears at 1000 °C [111].

Since the discovery of wet chemical method, several attempts have been done to understand the mechanism of transformations. Originally, Kasuga and co-workers [96] considered that a tubular morphology is being achieved after washing of the hydrothermal product. Some of the researchers still support this proposal. However, it was demonstrated that, 1D structure is being formed during hydrothermal synthesis [112]. The long, solid, parallelepiped titanates are named nanoribbons, nanobelts, or nanofibers in the literature. These structures tend to have good crystallinity and usually the relation between the lengths of the edges corresponding to each crystallographic axis is in the order 001 >> 100 > 010 [113]. The length of nanofibers (001) can be several tens of micrometers, while the width of nanofibers (001 or 010) is typically in the range 10–100 nm [94]. The aspect ratio can be as large as several thousand. Nanofibers, which are usually produced during alkaline hydrothermal reactions at high temperatures, can be found in straight as well as in curved forms [94]. Zhang et al. [114] considered that single surface layers experienced an asymmetrical chemical environment, due to the imbalance of H⁺ or Na⁺ ion concentration on two different sides of a nanosheet, giving rise to excess surface energy, resulting in bending. Another, the morphology of the derived titanate is also controversial as nanotube, nanoribbon, nanosheet or nanorod, all have been observed [115]. Chen et al. [106] and Morgado et al. [116] suggested that the formation of titanate tubes is independent of the original structure and particle size of the TiO₂. Zhang et al. [117] manifested

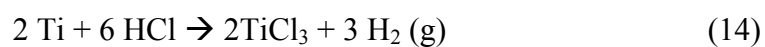
that a smaller raw material generally exhibits a higher surface energy, which is favorable for the formation of nanotubes after hydrothermal treatment. On the other hand, Yuan et al. [118] found that nanofibers, rather than nanotubes, are obtained when amorphous TiO_2 or commercial TiOSO_4 is used as the precursor.

Titanate nanotubes are wide-band gap semiconductor materials. From studies of the optical properties of aqueous colloids of titanate nanotubes at room temperature, the band gap has been estimated to be ca. 3.87 eV [119]. The surface area and porosity of titanate nanofibers produced at temperatures higher than 170 °C is much lower than that of nanotubes [113]. The 1 D architectures attracts the interest to exploit them in the wastewater treatment field [101]. However, the photocatalytic activity of titanate structures strongly depends on the nature of the pollutant, the crystallographic structure, the calcination treatment, and the presence of alkali ions (Na^+ , K^+) in the structure [120]. In this respect, the photo degradation of acetone in air was successfully found to occur by Yu et al. using calcined samples of nanowires at 500 °C [121], these samples showing a photocatalytic activity 1.8 times higher than Degussa P25. Turki et al. [101] reported that H titanate calcined at 400 °C formed of TiO_2 anatase nanotubes to a photocatalyst 4 times more active than P25 for the degradation of formic acid (FA). Also they concluded that any structure involving Na was found to be inert toward the photocatalytic degradation of FA showing the role of sodium as recombination centers for photo generated electron-hole pairs. Bavykin et al. [94] reported titanate nanotubes are more suitable for adsorption of positively charged dyes in contrast to conventional TiO_2 photoanodes in DSSCs. They also mentioned the instability of titanate structures at high temperatures which is a requirement for doctor blade method. Another problem is random orientation of one dimensional structures of the photoanode which inhibits the transport of electron to the FTO [122]. Taccihini et al. [123] applied their nanotube structures synthesized by hydrothermal treatment to DSSC as nanotube, nanotube/nanoparticle, nanorod and nanorod/nanoparticle. The highest efficiency was yielded by cells consisting only nanotubular structure.

2.4.2 Hydrothermal synthesis of TiO₂ nanostructures using acid catalyzer

Anatase, rutile or brookite TiO₂ nanocrystallites are reported to be synthesized using hydrothermal method with amorphous TiO₂, TiCl₄, TiOCl₂ aqueous solution, and titanium alkoxides via acidic hydrothermal process [124, 125, 126, 127]. The catalyzer type, pH, dwell time and temperature are important for the final morphology and crystal structure [124, 128]. Thermodynamically most stable phase of TiO₂ is rutile which can be obtained by high temperature calcination of the kinetically stable anatase phase. However, the calcination unavoidably causes sintering of the nanocrystallites. Many reports suggested that hydrothermal methods under acidic conditions were applicable for synthesis of rutile nano particles, as well as anatase and brookite nano particles. Yanagisawa and Ovenstone [129] reported that hydrothermal process using an amorphous TiO₂ suspension prepared by neutralization of TiCl₄ and by hydrolysis of Ti(OC₂H₅)₄ under acidic conditions using HCl (0.5 M) led to the formation of a mixture of anatase, brookite, and rutile phases in nanosize. Aruna et al. [130] reported the synthesis of 20 nm rutile nanocrystallites with titanium isopropoxide in the presence of nitric acid (pH 0.5) under vigorous stirring during hydrothermal treatment. Furthermore, Yin et al. [124], reported phase-pure TiO₂ nanocrystallites with narrow particle-size distributions by hydrothermal processes starting from amorphous TiO₂. They reported that autoclaving amorphous TiO₂ in the presence of HF and HCl as cooperative catalyzers led to the formation of narrow-sized anatase TiO₂, nitric acid as a cooperative catalyzer with HF also gave the anatase TiO₂ with a narrow size distribution but with a rather irregular crystalline surface, while amorphous TiO₂ was converted to phase-pure rutile TiO₂ nanocrystallites by autoclaving in the presence of citric and nitric acids. Andersson et al. [131] treated microemulsions with different acid catalyzers which are HCl and HNO₃ and concluded that if hydrochloric acid was used, the rutile structure formed, and if nitric acid was used, anatase formation occurred. Nian and Teng [132], synthesized anatase nanorods using HNO₃ aqua solution of H₂Ti₂O₅·H₂O nanotubes as precursor of hydrothermal process. Dai et al. [133] obtained pure anatase

nanoparticles in the lower HCl concentration (0.1-1 M) and 8 M HCl, a mixture of rutile and anatase in the 2 M to 7 M acidic concentration using cetyltrimethylammonium bromide surfactant agent (Hex-ncTiO₂/CTAB). Zhou et al. [134] synthesized rutile nanostructures with different morphologies by changing the acid molarity of hydrothermal precursor solution containing tetrabutyl titanate. HCl molarity varied between 1 and 10, aggregations, microspheres, nanoflowers, nanotrees, and nanobelts were formed. Wilson et al. [135] reported anatase and brookite binary phase resulted in HNO₃ assisted microwave hydrothermal process. Also they concluded that microwave limits Oswald ripening which provides nanoparticles with small diameters. Wang et al. [136] prepared solutions by hydrolysis precipitation with a water:alkoxide ratio of 165. After recovery and drying, these samples were hydrothermally aged at 180 °C in an acid-free solution for 1 day, 1 M HNO₃ solution for 1 day, 1.5 M HNO₃ solution for 1 day, and 1 N HNO₃ solution for 7 days which were resulted in anatase, anatase-rutile, rutile-anatase and rutile formation, respectively. Dai et al. [137] demonstrated that well-defined anatase TiO₂ nanocrystals with exposed {001} facets could be synthesized in high yields by controlling the hydrolysis rate of the sol-gel precursor and acid assisted hydrothermal treatment. Authors mentioned the importance of pH value of the medium used for hydrothermal treatment which played an important role in controlling the morphology of the obtained TiO₂ nanocrystals. Grimes and co-workers reported the hydrothermal/solvothermal synthesis of rutile TiO₂ nanorods of 10–35 nm diameter from a toluene/HCl (10 M) mixture using a sol-gel-derived TiO₂ seed layer on F-SnO₂ (FTO) [138]. Liu and Aydil firstly reported growth of TiO₂ rutile nanorods on the surface of FTO glass with hydrothermal method with 1:1 volume of HCl and water facilitating the lattice mismatch between FTO and TiO₂ [139]. Hosono et al. [140] discussed the recrystallization process i.e. dissolve and grow process of TiO₂ nanostructures by hydrothermal process. The hydrolysis reaction in strong acidic media can be explained as follows [140]:





Erdogan et al. [141] synthesized rutile TiO_2 nanoflowers using TTIP precursor, strong HNO_3 catalyzer and covering the hydrothermal vessel by titanate structures at relatively lower temperatures.

Both anatase and rutile can grow from the $[\text{TiO}_6]$ octahedra, and the phase formation proceeds by the structural rearrangement of the octahedral. As anatase structure involves more Ti atoms, in the presence of NO_3^- ions which has higher affinity to Ti atoms, anatase formation is reported more favorable [142]. Anatase formation under strong acidic hydrothermal conditions may be explained by dissolution and recrystallization and/or instu transformation [143]. An alternative interpretation of the Ostwald Step Rule has that the first phase to form will be the one possessing the least surface energy with respect to the reactant [144]. Although rutile is the most stable phase, anatase formation may be favored in hydrothermal system due to less surface energy of this polymorph compared to rutile [15]. It was observed that high pH favors anatase, low pH favors rutile, while intermediate pH and reactant concentration stabilize the brookite phase [145]. The three kinds of phase-pure TiO_2 exhibit their distinctive crystal shapes: rounded nanocrystals for anatase, nanoplates for brookite, and nanorods for rutile [146]. Brookite structure has both shared edges and corners and is midway between those of anatase and rutile in terms of the shared edges (four for anatase, three for brookite, and two for rutile) [145]. This might be the reason why brookite needs intermediate pH to stabilize. Pottier et al. [147] suggested that the Cl^- ions in the reaction system template the growth of brookite structure.

Some of the brookite research with hydrothermal process claims that basic media is important for brookite formation [16] such as Keesmann [148] was the one who firstly synthesized pure brookite by hydrothermal treatment of amorphous TiO_2 obtained by hydrolysis of titanium tetraisopropoxide or

alkaline titanates, in the presence of a solution of NaOH containing 3–25 atoms % of Na with respect to total amount of Ti and Na. Na⁺ ions were claimed to stabilize the lattice of brookite but Schwarzmann and Ognibeni [149] synthesized well crystallized brookite by hydrothermal treatment of TiO₂ and H₂O between 100 and 300 °C in the absence of Na⁺ ions. Additionally, brookite was obtained by milling anatase-phase powders. Wakamatsu et al. [150] synthesized almost single phase brookite after 54 ks and 72 ks ball milling of anatase under the condition of medium intensity. Brookite nanoflowers consisting of single crystalline nanorods were prepared by hydrothermal treatment of a solution containing titanium butoxide. Single-phase brookite was extracted from the suspension by centrifugal separation. It is worth noting that the final products of several syntheses reported in the literature are not really single phase brookite since they contain traces of anatase or rutile, as clearly evidenced by the XRD patterns [151]. The existence of brookite in the resultant powders is readily discernible from its (121) diffraction located at 30.81° (2θ) in the XRD pattern, where no overlapping of this peak with any one from anatase or rutile occurs. To claim phase-pure brookite, however, attentions should be paid to the brookite (121) and (120) peaks, as the strongest diffraction from anatase ((101), d=0.352 nm), if there is any, overlaps with the strongest diffraction from brookite ((120), d=0.351), and this may alter the apparent $I_{\text{brookite (121)}} / I_{\text{brookite (120)}}$ intensity ratio. Ideal brookite has a $I_{\text{brookite (121)}} / I_{\text{brookite (120)}}$ ratio of 0.9 (JCPDS: 21-1276) [16].

2.4.3 Doping of TiO₂ nanostructures with metal and nonmetals

Among the three polymorphs of TiO₂, anatase has been widely investigated due to its photo reactivity in catalytic applications [152]. This phase is very popular in optoelectronic applications due to easy mobility of charge carriers in the crystal structure [153]. However, in comparison to anatase TiO₂, rutile is less reactive owing to its higher recombination rate of electron–hole pairs and also a lower surface affinity for many organic compounds [15]. It is well known that

thermodynamically, rutile is more stable than anatase and could be more efficient in visible light induced photocatalytic processes because of the lower band gap as compared to anatase [154]. Recent publications have shown that surface and morphological modifications and doping or co-doping TiO₂ with transition metals, alkaline earth elements, and non-metals improve the photocatalytic activity of rutile phase of TiO₂ [155]. In Figure 2.7, charge separation mechanisms according to different metal or non-metal doping conditions were illustrated.

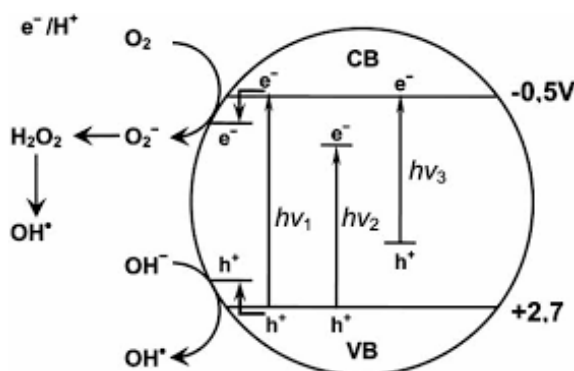


Figure 2.7 Mechanism of TiO₂ photocatalysis: $h\nu_1$: pure TiO₂; $h\nu_2$: metal-doped TiO₂ and $h\nu_3$: nonmetal-doped TiO₂ [156].

Many different strategies were applied to TiO₂ in order to shift the absorption spectrum through red side and prevent recombinations such as metal-ion doping (using transition metals: Cu, Co, Ni, Cr, Mn, Mo, Nb, V, Fe, Ru, Au, Ag, Pt) [157, 158, 159, 160], reducing TiO_x photocatalysts [161], non-metal doped-TiO₂ (N, S, C, B, P, I, F) [158, 162, 156], composites of TiO₂ with semiconductor having lower band gap energy [163], sensitizing of TiO₂ using dye with high photoconversion efficiency [164], establishing heterojunctions to inhibit recombinations and doping with upconversion luminescence agent [158, 165].

There are three different main opinions regarding modification mechanism of TiO₂ doped with nonmetals which are band gap narrowing, impurity energy levels placing, and oxygen vacancies [156]. Sato [166] first reported the shift of the TiO₂

absorption threshold into the visible region observed upon calcination of $\text{Ti}(\text{OH})_4$ in the presence of NH_4Cl (or aqueous NH_3) impurities before fifteen years Asahi et al. [167] reported the revolutionary paper which had opened a new generation to semiconductor materials, mainly represented by TiO_2 doped with non metal elements. In particular the oldest method to prepare N-doped TiO_2 materials is annealing of TiO_2 powders under NH_3 flux (gas) at 500–600 °C, eventually followed by partial reoxidation in air [168]. Burda et al. [169] succeeded in the preparation of N-doped TiO_2 by nitridation of TiO_2 colloidal nanoparticles with alkylammonium salts at room temperature. Some other alternatives are as following N-doped TiO_2 nanomaterials were synthesized by hydrolysis of titanium tetraisopropoxide in a water/amine mixture and post treatment of the TiO_2 sol with amines [170], or by ball milling of TiO_2 in a NH_3 aqueous solution [171]. However, it is still controversial where the N atoms sit. Experiments accompanied by density functional theory (DFT) calculations show different results for settlement of N atom in TiO_2 lattice both for substitutional and interstitial placement [172]. Comparison of N dopant effect on photoactivity is problematic. Because each process provides different settlement of N in the lattice both in surface and bulk. Also, because of different structures and densities of two different polymorphs, N-doping produces opposite effects on the absorption properties of anatase and rutile TiO_2 , leading to a red shift and a blue shift, respectively, of the absorption band edge as given in Figure 2.8 [92] Some research groups suggested that the redshift of band gap of nitrogen-doped TiO_2 originates from the localized states of the oxygen deficiencies caused by nitrogen doping, rather than from the nitrogen dopant itself [173].

Doping TiO_2 with 3d transitional metal ions has been investigated extensively for shifting the photo response of TiO_2 into the visible region by narrowing the band gap while inducing new intermediate energy levels and trapping charge carriers to inhibit recombination [157, 174]. Among various dopants, the similar radii of Mo^{+6} and Fe^{+3} (0.073 and 0.069 nm, respectively) to that of Ti^{4+} (0.075 nm) makes them

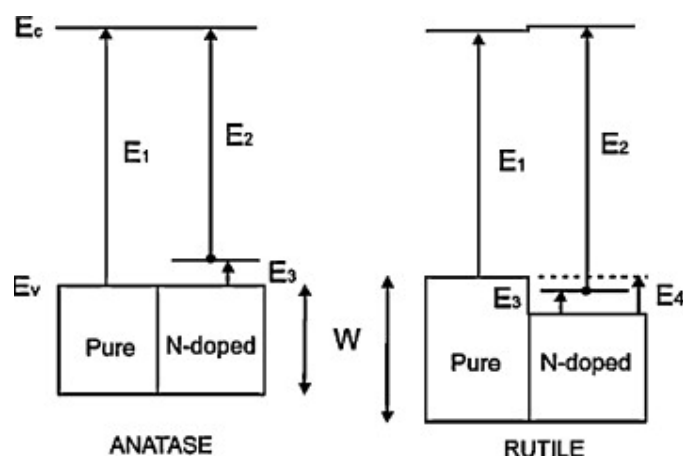


Figure 2.8 Schematic representation of the band structure of pure and N-doped anatase and rutile TiO_2 [92].

attractive for TiO_2 doping because of low or no lattice distortion [158]. Although single element doping reduces the band gap of TiO_2 to some extent, it suffers from the existence of a carrier recombination center and the formation of strongly localized d states within the band gap, which significantly reduce carrier mobility. Thus, co-doping of metals and non-metals has been tried to increase the efficiency of TiO_2 in several studies [175, 176]. Kubacka et al. [177] synthesized W and N co-doped anatase TiO_2 possessing both quite high activity and selectively in the gas-phase partial oxidation of aromatic hydrocarbons under visible light irradiation in the presence of molecular oxygen as the oxidant. Liu et al. [178] prepared a series of samples using sol-gel method and found that Mo and N passivated co-doping contributes to increase the dopant concentration and create more impurity bands in the band gap of TiO_2 thus increasing visible light photocatalytic activity. Yin et al. [179] and Long et al. [180] based on DFT calculations, separately proposed that the injection of 3d or 4d transition metals (such as Mo, W and V) can increase the solubility limits of N and the band edges of TiO_2 can be modified by co-dopants to significantly shift the valence band edge up. Zang et al. [181] synthesized Mo and N co-doped TiO_2 nanotubes by anodization method and the synergistic effect of Mo and N extended the absorption of TiO_2 nanotube arrays into the whole visible light region and resulted in remarkably enhanced

photocatalytic activity for the degradation of methylene blue (MB) under visible light irradiation. Liu et al. [182] synthesized Mo and Fe co-doped TiO₂ nano powders by sol-gel method which was recognized to absorb visible light, had higher separation efficiency of photo induced electrons and holes, and possessed higher photocatalytic activity compared to anatase TiO₂. Kim et al. [183] reported Fe-N co-doped TiO₂ synthesized by sonochemical method which displayed enhanced photochemical behavior as compared to commercially well known TiO₂ powder (P25).

2.4.4 Application of TiO₂ in DSSC

After discovery of DSSC, research towards semiconductor layer as photoanode of DSSC have boomed. TiO₂ is a good candidate among various oxides due to highly availability, nontoxicity, low cost, stability, large surface area, proper internal network structure for charge collection and transportation, and proper band alignments for electron injection from most successful dyes. Many various morphologies such as nanorods [184], nanotubes [185], nanospheres [186], nanofibers [187], nanoflowers [188] in anatase, anatase-rutile, rutile, brookite, anatase-brookite, rutile-brookite and anatase-rutile-brookite crystal structures have been conducted for better efficiency in terms of TiO₂ application. The trend of using TiO₂ in other morphologies instead of nanoparticles as photoanode film of DSSC has raised for inhibiting recombination in grain boundaries which are easily trap the charge carriers. Recombination causes decrease in the carrier mobility and the carrier lifetime. In the nanoparticle-based DSSCs, therefore, the carrier transport is a trap-limited diffusion process and the electron diffusion coefficient is several orders lower than the expected value which is deduced from the physical properties of the single crystalline bulk TiO₂. Electron transport in a given oxide semiconductor is faster in one-dimensional structures compared to nanoparticle based films. Also the one dimensional structures have excellent scattering ability. Composites, heterojunctions, bi-layers of different morphologies of TiO₂ in different crystal structures with different materials like multi walled carbon nano

tube (MWCNT) [189], graphene [185], Ag nano wires [190], Nb₂O₅ [191] etc. were also studied for more efficient DSSCs. That is, TiO₂ sea-urchin like assemblies composed of single crystalline nanoribbons were deposited on nano particle layer. 5.6 % conversion efficiency was yielded. In this study cold isostatic press (CIP) was used to decrease adhesion problems between layers [192]. Zhang et al. [186], built a photoanode which is a composition of P25 nano particle as an under layer and TiO₂ hollow spheres as top layer of photoanode. The cell revealed 5.13 % efficiency which is higher than that of pure P25 layer. Song et al. [185], formed bi-layer photoanodes which includes TiO₂/graphene composite as down layer and nanotubes as top layer and harvested 6.29 % efficiency. Graphene was found to enhance electron transfer while decreasing efficiency due to light absorption. Sun et al. [184] reported that their 1D-3D bilayer photoanodes demonstrated the highest energy conversion efficiency of 7.2 % for rutile TiO₂ dye-sensitized solar cells with TiCl₄ post-treatment. Song et al. [193], applied hierarchical flower-like CeO₂ microspheres and ALD deposited TiO₂ particles onto TiO₂ photoanode and obtained a 9.86 % overall efficiency. Mali et al. [188] synthesized vertically aligned nanorods onto FTO glass under the nanostar 3D structure using hydrothermal process. The authors reported 5.39 % efficiency higher than 3.74 % with single rod layer. Wang et al. [194] reported TiCl₄ treated 1D nanorod/3D nanotubes composite photoanode of DSSC which has a 7.68 % efficiency. Chen et al. [195] reported 7.0 % efficiency using 3D hollow nanostructures on top of P25 nanoparticles which is more than 4.8 % efficiency by P25 single layer photoanode. Doping is another strategy for enhanced efficiency of DSSCs. Various metal (Er, Yb, Zn, Co, Nb) [196, 197, 198, 199] and nonmetal (C, F, N, I, S) [200, 201, 202, 203] doping and/co-doping of TiO₂ are also reported to increase the efficiency of DSSC. Based on the Nb doping study, a positive shift of conduction band minimum (CBM) is reported to increase e⁻ injection and transport by a particular amount of doping. V_{oc} is affected in two different ways. First, the positive shift of CBM leads to decrease V_{oc}. Second, Nb doping would increase by suppressing the recombination between TiO₂ and electrolyte interface which increases voltage [204]. Ko et al. [205] reported Al-W co-doping enhances

conversion efficiency compared to mono-doped and undoped powders. They suggested that electrochemical effects stem from altered surface electronic states such as surface polarity and defect charge balancing.

CHAPTER 3

EXPERIMENTAL

In this chapter, laboratory experimental procedure for the synthesis of titanate and TiO₂ nanopowders via hydrothermal method was described. DSSC fabrication steps were explained under the subsection of DSSC fabrication. Details for the characterization of powders, photocatalytic activity tests and efficiency measurements were given in the subsection of characterization and property measurement.

3.1 Powder synthesis via hydrothermal method

Hydrothermal synthesis of nanostructures were accomplished using a high pressure reactor (ITO Instruments[®] I max. 120 bar and 250 °C) with a Teflon lined hastalloy vessel. The reactor has a mechanic stirrer made of Teflon, which can be set between 0 and 1500 rpm. Pressure inside the reactor changes autogenously according to the filling amount, solvent type and temperature of the treatment. A water cooling system covered by Teflon works for temperature set up. Hydrothermal synthesis in this study was conducted in two different conditions according to the catalyzer type. HNO₃ was used as acid catalyzer for acid assisted experiments and NaOH was used as base catalyzer for base assisted hydrothermal synthesis.

3.1.1 Base assisted hydrothermal synthesis

All chemicals were purchased and used in this study was tabulated in Table 3.1. Synthesis of hydrothermally derived titanate nanostructures was conducted following the study done by Kasuga and co-workers [96] with some modification

as illustrated in Figure 3.1. First, 10 M NaOH aqua-solutions were prepared (70 mL) freshly before every hydrothermal synthesis. 2 g P25, commercial anatase powder, and amorphous powder were dissolved in as prepared basic solution separately using a magnetic stirrer for 30 min. After dissolution process, solution was homogenized by sonication. Then, the solution was taken to the hastalloy vessel of autoclave without Teflon lining. Hydrothermal synthesis was conducted for 3 different duration times (12, 24, 36 h) at 130 °C while mixing at 450 rpm.

Table 3.1 Supplier and product number of chemicals used for synthesis of the nanostructures.

Materials	Supplier (Product code)
NaOH (98 %)	Sigma Aldrich (06203)
P25 [®] (Degussa) (99.5 %)	Aldrich (718467)
Anatase (99.6 %)	Alfa Aesar (036199)
Amorphous TiO ₂ powder	Laboratory product
HCl (37 %)	Merck (100317)

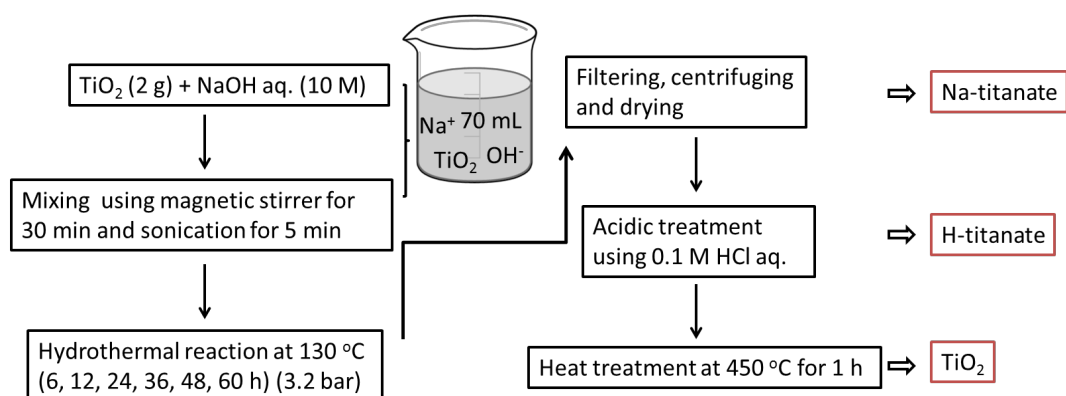


Figure 3.1 Schematic illustration of 1 D TiO₂ synthesis following titanate production by base assisted hydrothermal synthesis.

After hydrothermal synthesis, solution was filtered by washing with distilled water until pH becomes neutral. Then, the filtered solution was centrifuged at 5500 rpm for 10 min and dried at 80 °C for 24 h. 0.3 g of prepared powder was separated.

Remained powder was treated with 120 mL of 0.1 M HCl solution at 40 °C under magnetic stirring, washed with distilled water, centrifuged and dried. 0.3 g of the powder was separated again. Remaining powder was treated with 0.1 M acidic solution of 90 mL, treated with distilled water, centrifuged and dried. 0.3 g powder was separated again. Remaining powder was treated with 0.1 M acidic solution of 60 mL, washed with distilled water, centrifuged and dried. 0.3 g powder was separated once more. After that, remaining powder was calcined consistent with following procedure; heated to 450 °C with a heating rate of 5°/min and kept at this temperature for 1 h then cooled to room temperature with a cooling rate of 5 °C/min.

Coding of powders with respect to applied processes was tabulated in Table 3.2 (The letter P signifies P25 was used as beginning powder. Letter A indicates amorphous powder and no letter means anatase beginning powder was used, first number: hydrothermal dwell time, second number acid washing repeat and if the sample was calcined then the C letter was used in the coding). Appearance of some of the representative powders synthesized are shown in Figure 3.2.

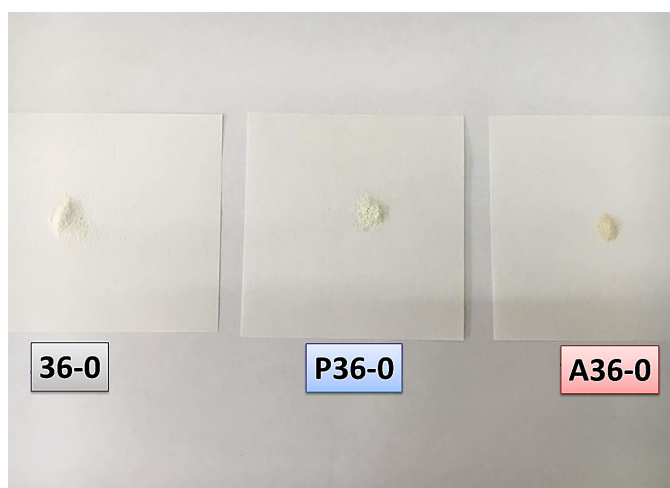


Figure 3.2 Some of the products synthesized by hydrothermal treatment.

Table 3.2 Coding of the samples with respect to their synthesis procedure.

Code	Precursor	Hydrothermal dwell time (h)	Acid washing times	Calcination at 450 °C
P6-0	P25	6	0	-
P6-2	P25	6	2	-
P12-0	P25	12	0	-
P12-2	P25	12	2	-
P24-0	P25	24	0	-
P24-2	P25	24	2	-
P36-0	P25	36	0	-
P36-2	P25	36	2	-
P48-2	P25	48	2	-
P60-2	P25	60	2	-
PC24-0	P25	24	0	+
PC24-1	P25	24	1	+
PC24-2	P25	24	2	+
PC24-3	P25	24	3	+
PC36-2	P25	36	2	+
6-0	A*, t*	6	0	-
6-2	A, t	6	2	-
12-0	A, t	12	0	-
12-2	A, t	12	2	-
24-0	A, t	24	0	-
24-2	A, t	24	2	-
36-0	A, t	36	0	-
36-2	A, t	36	2	-
36-3	A, t	36	3	-
36-4	A, t	36	4	-
C36-2	A, t	36	2	+
A6-2	Am*, t	6	2	-
A12-0	Am, t	12	0	-
A12-2	Am, t	12	2	-
A24-0	Am, t	24	0	-
A24-2	Am, t	24	2	-
A36-0	Am, t	36	0	-
A36-2	Am, t	36	2	-
A48-0	Am, t	48	0	-
A48-2	Am, t	48	2	-
AC36-2	Am, t	36	2	+
AC48-2	Am, t	48	2	+

A: Anatase, t: titania, Am: Amorphous

3.1.2 Acidic hydrothermal synthesis

Two different experimental studies were designed to synthesize the nanostructures. First, a set of experiments with 27 hydrothermal run by changing time, temperature, and acid molarity was done to understand the effect of time, temperature, and acid molarity on the morphological and structural behavior of 0D and 1D TiO₂ nanostructures. The second group involves 5 experiments that were done to investigate the effect of co-doping. Experiments were carried out in conjunction with the work reported by Liu and Aydil [139] though some modifications were made in the experimental procedure. An aqueous solution of HNO₃ was taken as the solvent for the hydrothermal synthesis. Chemicals used for the study was tabulated in Table 3.3.

Table 3.3 Supplier and product number of chemicals used for synthesis.

Materials	Supplier (Product code)
Titanium(IV) isopropoxide (97 %)	Aldrich (205273)
HNO ₃ (65 %)	Merck (100456)
Distilled water (15MΩ.cm)	Laboratory
Iron(III) nitrate nonahydrate ≥ (99.95 %)	Aldrich (254223)
(NH ₄) ₆ Mo ₇ O ₂₄ in H ₂ O	Merck (170227)

For the first experiment group, titanium tetra isopropoxide (TTIP) (Aldrich 97%) was used as precursor for all experiments. First, concentrated HNO₃ (Aldrich 70%) was diluted with distilled water (0.06, 0.2 and 1 HNO₃/H₂O volume ratio) to get the acid molarity of 1 M, 3 M, or 8 M. Then, 10 ml of TTIP was dissolved in the freshly prepared diluted HNO₃ solution under magnetic stirring at 300 rpm for 15 min. The resultant homogenous, clear, and transparent solution of 200 mL was transferred into the vessel of the high pressure hydrothermal reactor. The capacity of the vessel was 300 mL. Pressure during synthesis was autogenously varied between 10 and 60 bars depending on the acid concentration and synthesis temperature applied. Hydrothermal synthesis was done for 27 times for 3 different temperatures and 3 different dwell times which are 110, 140, 180 °C and 1, 3, 6 h,

respectively. After hydrothermal synthesis, the nanostructures synthesized was filtered, washed with distilled water several times until pH becomes neutral, centrifuged, and dried for 6 h at 60 °C. Schematic illustration of synthesis procedure is shown in Figure 3.3.

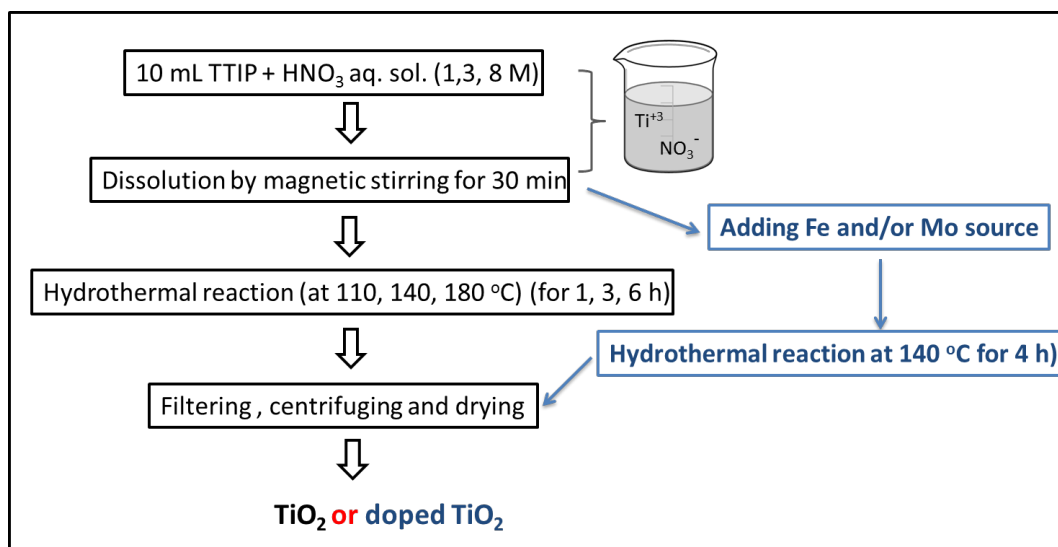


Figure 3.3 Flowchart showing synthesis of TiO_2 nanostructures by acid assisted hydrothermal process.

Code of the samples and the process parameters used during hydrothermal treatment are given in Table 3.4. The powders gathered by drying the 8M acidic TTIP aqua solution at 60 °C for overnight, coded as N800, was taken as a reference sample to clarify the evolution mechanism of the nanostructures during hydrothermal synthesis. One more sample was synthesized using 8 M acid catalyzer at 140 °C for 3 h inserting H-titanate structure to the system. H-titanates were spray coated inside the hastalloy vessel. Spray coating was firstly tried on a glass substrate. 2.5 mg/L titanate powder and ethanol (balance) were mixed and sonicated. Then, a controlled volume (10 mL) of the mixture was spray coated on a glass substrate having 1 cm surface area. The thickness of the film was measured by FESEM analysis (100 nm). After that, the amount was modified according to the exposed surface area of autoclave vessel. The letters N and H in the codes

stand for HNO₃ catalyzer and protonated H-titanate nucleation seed inputs, respectively. The first, second, and third integers in the codes are for the acid molarity, synthesis temperature, and synthesis time, respectively.

Table 3.4 Sample coding in terms of their synthesis conditions.

Code of the sample	Acid Molarity (M)	Synthesis Temperature (°C)	Hydrothermal Dwell Time (h)
N111	1	110	1
N113	1	110	3
N116	1	110	6
N141	1	140	1
N143	1	140	3
N146	1	140	6
N181	1	180	1
N183	1	180	3
N186	1	180	6
N311	3	110	1
N313	3	110	3
N316	3	110	6
N341	3	140	1
N343	3	140	3
N346	3	140	6
N381	3	180	1
N383	3	180	3
N386	3	180	6
N811	8	110	1
N813	8	110	3
N816	8	110	6
N841	8	140	1
N843	8	140	3
N846	8	140	6
N881	8	180	1
N883	8	180	3
N886	8	180	6

The second set of experiments was conducted by adding Mo and Fe nitrate solutions to the recipe. The amounts of precursor, HNO₃, water, Mo and Fe solutions were modified in order to obtain 8 M HNO₃ in the solution. Mo standard

solution and Fe III nano nitrate nonahydrate were added after dissolving of TiO₂ in the HNO₃ aqua solution. Experimental procedure was included with blue letters in Figure 3.4. Time and temperature parameters were remained the same as 4 h and 140 °C, respectively. Teflon lined vessel was used. Mo standard solution was added as 0.0378 L for 0.0378 g Mo and 0.076 L for 0.076 g Mo (1 and 2 wt % of 3.78 g TiO₂). Fe III nano nitrate nonahydrate was used 0.149 g for 0.019 g and 0.298 for 0.038 Fe (0.5 and 1 wt % of 3.78 g TiO₂). Coding of samples is given in Table 3.5.

Table 3.5 Code of Mo and Fe doped TiO₂ powders.

Sample	Doped metal content wt %	
	Molybdenum	Iron
Mo0Fe0	0	0
Mo1Fe0	1	0
Mo2Fe0	2	0
Mo2Fe0.5	2	0.5
Mo2Fe1	2	1

3.2 DSSC assembly

Semiconductor film on FTO glass was achieved by scotch printing of pastes which are composed of semiconductor nano powders dispersed in an organic based high viscosity fluid. The particles and fluid are blended together to form a mechanically and chemically stable material before sintering. The materials used for DSSC assembly are tabulated in Table 3.6.

Table 3.6 Materials used for DSSC fabrication.

Materials	Company (Product Number)
TiO ₂	Laboratory
Ethyl cellulose (46 % ethoxyl)	Aldrich (200670)
α -Terpineol (90 %)	Aldrich (432628)
Acetic acid (100 %)	Merck (100056)
Ethanol (96.0-97.2 %)	Aldrich (24105)
Citric acid (99 %)	Aldrich (C0759)
Titanium(IV) isopropoxide (97 %)	Aldrich (205273)
Titanium(IV) chloride (97 %)	Fluka (89545)
Surlyn film (50 μ m)	DuPont
FTO (20-30 Ω /sq)	Solaronix
N719	Solaronix
Iodolyte HI-30	Solaronix
Chloroplatinic acid hydrate (\geq 99.9 %)	Aldrich (520896)

3.2.1 Photoanode preparation

3.2.1.1 Paste preparation

Powders tabulated in Table 3.7 was used for DSSC application. Paste preparation was done applying the same method with Grätzel and coworkers with some modifications [206]. The TiO₂ powders were grinded using acetic acid, water and ethanol, respectively. Dispersions in the mortar were transferred with excess of ethanol (40 ml) to a beaker and stirred with a 2 cm long magnet tip at 350 rpm. The ultrasonic homogenization was performed. α -terpineol and the mixture solution of two ethyl celluloses in ethanol were added, followed by stirring and sonication. Pechini method was used for one powder (N846) as suggested by Ronconi et al. [207]. The pechini batch was obtained using a precursor molar ratio of 1:4:16 [Ti(iOPr)₄:citric acid:ethylene glycol]. The solution was prepared by heating ethylene glycol to 60 °C and during stirring the TTIP was added. Finally, citric acid was added and the temperature increased to 90 °C. The solution was stirred at this temperature until it turned clear. The paste has been prepared by mixing the TiO₂ powder and sol–gel solution in a mortar grinder for 1 h. The

molar ratio between TiO₂ and TTIP was 7:1. The contents in dispersion were concentrated by evaporating the ethanol on hot plate at 40 °C for both process. At each step, liquids were added drop by drop into a porcelain mortar and/or beaker. The condition was in the ambient air at room temperature. The coding of pastes was given in Table 3.7

Table 3.7 Coding of pastes according to powder content and formation method.

Code	Powder	Formation method
PN116	N116	Grätzel
PN843	N843	Grätzel
PN846	N846	Grätzel
PHN843	HN843	Grätzel
P1-2D	A36-2(50 wt %)+A48-2(50 wt %)	Grätzel
PN846-p	N846	Pechini
PN846-t	N846	Grätzel+TiCl ₄ treatment

3.2.1.2 Cleaning FTO glasses

Fluorine doped tin oxide (FTO) glass was cut into 2 x 1.5 cm² pieces. Each of the pieces was cleaned with the following procedure:

- Sonicate in soap solution – 15 min.
- Rinse with copious distilled water.
- Sonication in acetone – 5 min
- Sonication in ethanol - 5 min

3.2.1.3 Applying paste on FTO

A 0.5×0.5 cm² window was cut in a piece of Scotch Magic tape (~30 μm for single layer and ~50-60 μm thick for bi-layer photoanodes) and put on the conductive side FTO glass. A thin film of nano-crystalline TiO₂ was applied onto the

conducting glass by ‘doctor blading’ with a stainless steel blade. The paste was stirred manually before use, but shaking the bottle itself would cause air bubble formation preventing good deposition. The tape was removed carefully and the paste was allowed to relax for 30 min in a covered petri. The latter was a critical step as it allows reducing surface irregularity and brings the air bubbles out. Plastic and glass lab ware were used as much as possible in every steps of the fabrication, to prevent contamination. The thickness was measured with a surface profilometer (Mitutoyo Surf Test SC470).

3.2.1.4 Sintering

The TiO₂ coated substrates were put on a glass plate inside a glass tube, and heated with kantal heating elements under air atmosphere. The temperature was precisely controlled with a Eurotherm 2208e temperature controller. The benchmark temperature profile was shown in Table 3.8.

Table 3.8 Heat treatment program used for the sintering of pastes.

Temperature (°C)	Time (min)
25-325	55
325-325	5
325-375	10
375-375	5
375-450	15
450	15
450-500	10
500	15
500-80	Naturally

3.2.1.5 Dye loading

Dye solution was prepared solving N719 dye in ethanol for 0.5 mM dye solution. The solution was kept in refrigerator. The dye solution is always needed to be stored away from light. The electrodes taken from furnace at 80 °C were immersed

in the dye solutions and then kept at room temperature for 12 h to adsorb the dye onto the TiO₂ surface. After taking away the electrodes, they were used as photoanode of the cell. Dye desorption was done by dipping dye loaded photoanodes into 0.1 NaOH aqua solution for a few seconds.

3.2.2 Counter electrode preparation

Two 0.8 mm diameter holes were drilled on a piece of 1.7×1.5 cm² FTO glass. The substrate was cleaned similarly with working electrode. The cleaned substrate is heated for 15 min at 450 °C to remove the residual organic contaminants. Then, H₂PtCl₆.H₂O was dissolved in 2-propanol to form 10 mM Pt solution. The solution was spin coated on the surface of FTO glass. Spinning was applied as 1200 rpm for 5 s. The electrode was heated immediately at 450 °C for 30 min, activating the platinum layer for working. The activated electrodes were instantly used for cell making not to lose catalytic effect.

3.2.3 Cell fabrication

The working and counter electrode were sealed using a film (Surlyn ® 1702 hot melt foil from DuPont). Surlyn ® is an ionomer with a melting point of about 90 °C. The thickness of the foil used in a standard DSSC was 50 µm. The foil was stored at least one day in a desiccator before the cell was sealed. Otherwise water adsorbs on the surface, which decreases the adhesion to the FTO-substrate. After putting surlyn on top of the working electrode, counter electrode was put onto the working electrode. Then the cell was exposed to heat using a heating gun at 100 °C. After sealing process electrolyte was filled from the one hole on the counter electrode after taking out the air from the other hole. Then the holes were closed using a piece of foil. The final form of the cell is shown in Figure 3.4.

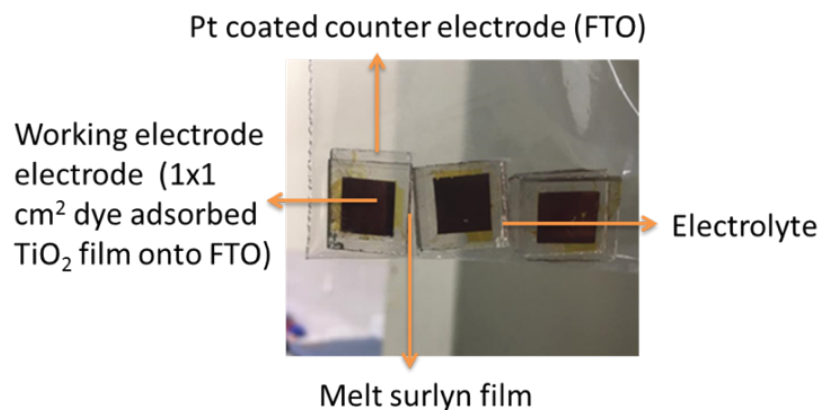


Figure 3.4 Cells prepared for efficiency analysis.

3.3 Powder and electrode characterization and property measurement

3.3.1 X-ray diffraction (XRD) analysis

The crystallographic information of all samples was investigated by powder XRD analysis. XRD patterns were detected using CuK α radiation, $\lambda=1.5406 \text{ \AA}$, 40 kV, 40 mA through an X-ray diffractometer (Rigaku, D/MAK/B.). The samples were prepared in the form of fine homogeneous powder by grinding in a mortar with pestle. A thin smooth layer of the samples mounted on a non-crystalline holder such as fused silica was held in the path of X-rays. The XRD patterns with diffraction intensity versus 2θ were recorded, generally from 20° to 80° at a scanning speed of $2^\circ/\text{min}$. The well-known Bragg's equation is used to determine the interlayer space of the crystals $d = \lambda / (2 \sin \theta)$, where, θ is the diffraction angle. XRD patterns were also analyzed using Rigaku 4.2 software to identify the crystalline phase(s) present in the products. The same amount of powder ($\sim 0.2 \text{ g}$) was used for every analysis. Anatase/rutile ratio was determined with $X_A = [1 + 1.26(I_R/I_A)]^{-1}$ formula, where X_A is the fraction of anatase phase in the mixture, while I_A and I_R are the integrated intensities of the (101) reflection of anatase phase and the (110) reflection of rutile phase. PeakFit® software was used to analyze the

peak areas of powders including brookite phase. The average crystallite sizes, d_{hkl} , was calculated by the Debye Scherrer formula with the full width at half maximum (FWHM) of the peaks $d_{hkl}=0.9 \lambda / (\text{FWHM} \times \cos\theta)$ assuming the crystallites are spherical in shape.

3.3.2 Field emission scanning electron microscopy (FESEM)

FESEM (Nova Nanosem) was frequently used in this study to examine the morphology of the powders synthesized. Operation voltage was changed between 10 to 20 kV. In order to improve the conductivity of the samples, all samples were coated with a thin layer of gold by a sputter coating method. Besides getting the images of the samples, FESEM is equipped with Energy Dispersive X-Ray Spectroscopy (EDS) that provides the information of the elemental composition of samples imaged by FESEM. The EDS microanalysis system collects the X-rays, sorts and plots them by energy, and automatically identifies and labels the elements responsible for the peaks in this energy distribution.

3.3.3 High resolution transmission electron microscopy (HRTEM)

The main point of HRTEM is that a highly focused and monoenergetic electron beam is used to bombard the specimen. The transmitted electrons form images on a fluorescent screen that provide morphological features and atomic arrangements of the samples. For HRTEM, interferences among beams scattered by the crystal in different directions form a “lattice image”.

In this study HRTEM was used to investigate formation mechanism and for clarifying the growth direction, phase-morphology interaction of nano powders. During the specimen preparation, TiO₂ nanostructure materials were dispersed in ethanol and a few drops of such solution mixture were spread on a carbon coated copper grid for analysis in a JEOL 3010 (300kV).

3.3.4 Braunner - Emmett - Teller (BET) surface area analysis

BET method was used to measure the total surface area of the TiO₂ nanostructures. The adsorption data were obtained from this testing. Full adsorption and desorption isotherm of nitrogen on the samples were determined at various pressures and the pore volume and pore-size distribution were calculated with the Barret-Joyner-Halenda (BJH) method. The surface area was measured by Quantachrome NOVA-3000 and all samples were degassed in N at 110 °C for 12 h.

3.3.5 Inductively coupled plasma mass spectrometry (ICP-MS) analysis

Inductively Coupled Plasma Mass Spectrometry (Perkin Elmer DRC II) is a very sensitive and powerful analytical method used to analyze trace elements. The principle of this instrument is that ionized or excited atoms produced by the application of plasma to the sample which are separated and identified according to their mass and charge ratio (m/z). Samples for ICP-MS analysis was prepared by dissolving 50 mg powder in 200 mL HF solution.

3.3.6 X-ray photoelectron spectroscopy (XPS) Analysis

XPS is a quantitative spectroscopic technique that measures the elemental composition, empirical formula, and the chemical state and electronic states of the elements that exist within a material. XPS spectra are obtained by irradiating a material with a beam of aluminum or magnesium X-rays while simultaneously measuring the kinetic energy (KE) and number of electrons that escape from the top 1 to 10 nm of the material being analyzed. Because the energy of a particular X-ray wavelength equals a known quantity, we can determine the electron binding energy (BE) of each of the emitted electrons by using an equation that is based on the work of Ernest Rutherford (1914):

$$E_{\text{binding}} = E_{\text{photon}} - E_{\text{kinetic}} - \Phi \quad (17)$$

where, E_{binding} is the energy of the electron emitted from one electron configuration within the atom, E_{photon} is the energy of the X-ray photons being used, E_{kinetic} is the kinetic energy of the emitted electron as measured by the instrument, and Φ is the work function of the spectrometer. It is important to note that XPS detects only those electrons that have actually escaped into the vacuum of the instrument. The photo-emitted electrons that have escaped into the vacuum of the instrument are those that originated from within the top 10 to 12 nm of the material. All of the deeper photo-emitted electrons, which were generated from the X-rays which penetrated 1–5 micrometers into the material, are either recaptured or trapped in various excited states within the material. For most applications, XPS is a non-destructive technique to measure the surface chemistry of any inorganic compounds, metal alloys, semiconductors, polymers, or catalysts. XPS is a very useful technique especially for multicomponent samples such as the binary metal oxides, such as doped and co-doped TiO_2 , synthesized in this study. The surface composition was determined by X-ray photoelectron spectroscopy (XPS) was performed under ultrahigh vacuum at a pass energy of 93.90 eV on a Specs EA 300 system equipped with a dual X-ray source by using a Mg $K\alpha$ (1253.6 eV) anode and a hemispherical energy analyzer. Survey and high-resolution spectra were obtained using an analysis area of $\sim 300 \times 700$ micrometers and pass energies of 160 eV and 20 eV, respectively. All binding energies were calibrated with contaminant carbon ($\text{C}1s=285$ eV) as a reference.

3.3.7 Differential thermal analysis (DTA) and Thermogravimetric Analysis (TGA)

Thermal analysis is an important technique for the characterization of solid materials, as it provides information on the physical and chemical changes involving endothermic and exothermic processes, temperatures for phase

transitions, melting points and crystallization, and the weight loss when the temperature is increased. Differential Scanning Calorimetry (DSC): DSC is a thermal analysis technique that is used to measure the heat flows associated with transitions in materials as a function of time or temperature. This technique provides both qualitative and quantitative information about the physical and chemical changes that are involved in endothermic processes such as melting, and exothermic processes such as crystallization, or changes in heat capacity such as at the glass transition temperature (T_g). An alternative technique which shares much in common with DSC is DTA. In this method, the heat flow to the sample and the reference remains constant, with the instrument measuring the temperature difference. When the sample and reference are heated, identical phase changes and other thermal processes cause a difference in temperature between the sample and reference. Both DSC and DTA provide similar information; however, DSC is the more widely used technique amongst these two techniques. TGA, another important thermal technique, is widely used for the characterization of solid materials including polymer, organic, inorganic and composite materials. Especially, TGA can be used to determine the percentage of inorganic fillers in inorganic/polymer composites. TGA can determine: (1) moisture/liquid content and the presence of volatile species, (2) decomposition temperatures, and (3) the rate of degradation. TGA, in this work was performed under nitrogen/air atmosphere on a S II Exstar TGA-DTA at a heating rate of 10 °C/min from room temperature to 1000 °C.

3.3.8 UV-Vis Spectrophotometer and Methylene Blue (MB)

Photodegradation Test

UV/Vis spectrophotometer is ultraviolet-visible spectroscopy instrument. It is routinely used in the quantitative determination of solutions of transition metal ions and highly conjugated organic compounds. It measures the intensity of light passing through a sample (I), and compares it to the intensity of light before it passes through the sample (I_0). The ratio I/I_0 is called the transmittance, and is

usually expressed as a percentage (%T). The absorbance A , is based on the transmittance: $A = -\log(\%T)$ The basic parts of a spectrophotometer are a light source where an incandescent bulb for visible wavelengths and a deuterium arc lamp in the ultraviolet. The spectrometer includes a holder for the sample, a monochromator to separate the different wavelengths of light and a detector. The detector is typically a photodiode used with monochromators, which filter the visible light so that only light of a single wavelength reaches the detector. In this thesis, a UV-visible Spectrophotometer Scinco instrument was used, and the scanning rate was 600 nm /min with a wavelength range of 200 -900 nm. Spectra were acquired in transmission mode through the quartz tube at a 300kV accelerating voltage. White blank measurement was performed in accordance with USRS-99-010 standard. The percent reflection against wavelength graph was transformed using the Kubelka–Munk method to an $[\text{eV}]^{1/2}$ against $[\text{eV}]$ graph. Band gap energy of the powder sample was calculated by extrapolating the mid-section of the graph to the x axis. The effect of co-doping on photocatalytic activity was evaluated through degradation of methylene blue (MB) solution under a 100 W UV lamp with a wavelength at 365 nm and continuous stirring using a magnetic stirrer. The distance between the source and the surface of Pyrex container (300 mL capacity) was 5 cm. In order to keep the temperature of the solution constant during the reaction, water was circulated through the annulus of the jacket quartz tube. Photocatalytic tests were done using 100 mL solution. The MB concentration was 10 mg/L with a catalyst loading of 0.5 g/L. Before irradiation, the suspension aqueous solution was stirred continuously in dark for 30 min to ensure adsorption/desorption equilibrium. Initial concentration of MB before dark mixing was used as the initial value for further kinetic treatment of the photodecomposition processes to identify adsorption values. 3 mL samples taken from the solution at regular intervals using a syringe filter (Millex Millipore, 0.22 μm) were analyzed using the UV–Vis spectrophotometer to determine the concentration of MB. The removal efficiency of the photocatalyst was calculated as follows:

$$\eta = (C_0 - C_t) / C_0 \times 100 \quad (18)$$

where, C_0 and C_t are the concentrations of MB at initial and different irradiation times, respectively.

3.3.9 I-V measurements of DSSCs

The photocurrent density–voltage (J–V) measurements of the DSSCs were conducted by a Keithley model 2440 source measure unit. A solar simulator (Newport) equipped with a 100 W Xenon lamp is used as a sun-light source, which light intensity was calibrated by Si solar cell under AM 1.5G one sun light intensity.

3.3.10 EIS measurements of DSSCs

EIS measurements of assembled DSSCs were performed using Gamry EIS 3000 Potentiostat biased to Philips white LED lamp (25 W). The tested areas of samples were 0.25 cm^2 . The signals were collected between 100 kHz and 10 mHz. The scan amplitude was 10 mV and 0.6 V DC current was applied to the cells. According to Gamry tutorial, an equivalent circuit was fitted to the curves including Pt counter electrode-electrolyte interface and TiO_2 -electrolyte-dye interface. EIS analysis was performed to investigate the electronic responses of different elements of the DSSCs. Figure 3.5 shows the fitted equivalent circuit for DSSCs which were proposed by Grätzel et al. [208]. This model only includes the response from the resistance of Pt-electrolyte interface and TiO_2 electrolyte interface. R_1 represents the sheet resistance which is induced by TCO, electrolyte layer and counter electrode, R_2 represents the charge transfer resistances related to recombination of electrons at the Pt electrolyte interface and the electron transport resistance, CPE1 and CPE2 are constant phase elements of two electrode and electrolyte interfaces, C_1 represents capacitance and finally R_3 and R_4 are the charge transfer resistances

associated with recombination of electrons at the TiO_2 electrolyte interface and the electron transport resistance in the system.

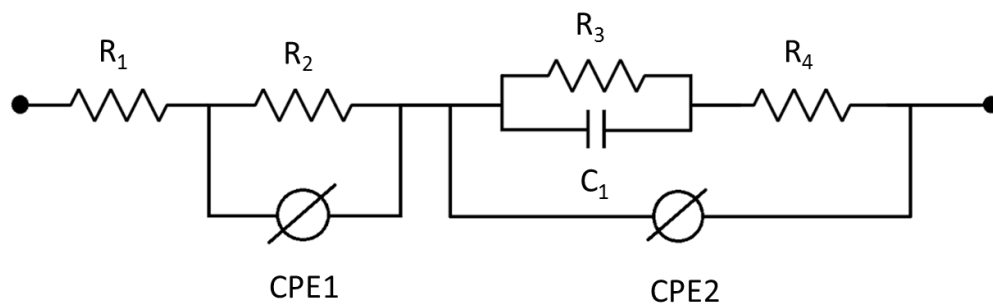


Figure 3.5 Equivalent circuit model used for fitting EIS data [208].

CHAPTER 4

RESULTS and DISCUSSION: SYNTHESSES of ONE DIMENSIONAL TITANATE and TiO₂ NANOSTRUCTURES, THEIR CHARACTERIZATION and PHOTOACTIVITY

4.1 General

One dimensional (1D) titanate and TiO₂ nanostructures are very complex. Reported values for the photoactivity of these structures is controversial. However, one dimensional structures are considered to be a good candidate for optoelectronic applications due to their lower recombination rates achieved by eliminating the grain boundaries. The lower surface area and instability of these structures are important handicaps, which may cause lower efficiency values. So far, these structures are considered non beneficial for DSSC applications although their photocatalytic activity is satisfactory.

This study was carried out to synthesize 1D titanate nanostructures by base assisted hydrothermal treatment. Precursor type and hydrothermal dwell time were changed to get 1D nanostructures with different morphology. An understanding of the effect of hydrothermal duration and precursor type on the final morphology and crystal structure of the products. Also, effect of Na content on polymorphic transformation was investigated by keeping precursor and hydrothermal dwell time constant. The nanostructures synthesized were characterized using microstructural characterization techniques. Photocatalytic tests were done to evaluate the photocatalytic performance of the nanostructures synthesized. Photocatalytic test results were combined with morphological and crystallographic findings to get the most proper and promising nanostructure for the fabrication of DSSC.

4.1.1 XRD analysis

XRD patterns of the selected nanostructures namely; P36-0, 36-0, and A36-0 that were synthesized by base assisted hydrothermal treatment are shown in Figure 4.1

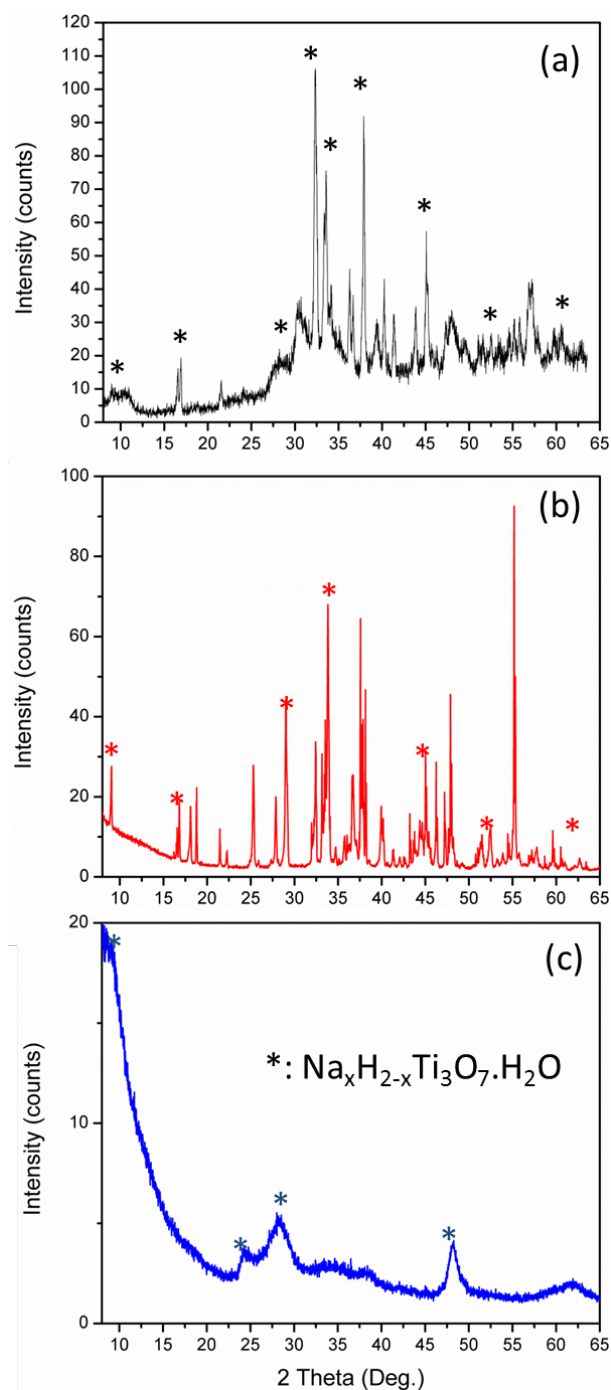


Figure 4.1 XRD patterns of samples (a) P36-0, (b) 36-0, and (c) A36-0.

In order to get only titanate phase in the nanostructures to be synthesized, a hydrothermal treatment temperature of 130 °C was taken into consideration since anatase phase is unstable in a high concentrated alkali solution at 130 °C and transforms into sodium titanate in 2 h [209]. The XRD patterns suggest that different Na titanate structures exist in samples P36-0, 36-0, and A36-0. Although the amount of powders used in the XRD analyses is more or less the same, intensity of the peaks belonging to phases present in sample P36-0 is superior to the other two samples as seen in Figure 4.1. This finding implies that amount of crystalline phases is much more in sample P36-0 than the other two samples. This means that better crystallinity is achieved in sample P36-0 as compared to samples 36-0 and A36-0.

The diffraction peak at 2θ of 9.1° , which belongs to 100 plane of typical layered titanate with a formula of $\text{Na}_x\text{H}_{2-x}\text{Ti}_3\text{O}_7 \cdot \text{H}_2\text{O}$ ($0 < x < 2$, $n < 12$) [94] is detected in all samples. As seen in Figure 4.1 (a), without acidic washing many peaks belonging to Na and/or H titanate compounds appears in the XRD pattern of sample P36-0. Other peaks at 16.5 (101), 25 (110), 27.9, 29 (003), 32.4 (202), 33.9, 38.1 (013), 46 (104), 47.9 (020), 53, 58, and 62° endorse that the sample may contain $\text{Na}_2\text{Ti}_3\text{O}_7$ (JCPDF 72-0148). Also the peaks assumed as $\text{Na}_2\text{Ti}_3\text{O}_7$ may refer to other phases such as $\text{Na}_2\text{Ti}_6\text{O}_{13}$ (JCPDS 73-1398), $\text{NaH}_x\text{Ti}_{2-x/4}\text{O}_4 \cdot \text{H}_2\text{O}$, and/or $\text{H}_2\text{Ti}_2\text{O}_4(\text{OH})_2$ crystalline phases which have analogue peaks with each other indicated in Table 2.3 [94]. Noting that the XRD data cannot unambiguously confirm the structure of the synthesized titanate samples, but are consistent with the formation of $\text{Na}_x\text{H}_{2-x}\text{Ti}_3\text{O}_7$ complex titanates, in agreement with other reported studies [94, 95].

A comparison of the XRD patterns of samples 36-0 and A36-0 verify that amount of crystalline phases presents in sample 36-0 is more than in sample A36-0. See Figure 4.1. A sharp peak belonging to titanate is clearly seen in sample 36-0 as compared to sample A36-0. The same peak broadened in sample A36-0. XRD analyses reveal that sample 36-0 contains similar phases with sample P36-0 ($\text{Na}_x\text{H}_{2-x}\text{Ti}_3\text{O}_7 \cdot \text{H}_2\text{O}$), but sample A36-0 consists of only $\text{Na}_x\text{H}_{2-x}\text{Ti}_3\text{O}_7 \cdot \text{H}_2\text{O}$ phase.

Layered titanate peak at 2θ of 9.1° is identified though it was broadened as is in sample P36-0. The diffraction peaks belonging to anatase or rutile phases were not detected in samples P36-0 and A36-0. Nonetheless, a very small peak of anatase (101) plane was noticed at 2θ of 25.2° in sample 36-0.

XRD patterns of the protonated titanates obtained using different precursors after hydrothermal treatment are seen in Figure 4.2. All samples show titanate tubular structure $\text{Na}_x\text{H}_{2-x}\text{Ti}_3\text{O}_7 \cdot \text{H}_2\text{O}$ at 2θ of 9.1° with varying intensities. The “x” value may be 0 or not. The highest intensity is sensed in sample 36-2 as shown in Figure 4.2 (b).

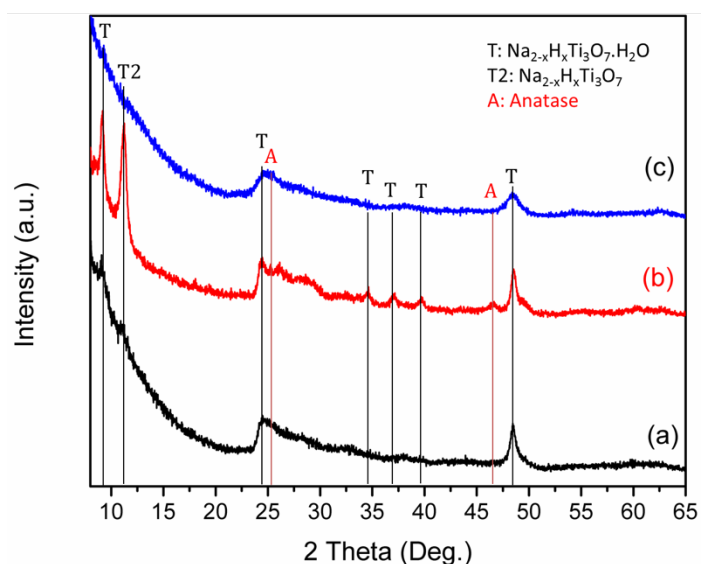


Figure 4.2 XRD patterns of samples (a) P36-2 (b) 36-2 (c) A36-2.

Sample 36-2 consists of both tubular and fiber structure of $\text{H}_2\text{Ti}_3\text{O}_7$ phase that is recognized at 2θ of 9 and 11° . Other peaks belong to $\text{M}_2\text{Ti}_3\text{O}_7$ ($\text{M}=\text{Na}$ or H). H_2O may bound to the structure and forms orthorhombic $\text{H}_2\text{Ti}_2\text{O}_5 \cdot \text{H}_2\text{O}$ phase that may be existent in samples 36-2 and P36-2 at 2θ of 25° . This peak is seen at 2θ of 25.07° in sample A36-2. The shift of the peak to higher diffraction angles is attributed to the narrowing of interlayer space by less H_2O content in the structure. In sample 36-2, $\text{H}_2\text{Ti}_3\text{O}_7 \cdot \text{H}_2\text{O}$ phase is assumed to exist due to the presence of

peaks at 2θ of 11° which also assigns fiber morphology. Better protonation was achieved in this sample. Anatase larger grains fail to transform titanate structure as opposed to P25 [95]. However, development of H titanate structure in sample 36-2 was better as compared to sample P36-2. Very small peaks at 25, 37.8, 48.7, and 53° suggest that anatase may be present in sample 36-2. Other samples were not investigated in detail in terms of their anatase or rutile content but it is clear that TiO_2 (B) or anatase phase is not existent in the samples since there is no peak at 2θ of 14.2° .

Figure 4.3 shows the XRD patterns of samples P6-2, P12-2, P36-2, P48-2, and P60-2 that were synthesized at different hydrothermal dwell time. Although as stated earlier the XRD results cannot unambiguously confirm the structure of the samples synthesized, this study was carried out to understand the variations in the phases developed by changing hydrothermal dwell time. Samples P6-2, P12-2, and P48-2 do not have the identifying layered titanate peak at $2\theta \cong 9.1^\circ$. However, sample P48-2 has (101) plane of 1D structure at 2θ of lower degrees instead of 9.1° as seen by broadening ($< 7^\circ$). This peak also perpendicular to the growth axis of [020] of 1D structure. Instead of (100) plane, formation of the 1D structures by (101) plane was reported [94]. Peak related titanate structure is obvious in the XRD pattern of samples P36-2 and P60-2. See Figure 4.3 (c) and (e). However, in the sample P60-2, (200) peak was shifted to 2θ of 11.08° as previously observed for sample 36-2 implying the narrowing of interlayer distance due to increasing crystallinity with transforming of morphology to cylindrical fiber. Intensity of the (200) peak in sample P36-2 is lower as compared to the one in sample P60-2. This make sense when the aspect ratio of fiber and tube is compared with each other. The peak shifted to higher angles possibly due to narrowing of interplanar distances by decrease in water content at longest duration. Other peaks at 24.3, 28.5, and 48° suggest that the structure may be orthorhombic $\text{H}_2\text{Ti}_2\text{O}_5 \cdot \text{H}_2\text{O}$ if all the Na is removed from the structure [94]. A 2θ of 48° may show that all the powders have preferential orientation through [020] axis. TiO_2 (B), anatase or rutile peaks are not detected at the samples.

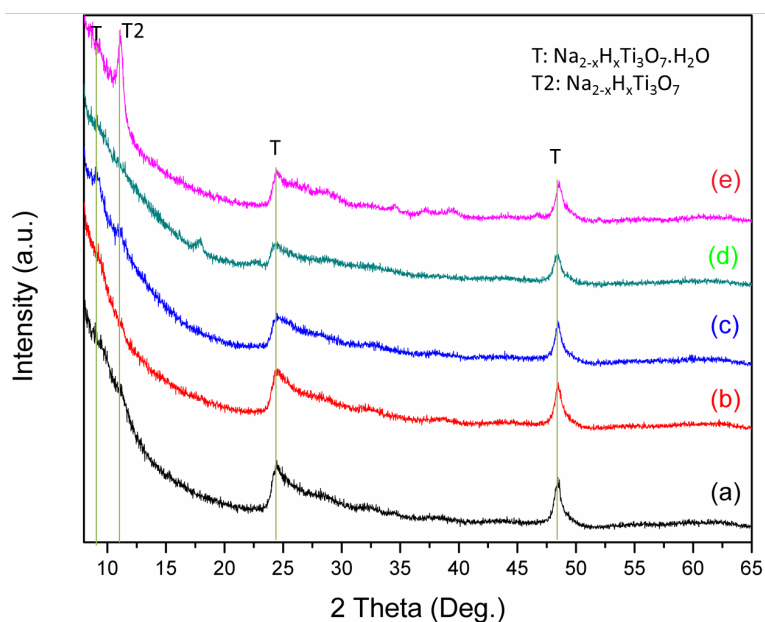


Figure 4.3 XRD patterns of samples (a) P6-2, (b) P12-2, (c) P36-2, (d) P48-2, and (e) P60-2.

The effects of acid washing on the development of phases in the nanostructures synthesized by using anatase as precursor were investigated also with respect to acid washing repeat. XRD patterns of powders with different acid washings are seen in Figure 4.4. As shown in Figure 4.1(a), without acidic washing nanostructure has many peaks belonging to Na and H titanates. Sharp typical titanate peak at 2θ of 9.1° is clearly seen in sample 36-0. Other peaks at 25.0 , 25.2 , 27.9 , 29 , 32.4 , 33.9 , 38.1 , 46 , 47.9 , 53 , 58 , and 62° suggest that the samples contain $\text{Na}_2\text{Ti}_3\text{O}_7$, $\text{Na}_2\text{Ti}_6\text{O}_{13}$, $\text{H}_x\text{Ti}_{2-x/4}\text{O}_4\cdot\text{H}_2\text{O}$, $\text{H}_2\text{Ti}_2\text{O}_4(\text{OH})_2$ and anatase phases. However, after washing with 0.1 M HCl, new phases were identified in the structure as shown in Figure 4.4 (b), (c) and (d). The peak at 2θ of 9.1° remained while a new peak at 2θ of 11.2° formed in sample 36-2 as seen in Figure 4.4 (b). These peaks belong to $\text{H}_2\text{Ti}_3\text{O}_7$ and $\text{H}_2\text{Ti}_4\text{O}_9\cdot\text{H}_2\text{O}$ phases, respectively. A peak at 2θ of 9.1° may also be attributed to remaining Na titanate and/or fiber morphology because after 4 times washing, it diminished as indicated in Figure 4.4 (c). A peak at 2θ of 48° is a common peak belonging to (020) plane of layered titanates, implying that the orientation exists in all of the samples as indicated before.

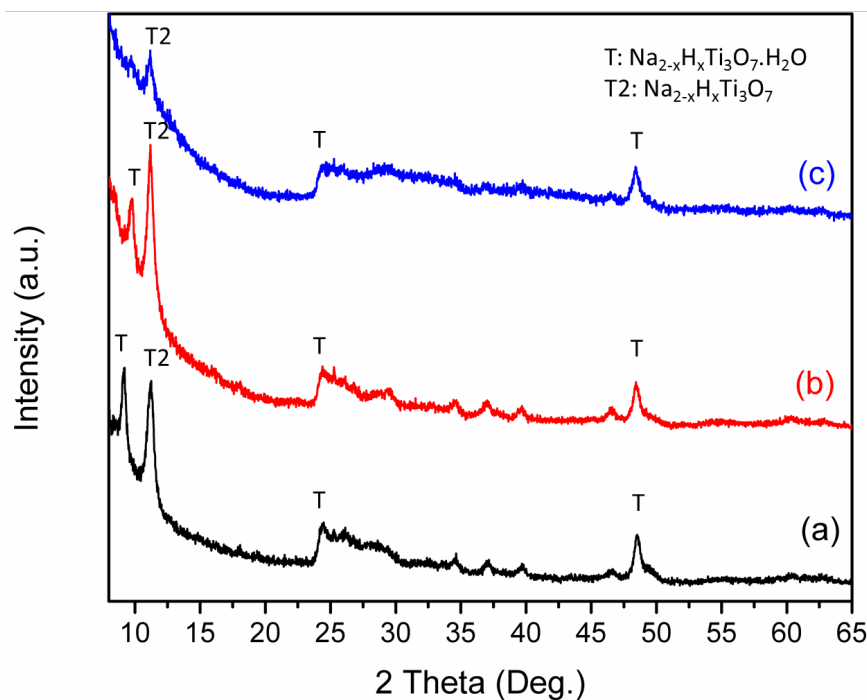


Figure 4.4 XRD patterns of samples (a) 36-2, (b) 36-3, (c) 36-4.

However, after washing with 0.1 M HCl, structure was changed considerably. The peak at 2θ of 9.1° remained and a new peak at 2θ of 11.2° appeared in the XRD pattern, suggesting the formation of $H_2Ti_3O_7$ phase in the structure.

XRD patterns of calcined nanostructures are shown in Figure 4.5. Phase development upon calcination of titanates was influenced by starting precursor materials used in hydrothermal synthesis. Calcination leads to formation of TiO_2 polymorph if Na is completely removed from the initial titanate phase. Obviously, after calcination at $450^\circ C$, typical titanate peak at 2θ of 9° disappeared. The findings suggest that Na titanate transforms first to H titanate via ion exchange, and then to TiO_2 during calcination at $450^\circ C$ for 1 h. The peaks at 2θ of 25.1 , 38 , 48 , 53.9 , 55.2 , and 62.8° are assigned to (101), (004), (200), (105), (211), and (204) of the anatase TiO_2 , respectively. Nevertheless, it is not for sure that the samples contain completely anatase phase because another unstable polymorph of TiO_2 (B) has similar peaks with some additional contributions to anatase, such as peaks at 2θ of 14.2 , 28.9 , 33.3 , and 44.1° (JCPDS 46-1238). Calcination at

temperatures below 500 °C results in formation of TiO₂ (B) phase [94]. Figure 4.5 (a) points out these contributions with a much less intensities in sample PC36-2 as compared to sample C36-2 that has a broadened (101) peak as seen in Figure 4.5 (b). In Figure 4.5 (c), sample AC36-2 does not have any TiO₂ (B) contribution phase due to anatase formation at 450 °C. Rutile phase was not detected in none of the powders. Shifting of peaks to higher angles due to contraction of interlayer distance as a result of the release of water molecules is the evidence of polymorphic transformation from titanate to TiO₂ structures.

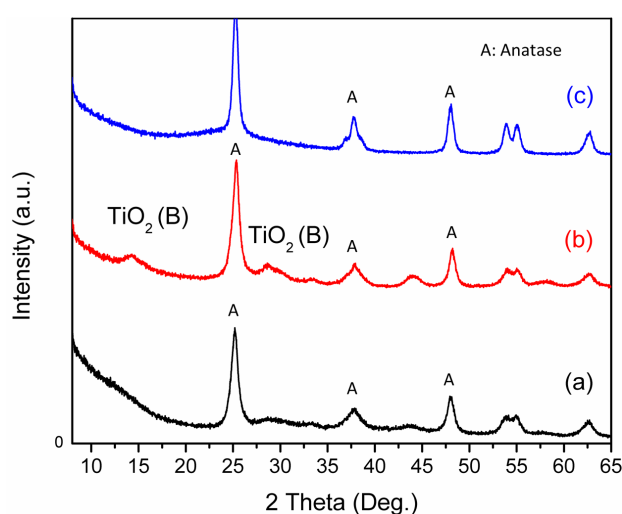


Figure 4.5 XRD patterns of samples calcined at 450 °C (a) PC36-2, (b) C36-2, and (c) AC36-2.

Figure 4.6 shows XRD patterns of sample P24 with different times protonation and calcination at 450 °C. Na₂Ti₃O₇ and/or Na₂Ti₆O₁₃ and other unidentified Na related titanate peaks were formed when the nanostructure was calcined in as synthesized form without protonation. The peak at 2θ of 9° shifted to 12.5° probably due to the contraction of interlayer distance because of release of water as seen in Figure 4.6 (a). Other peaks also shifted to higher angles by almost 2° except (020) peak at 48°. After one-time protonation, other peaks related to Na titanate were almost non existent except the peak at 2θ of 12.5 and 48° belongs to Na₂Ti₃O₇ and/or Na₂Ti₆O₁₃. A hump between 2θ of 25 and 35° probably means the transformation

to another polymorph as seen in Figure 4.6 (b). Calcination of protonation twice resulted in TiO_2 (B) and probably anatase formation in the structure as shown in Figure 4.6 (c). When the sample was acidic treated 3 times, the structure started to turn into anatase from TiO_2 (B) as seen in Figure 4.6 (d). EDS analysis was done to understand if there is Na inside the structure.

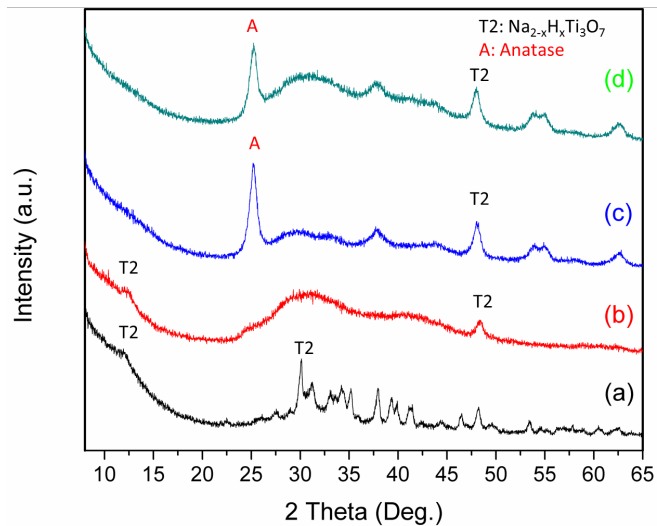


Figure 4.6 XRD patterns of calcined nanostructure after several protonation (a) PC24-0, (b) PC24-1, (c) PC24-2, and (d) PC24-3.

4.1.2 EDS analysis

EDS spectra of samples P36-0, P36-1 and P36-2 which are before and after exposing to acidic treatments several times are shown in Figure 4.7. Without acidic treatment, that is after hydrothermal synthesis, the sample contained large amount of Na (16 %) as indicated in Figure 4.7 (a). After one washing, sample was found to contain 10 % Na according to EDS analysis shown in Figure 4.7 (b). However after two times acidic washing, Na was not detected in the sample as depicted in Figure 4.7 (c).

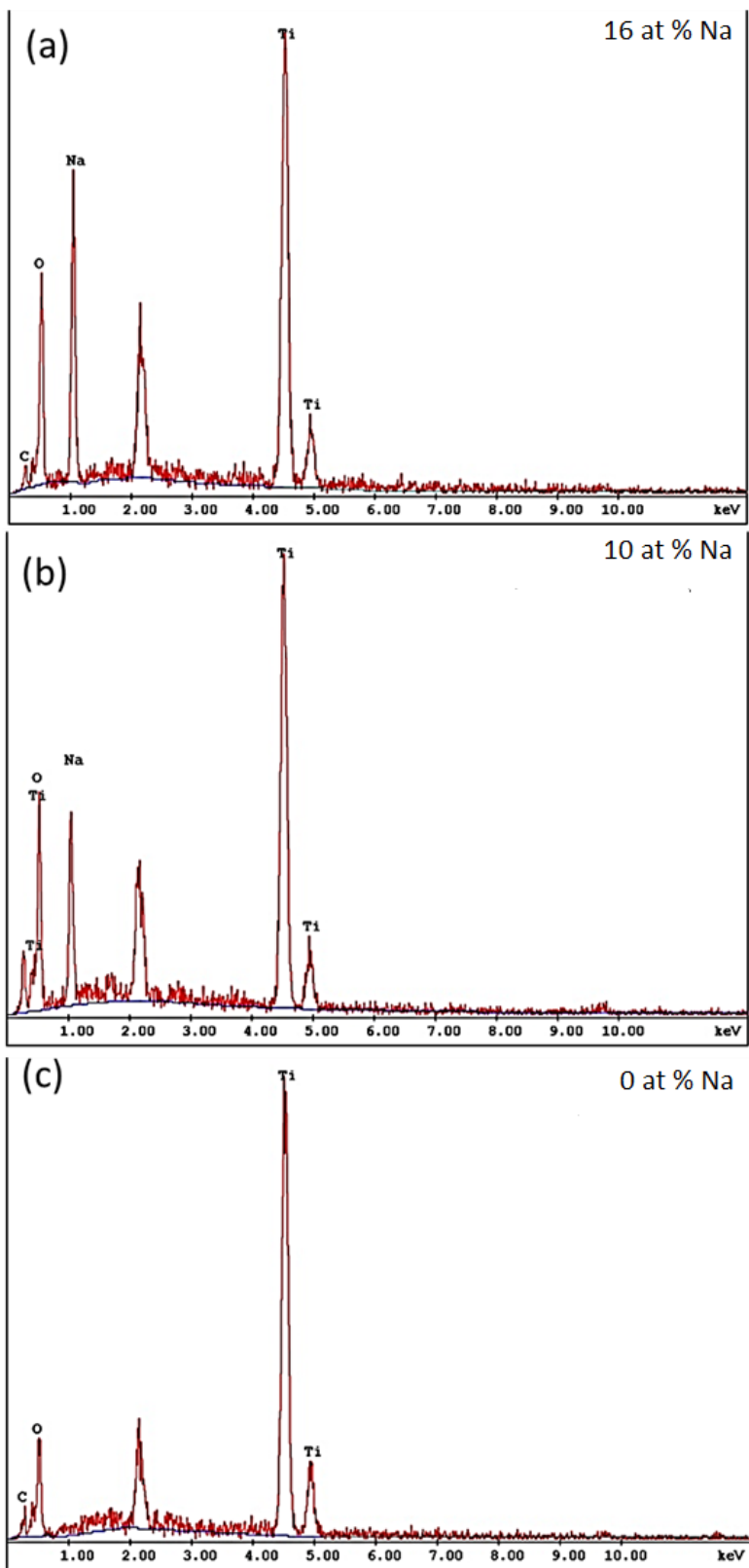


Figure 4.7 EDS spectra of samples (a) P36-0, (b) P36-1, (c) P36-2.

4.1.3 Morphological analysis

Figure 4.8 shows the representative FESEM images of samples P12-0, P12-2, 12-2, 24-2, A24-2, and A36-2. As seen in Figure 4.8 (a), titanate nanoribbons were formed by exfoliating of large aggregates as previously reported by many researchers [94, 113]. The exfoliating occurred in the form of nanoribbons. After neutralizing step and twice acidic washing, the structure still kept the ribbon form. The sheet like structure curved through the length axis as seen in Figure 4.8 (b).

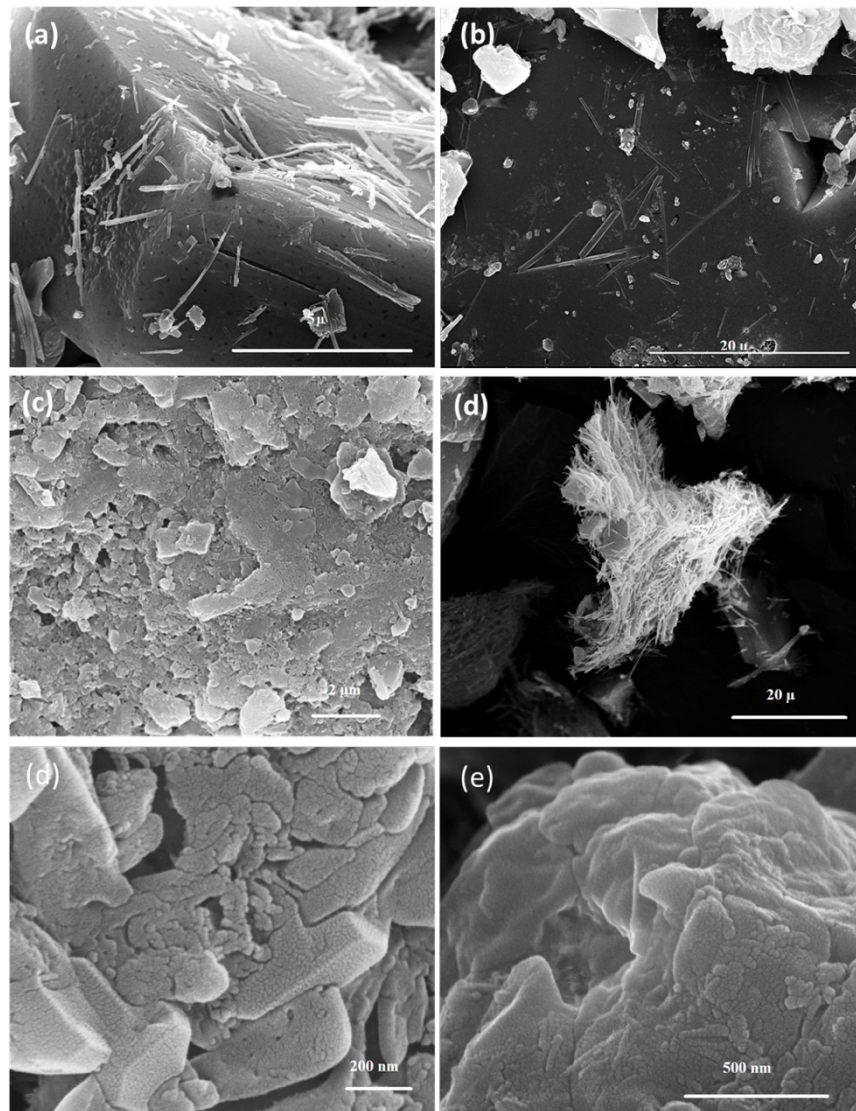


Figure 4.8 Representative FESEM images of samples (a) P12-0, (b) P12-2, (c) 12-2, (d) 24-2, (e) A24-2, (f) A36-2.

Figure 4.8 (c) shows the exfoliated structure of sample 12-2 from dissolved aggregates. Exfoliating of anatase structure is more homogenous compared to P25 is used at the same hydrothermal duration and, it appears in flake structure. The image was taken after acidic washing step. When the hydrothermal duration time was increased to 24 h, flakes were diverged in a particular axis and formed highly agglomerated needle like structures as shown in Figure 4.8 (d). The exfoliating mechanism is valid for two different precursors. However, as seen in Figure 4.8 (e) and (f), samples A24-2 and A36-2 were not in layered form.

Amorphous aggregates did not transform to layered form probably due to insufficient hydrothermal dwell time. Sample A36-2 was started to become layered in a form very similar to the one observed in sample 24-2. The modification in exfoliation mechanism of nanostructures synthesized by using different precursors has not been evaluated yet. Bavykin and Walsh [95] proposed a structure evolution with exfoliation mechanism very similar to the mechanism described for samples 24-2 and A36-2. Outcomes of the morphological analysis is in agreement with crystal structure analysis performed by using XRD. When the morphology is formed in layers, the XRD peak at 2θ of $9-11^\circ$ is observed. The rutile content and fine particle size of P25 powder lead to development of tetragonal aggregates that may cause the sheet-like exfoliates. The particle size of P25 is nearly 25 nm. It contains rutile and anatase phases together. The similarity of exfoliation in samples 24-2 and A36-2 is explained by anatase zigzag octahedral orientation. Although the amorphous precursor does not show any crystallographic plane, calcination at temperature of 450°C results in formation of anatase crystallites. Thus, the octahedral orientation of the grains may have a tendency towards the anatase formation. P25 powder also contains a large amount of anatase. However, rutile content of this powder may play a prominent role for development of tetragonal aggregates which exfoliates later to ribbons.

Figure 4.9 shows the aggregates synthesized by using different precursor materials. Figure 4.9 (a) shows the FESEM image of sample P6-2. As seen in the image, dissolved tetrahedrons in NaOH solution was aggregated in tetragonal shapes. By

increasing the hydrothermal duration further, these aggregates are exfoliated into nanoribbons as shown in Figure 4.8 (a). Zigzag structure of anatase is similar to but, rutile structure is different than structure of titanates. The reason for the nanostructure exfoliating in nanoribbons from tetragonal aggregates may be a result of rutile content in the structure. Utilization of titanate ribbons as nucleation seed facilitates anatase formation by splitting of titanate structure and attracting to itself Ti^{+4} ions and correlatively rutile formation becomes easier by surface transformation from anatase under acid assisted hydrothermal treatment conditions. Thus, anatase content may be more useful for nanoribbon exfoliating. Fine grain size of this powder probably establishes stronger attraction due to the higher surface energy. Thus, the layers exfoliate as diverged in the aggregate form. Generally, rutile is considered more stable in titanate processing [94]. Figure 4.9 (b) shows the FESEM image of sample 6-2 which was dissolved TiO_2 tetragonal-like aggregate using anatase beginning powder. The anatase precursor has larger particles (200 nm) as compared to P25 powder. This structure exfoliated forming layers for whole structure. The layer formation is probably due to the anatase zigzag structure. Larger particles of the anatase powder may establish weaker bonds with lower surface energy and thus they exfoliate as layers. Amorphous powder aggregate of sample A6-2 has a sponge like morphology as seen in Figure 4.9 (c). This morphology is different from the products of other precursors.

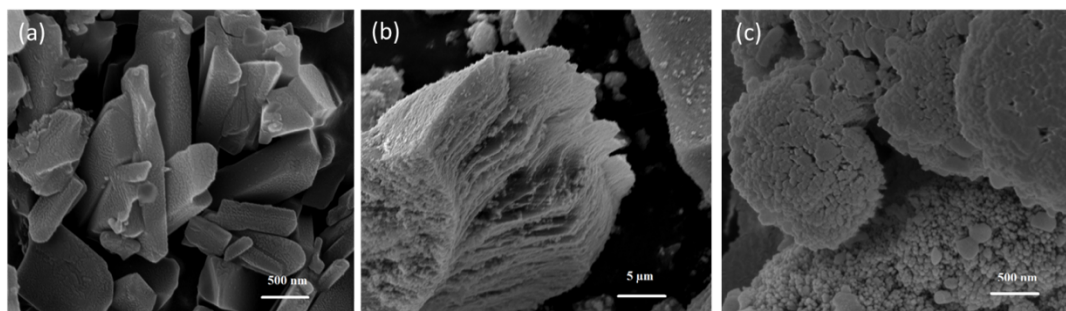


Figure 4.9 FESEM images showing the dissolved aggregates synthesized using different precursors for samples (a) P6-2, (b) 6-2, (c) A6-2.

FESEM images of P12-2, P24-2, P36-2, and CP36-2 are seen in Figure 4.10. After 12 h of hydrothermal dwell time, ribbons and diverged ribbons in fiber were noticed in the structure as shown in Figure 4.10 (a). Hydrothermal dwell time of 24 h resulted in rolled sheets which form tubular structure and closed edge fibers as shown in Figure 4.10 (b). After 36 h, fibers and ribbons appeared in the sample as illustrated in Figure 4.10 (c). The length of these one dimensional structures is several micrometers. Straight and/or twisted form of these structures were introduced to literature [94]. The one dimensional structures obtained by using P25 as precursor resulted in structures in straight form. Figure 4.10 (d) shows the image of sample P36-2 that was calcined after twice acidic treatments. The straight form of the structure is obvious in the image although the fibers are highly agglomerated. Nanotube morphology was not detected. As XRD pattern of sample CP36-2 suggested a polycrystalline structure of small crystallites on the fiber morphology is recognized evidently.

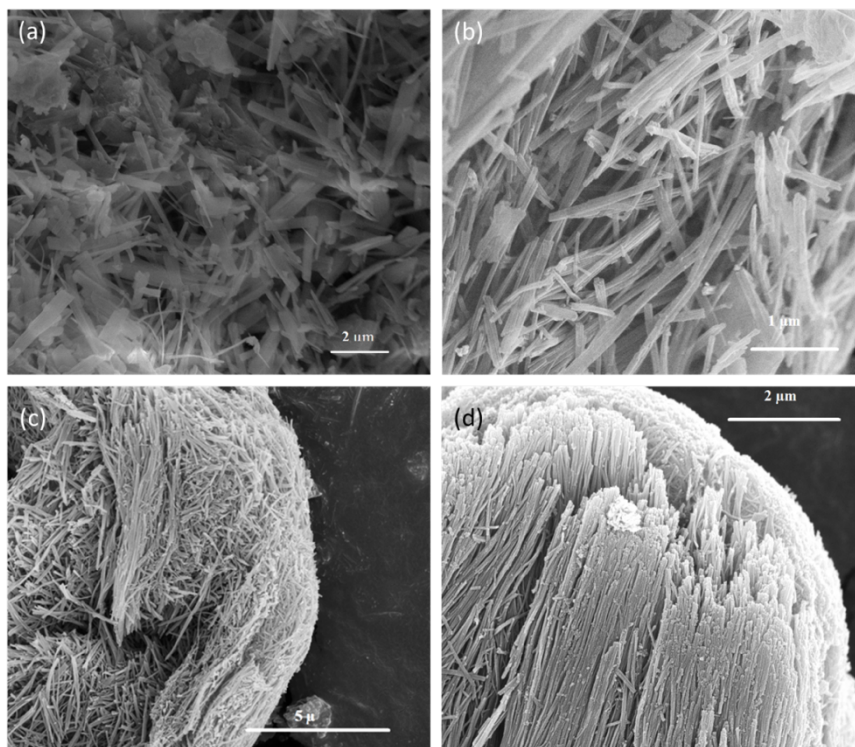


Figure 4.10 FESEM images of nanostructures synthesized using P25 powder as precursor (a) P12-2, (b) P24-2, (c) P36-2, (d) CP36-2.

Figure 4.11 shows the FESEM images of samples 12-2, 24-2, 36-2, and C36-2. As seen in Figure 4.11 (a), 1D structure formed by ripping of sheets from the edges after 12 h hydrothermal dwell time. After 24 h, a tubular structure having a length of smaller than 500 nm was detected. The tubular structures did not reside independent from the mother layer that probably resulted from the larger diverged sheets as indicated Figure 4.11 (b). After 36 h, 1D nanostructures with placing three in one appeared in the morphology. Structural alignment was not regular and was raptured as indicated in Figure 4.11 (c). After calcination, thin ribbon-like structure with a length of several micrometers could be seen in sample C36-2. The structure is different than the one observed in sample CP36-2. There is no alignment. Probably, after longer synthesis this structure would be in the form of narrower ribbons that are more close to fiber morphology. Any rolled structure was not detected in the samples other than sample 24-2. When the two precursors are taken into consideration, the resultant structures are more or less similar.

FESEM images of nanostructures synthesized using amorphous precursor are shown in Figure 4.12. The images indicated the amorphous powder evolution in hydrothermal reactor after protonation at different durations. As seen in Figure 4.12 (a), a 12 h of hydrothermal time did not result in an efficient amount of layered structure formation. Small spherical layered structures with approximately 100 nm diameter formed. After 24 h, fiber like structures were witnessed with layered structure as indicated in Figure 4.12 (b). This fiber like structure formed by gathering of small spherical units. Oriented attachment (OA) or Oswald ripening (OR) mechanisms were already proposed for 1D structures [121]. This is completely different from the roll-up model because the oriented crystal growth (OCG) mechanism indicates that titanate nanotubes are formed by oriental adding TiO_6 building blocks onto seeding nanoloops [210]. In the present case, nano particles smaller than 20 nm was oriented to form 1D structure while sheet like structure formation. The formation ensued without dissolution. However, dissolved aggregate formation was also observed as seen in the same image. Sheet formation was noted after 36 h of synthesis as seen in Figure 4.12 (c).

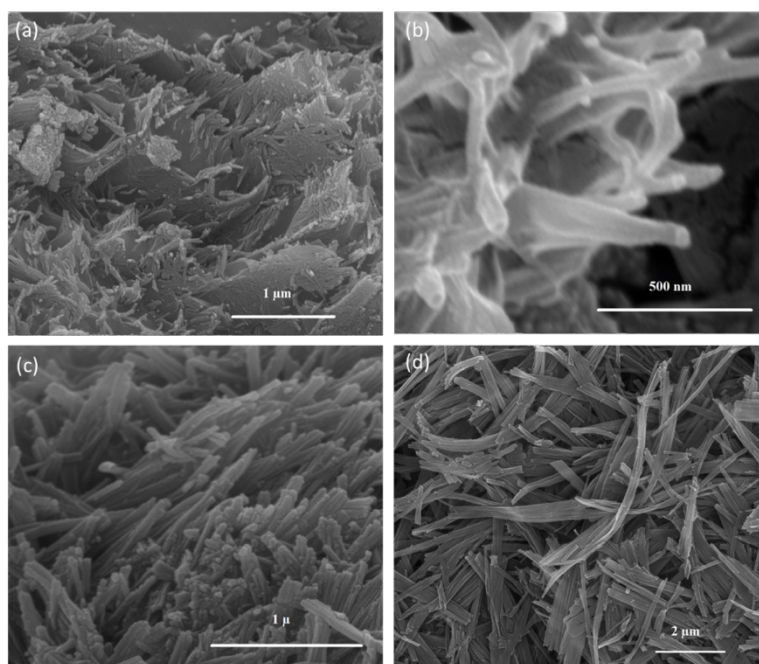


Figure 4.11 FESEM images of powders synthesized using anatase precursor (a) 12-2, (b) 24-2, (c) 36-2, (d) C36-2.

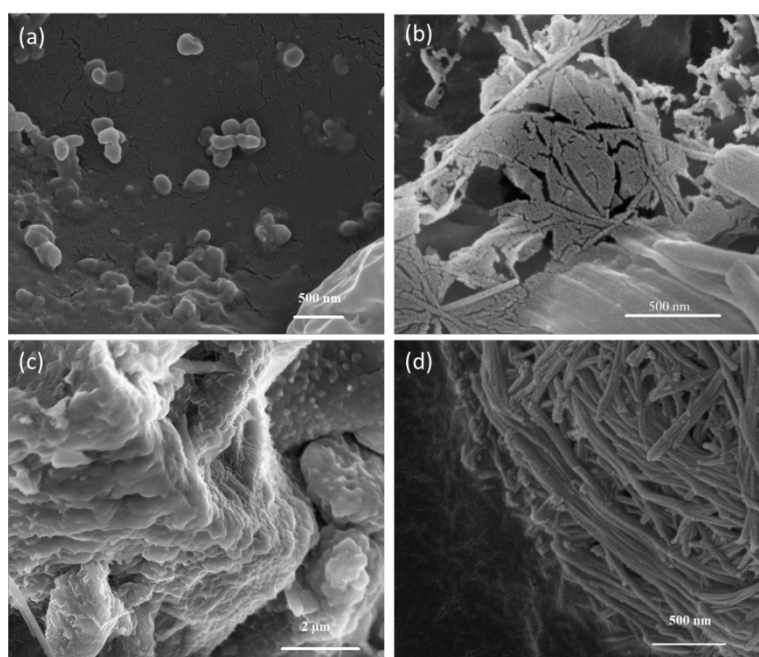


Figure 4.12 FESEM images of powders synthesized using amorphous precursor (a) A12-2, (b) A24-2, (c) A36-2, (d) AC48-2.

Ripening of nano particles was not detected in this sample probably due to dissolution of all powder. Wire-like morphology with nearly 50 nm in diameter and several micrometers in length was observed after 60 h of synthesis as seen in Figure 4.12 (d). Structure was highly agglomerated and bended in contrast to straight structure synthesized by using crystalline powder at the beginning.

Figure 4.13 shows the HRTEM images and SAED pattern of sample P36-0. As seen in Figure 4.13 (a), a tubular morphology formed after hydrothermal synthesis without further treatment. The inner diameter of tubular structure was 25 nm and the outer diameter was 34.3 nm. The interlayer distance was measured 0.84 nm, which belongs to $\text{Na}_2\text{Ti}_3\text{O}_7$ structure as indicated in Figure 4.13 (b). The planes are parallel to growth direction of tubes which makes the growth direction as [010] axis. Indeed as seen in Figure 4.13 (c) the interlayer distance between perpendicular planes was 1.89 nm, which belongs to (020) plane of Na titanate phase. This structure is not a tubular structure. It is probably an exfoliated sheet without bending. Figure 4.13 (d) shows the SAED analysis of sample P36-0. As seen in the pattern, the dots have streak-like reflections around which is probably due to presence of stack fault and/or small texturation. Also researchers reported reflections of diffraction data of these samples calling the structure as “super-structure” [211].

Figure 4.14 shows the HRTEM and SAED patterns of sample P36-2. As seen in Figure 4.14 (a) the sample consists of tubular structure with nanosheets. Fiber morphology was not realized by this analysis. Diameter of the tubes decreased as compared with the sample that was not acid treated possibly because of the diverging of sheets with a width of 50 nm to narrower structures like 6 to 15 nm as seen in Figure 4.14 (a). The interlayer space of the structure was measured 1.78 nm, which clarifies the narrowing of d spacing of plane (020) as shown in Figure 4.14 (b). Interlayer spacing between (200) planes are 0.79 nm, which indicates shrinkage as compared with the sample obtained without acidic treatment as seen in Figure 4.14 (c). Figure 4.14 (d) shows SAED analysis. The reflected spot image

is very similar with the one detected in sample P36-0. Dots number increased as compared to sample P36-0 which may be related to the degree of crystallinity.

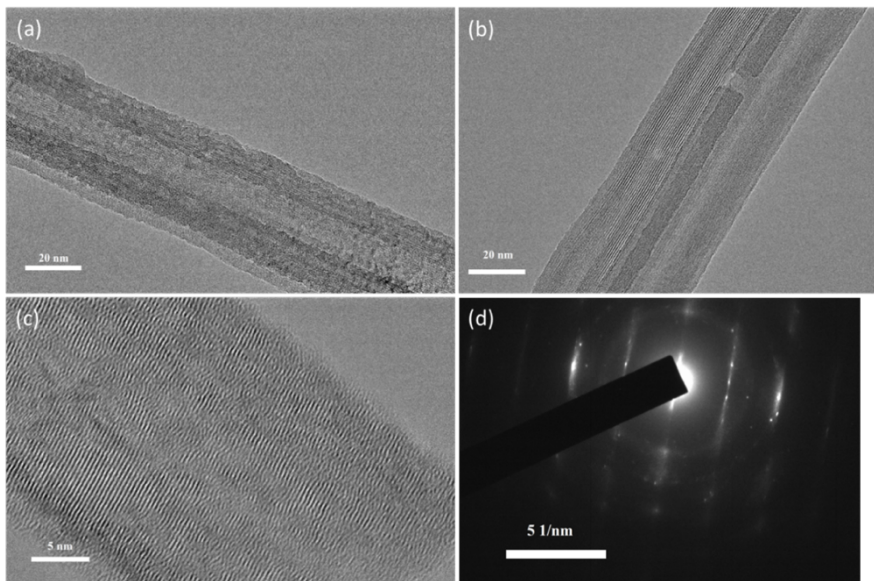


Figure 4.13 HRTEM images of sample P36-0 (a) tube image, (b) lattice fringes of tubular structure, (c) Lattice fringes of sheet structure (d) SAED pattern taken from tubes and sheets.

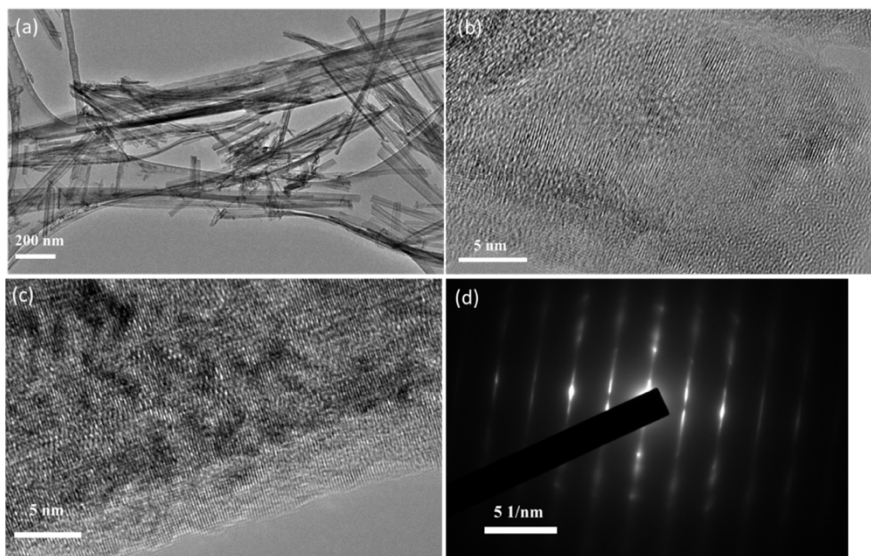


Figure 4.14 HRTEM images of sample P36-2 (a) General image of sample P36-2, (b) lattice fringes parallel to growth direction, (c) lattice fringes perpendicular to growth direction, (e) SAED analysis.

Figure 4.15 shows the HRTEM images of sample CP36-2. Bright field image shown in Figure 4.15 (a) indicates the 2D structure several micrometers in length and 14 nm in diameter. Distance between two fringes was measured as 3.52 nm, which corresponds to d spacing of anatase 101 planes. Fringes are not seen very clearly. However, discernable ones keep their continuity along the sample. The structure is not hollow implying its fiber structure instead of tube. Analysis of some of the structures was very difficult due to a high amount of so thin sheet like structure formation. Figure 4.15 (b) shows the image of the same sample in a large area. Small (<100 nm) oriented structures accompany with long sheets, which are in fiber morphology. However, these fiber-like small structures are polycrystalline, may be a result of Oswald ripening, as seen in Figure 4.15 (c). The interlayer spacing for these small structures was measured 3.51 nm. The fringes are clearer implying better crystallinity in the samples. SAED analysis revealed polycrystalline behavior as seen clearly in Figure 4.15 (d).

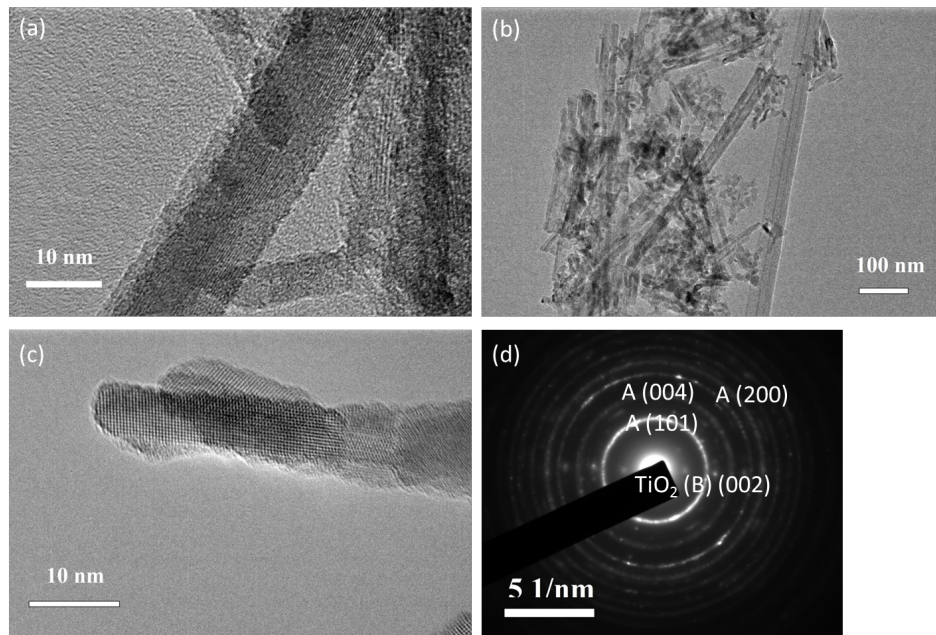


Figure 4.15 Ribbon structure of sample PC36-2 (a) Fringes of unit structure, (b) agglomerated ribbons in different diameter and length, (c) stacked ribbons with fringes, (d) SAED pattern of sample.

Planes obtained by SAED analysis are presented in in Table 4.1. Data confirm the results reported previously by XRD analysis. TiO_2 (B) structure that could not be identified by XRD analysis was detected by SAED analysis clearly in two dots. This may be attributed to low calcination temperature. Interlayer spacing TiO_2 (B) 110 plane is similar with anatase 101 plane ($d=0.35$ nm). The EDS spectra shown in Figure 4.16 revealed Ti and O peaks but no Na peak in sample PC36-2.

Table 4.1 SAED analysis data for sample PC36-2.

Reciprocal of Diameter (1/nm)	Interplanar spacing (Å)		Corresponding Crystallographic Plane (Phase)
	Calculated	Theoretical*	
3.213	6.39	7.86	100 (TiO_2 (B))
5.67	3.53	3.52	101 (anatase)
8.42	2.37	2.38	004 (anatase)
10.66	1.87	1.88	200 (anatase)
11.62	1.72	1.70	105 (anatase)

*Anatase: JCPDS 21-1272, TiO_2 (B): JCPDS 46-1238.

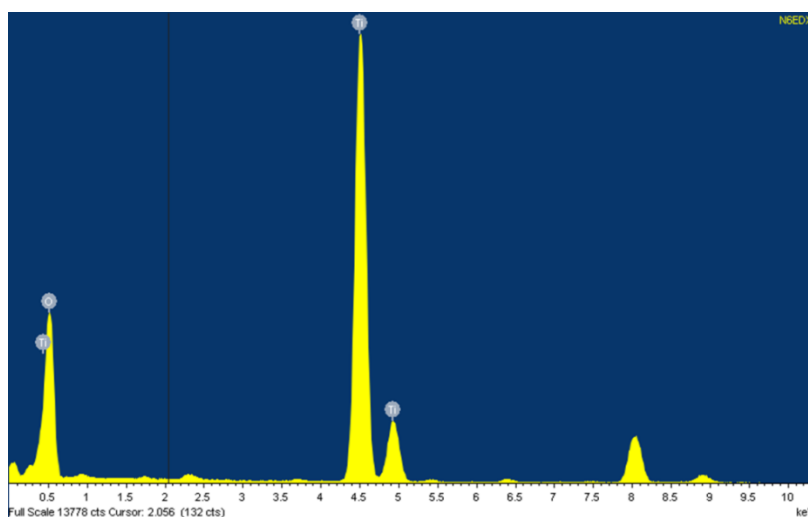


Figure 4.16 Representative high resolution EDS spectra of sample PC36-2.

4.1.4 Thermal analysis

The DTG, DTA and TG analysis of samples P36-2, 36-2 and A36-2 are shown in Figure 4.17. Thermogravimetric analysis revealed that large amount (~ 20 %) of weight loss occurred in all of the samples. Since only water is present in the samples as a volatile matter, weight loss is assumed to be due to volatilization of water. Weight stabilization was achieved for samples P36-2 and A36-2 at 400 °C but not for sample 36-2 until 1000 °C. This finding implies better stability of samples P36-2 and A36-2 as compared to sample 36-2. DTA curves showed one peak for powder P36-2 and two peaks for 36-2 in the endothermic region at temperatures between 25 and 400 °C as seen in Figure 4.17 (a) and (b), respectively. The endothermic peaks are attributed to the removal of physically adsorbed water and/or interlayered OH groups for samples P36-2 and 36-2. DTA curve of sample A36-2 indicates one broad peak between 25 and 200 °C as shown in Figure 4.17 (c). Sample A36-2 would probably favor larger amount of adsorbed water although all the samples were preserved in the same conditions. The broadening means that dehydration process occurs slowly in sample A36-2. A large exothermic peak above 200 °C in samples P36-2, 36-2 and a small peak in sample A36-2 is attributed to TiO₂ (B) transformation from H-titanate structure as shown in Figure 4.17 (a), (b) and (c). Above 400 °C, larger peaks for samples P36-2, 36-2 and A36-2 are noticed. This peak may be considered to transform to anatase for samples P36-2 and A36-2 and TiO₂ (B) for sample 36-2. XRD and SAED analysis of calcined sample PC36-2 also suggests a large amount of anatase and small amount of TiO₂ (B) transformations at 450 °C. However, XRD analysis suggests TiO₂ (B) transformation for sample 36-2. In the XRD pattern, no peak of TiO₂ (B) was detected for sample AC36-2. Thus, the exothermic peak above 400 °C is probably anatase transformation for sample A36-2.

Below 700 °C, there is an exothermic peak in sample P36-2 which may be transformation of TiO₂ (B) to anatase or rutile. Above 700 °C, there is another small exothermic peak for sample for sample A36-2 attributed to transformation to rutile from amorphous phase remained in the structure. No peak was detected at

this temperature range for samples P36-2 and 36-2. Above 800 °C there is last exothermic peak for P36-2 and A36-2 which may be rutile transformation. The rutile transformation peak was detected above 900 °C for sample 36-2. The broadening of this peak for sample 36-2 means that the transformation is slow. It is predicted that sample 36-2 is stable as compared to other samples due to the slow transformations, the mass reduction continues until 1000 °C which leads phase transformation continuity of the sample. The slow transformation may be due to the anatase phase remained in the structure.

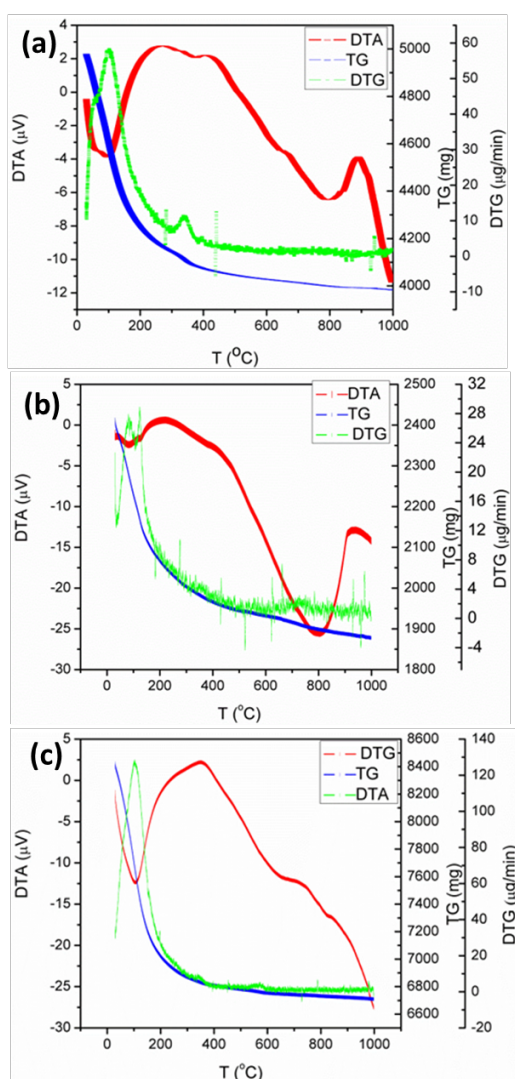


Figure 4.17 DTA (μV), TG (μg) and DTG ($\mu\text{g}/\text{min}$) curves of sample (a) P36-2, (b) 36-2, and (c) A36-2.

4.1.5 Photocatalytic activity

Figure 4.18 shows the absorbance curves of samples synthesized for 36 h. As seen from Figure 4.18 (a) and (b) as synthesized and protonated samples P36-0 and P36-2 perform a very high adsorption of methylene blue molecules. Degradation of MB is attributed to high adsorption capability of titanate powders. The high adsorption might be a result of high surface area as well as high ion exchange ability of the powder. MB degradation of sample PC36-2 is illustrated in Figure 4.18 (c). The graph demonstrates a gradual MB degradation which shows lower desorption probably due to phase transformation from titanate to TiO_2 after calcination. Figure 4.18 (d) shows the MB degradation of sample 36-0 which does not demonstrate as high adsorption as sample P36-0. MB degradation is slow but follows a linear trend. Sample 36-2 showed more adsorption as compared to sample 36-0 as shown in Figure 4.18 (e). However, degradation occurred for this sample was much slower than the one observed in sample 36-0 and follows a linear trend that is an indication of the first order kinetics. Sample C36-2 showed the highest adsorption among the samples synthesized by using anatase precursor as illustrated in Figure 4.18 (f). For the powders synthesized by using anatase precursor, the residual anatase phase in the structure might be responsible for the gradual degradation of MB with a first order kinetic. In addition, layered form of sample 36-0 is quite different than that of sample P36-0. Crystallographic and morphological differences between the two structures might be responsible for the occurrence of different reactions during degradation test. Figure 4.18 (g) shows the absorption of sample A36-0 that shows highest adsorption (98 %) as compared to previous samples. Sample A36-2 exhibited slightly low adsorption as seen in Figure 4.18 (h).

Sample AC36-2 showed a high adsorption as compared to other calcined samples. The sample showed the highest photocatalytic rate among all the samples. The higher reactivity may be a result of morphological difference of this nanostructure as having large sheets without rolled or diverged. Indeed, the adsorbed powders also retards the photocatalytic reaction that even the solution was mixing during

illumination, photon-material interaction is limited. For that reason, degradation occurs slowly with those samples. Thus, adsorption may affect reversely to the photoactivity of the powders.

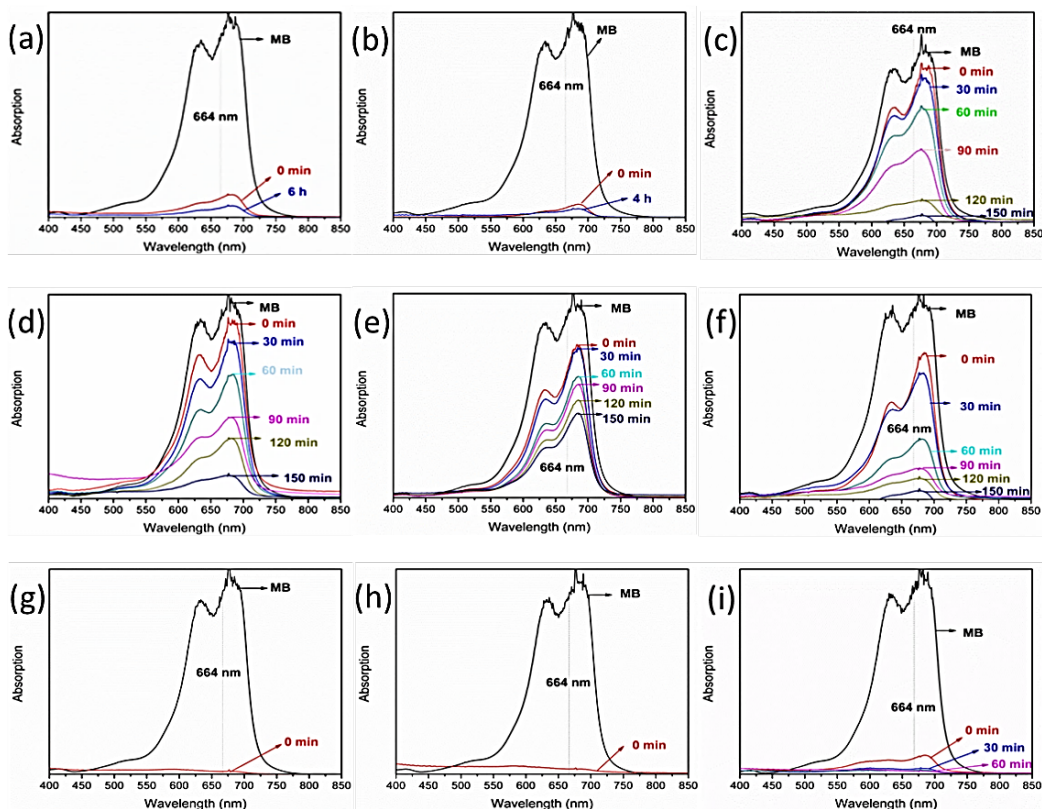


Figure 4.18 Absorbance spectra of solutions containing MB and (a) P36-0, (b) P36-2, (c) PC36-2, (d) P36-0, (e) 36-2, (f) C36-2, (g) A36-0, (h) A36-2, and (i)AC36-2.

Comparison of degradation rate of MB by calcined samples was shown in Figure 4.19. Titanate powders were not compared in terms of degradation due to the high adsorption ability of these structures that show a deceiving degradation. Sample AC36-2 also performed considerably high adsorption to MB molecules. However, a real degradation occurred in the sample. The BET results of powders P36-2, 36-2 and A36-2 are tabulated in Table 4.2. The high surface area explains the photoactivity and adsorption tests of powders. Figure 4.20 shows the band gap

measurements using Kubelka Munk transformation of absorption data of nanostructures.

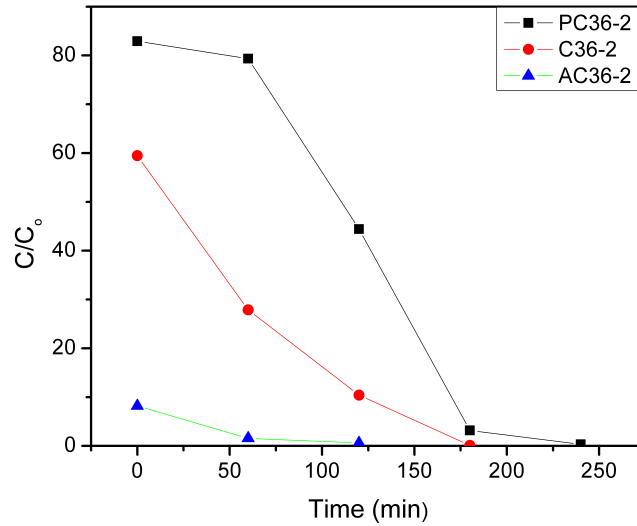


Figure 4.19 Variation in concentration of methylene blue with respect to time.

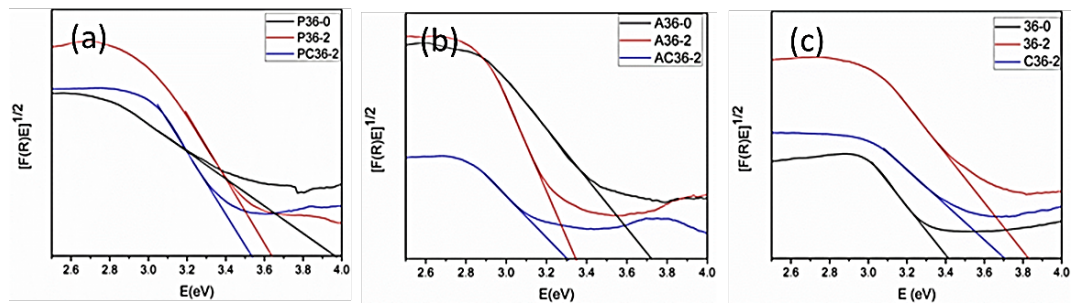


Figure 4.20 Band gaps as calculated by Kubelka Munk transformation of absorption data of the samples synthesized using (a) P25, (b) anatase, and (c) amorphous precursor.

Band gaps obtained by transaction of curves were tabulated in Table 4.2. As shown clearly in Table 4.2, band gap of Na-titanates is higher than that of TiO₂ polymorphs with an exception of sample 36-0. The anatase existence probability may cause the lower band gap energy of this powder. For the powders synthesized using P25 and amorphous powder, band gap values were decreased after acidic

washing and further decrease occurred after calcination. Band gap of sample synthesized by anatase precursor increased by acid washing which is possibly due to phase transformation from $\text{Na}_2\text{Ti}_3\text{O}_7$ and $\text{Na}_2\text{Ti}_6\text{O}_{13}$ to orthorhombic $\text{H}_2\text{Ti}_{2-x/4}\square_{x/4}\text{O}_4\cdot\text{H}_2\text{O}$ and monoclinic $\text{H}_2\text{Ti}_3\text{O}_7$ while other samples was transformed to mostly $\text{H}_2\text{Ti}_{2-x/4}\square_{x/4}\text{O}_4\cdot\text{H}_2\text{O}$ phase. Or anatase content may decrease by acidic washing due to dissolution thus band gap increases. After calcination, band gap of the samples were decreased. However, the lowest band gap which is closer to TiO_2 anatase (3.2 eV) was obtained by sample AC36-2. Photocatalytic activity also higher compared to other samples for sample AC36-2. The XRD pattern of this sample was also closer to anatase structure when compared to other calcined samples.

Table 4.2 Band gaps of samples calculated by Kubelka Munk transformation of absorption data.

Sample	P36-0	P36-2	PC36-2	36-0	36-2	C36-2	A36-0	A36-2	CA36-2
Band Gap (eV)	3.96	3.64	3.53	3.41	3.83	3.51	3.72	3.35	3.31
Surface Area (m^2/g)	-	283	-	-	188	-	-	232	-

CHAPTER 5

RESULTS AND DISCUSSION: HYDROTHERMAL SYNTHESSES OF TiO₂ NANOSTRUCTURES USING ACID CATALYZER

5.1 General

This study was conducted to synthesize TiO₂ nanostructures by using HNO₃ assisted hydrothermal treatment and, to evaluate the optical properties of the structures synthesized. HNO₃ was chosen as a catalyzer due to lack of information about application of this catalyzer especially in strong molarity in the open literature. Time, temperature, and acid molarity of hydrothermal treatment were changed gradually in order to understand the formation mechanisms of the TiO₂ with polymorphs having different crystal structure and morphology. Anatase, anatase-rutile mixture, brookite, brookite-anatase mixture, and rutile TiO₂ with 0D - 3D crystal structure was synthesized. No alcohol, oxidation agent, or surfactant were used during hydrothermal treatments but H-titanate structure was used as nucleation seed to obtain phase pure rutile TiO₂. After synthesis, structural, morphological and optical characterizations were done. Results were compared with the results reported by other researchers who used other acid catalyzers for growth conditions. A formation mechanism was proposed for 3D structures. Photoactivity of selected powders were determined to investigate the suitability of these powders for DSSC applications.

5.1.1 XRD analysis

XRD patterns of powders synthesized by HNO₃ assisted hydrothermal treatment using different acid molarity, temperature, and durations are illustrated in Figure 5.1. All XRD analyses were done at diffraction angles between 2 θ of 20 and 80°.

Calculations were done by eliminating $\text{CuK}\alpha\text{-2}$ irradiation. The peak locations and their relative intensities for the TiO_2 phases were cited from the Joint Committee on Powder Diffraction Standards (JCPDS) database. The diffraction peaks located at 25.4 , 37.6 , 48 , 54 , 55 , and 63° corresponding to the characteristic (101), (004), (200), (105), (211), and (204) planes of the anatase phase, respectively (JCPDS 21-1272); and at 27.3 , 36 , 41.3 , 54.4 , 56.2 , and 62.8° corresponding to the characteristic (110), (101), (111), (211), (220), and (002) planes of the rutile phase, respectively (JCPDS 21-1276) were detected in the powders. The existence of brookite (JCPDS: 29-1360) in the resultant powders is readily discernible from its (121) diffraction peak located at 30.8° in the XRD pattern, where no overlapping of this peak with anatase or rutile peaks occurs.

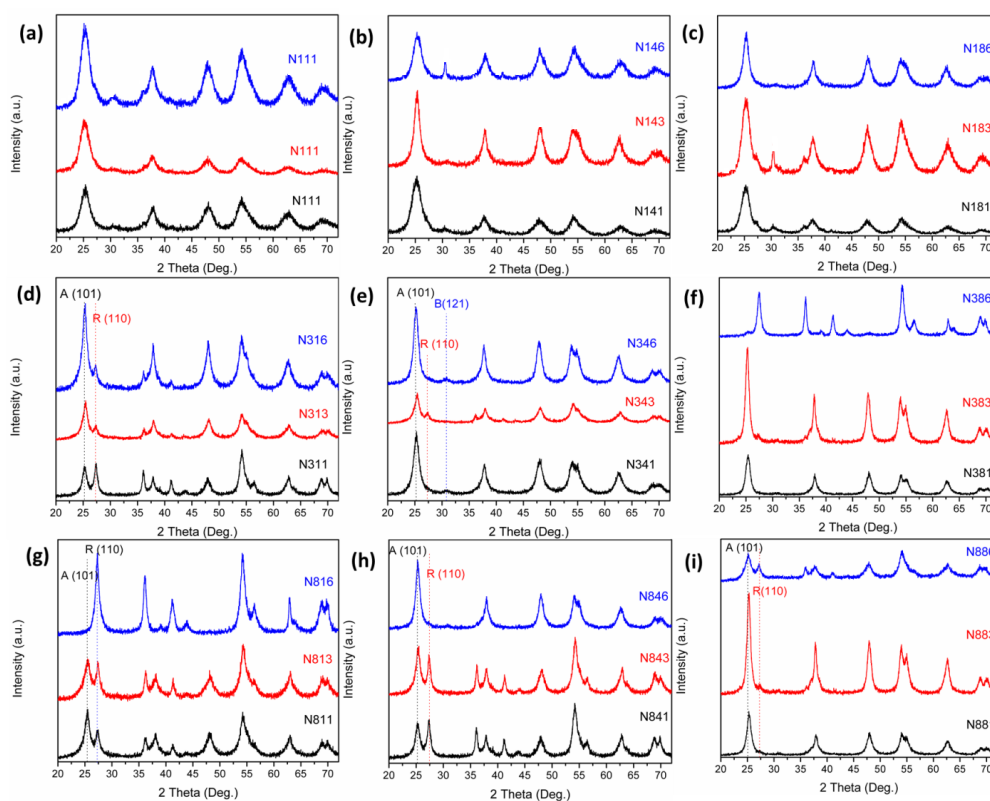


Figure 5.1 XRD patterns of samples synthesized using 1 M acid catalyzer at (a) 110°C , (b) 140°C , (c) 180°C , for different durations, 3 M acid catalyzer at (d) 110°C , (e) 140°C , (f) 180°C for different durations, and 8 M acid catalyzer at (g) 110°C , (h) 140°C , (i) 180°C for different durations.

Anatase phase evolved dominantly for all synthesis durations when 1 M acid catalyzer was used at 110 °C. See Figure 5.1 (a). The existence of anatase phase is easily noted by the peaks at 2θ of 37.6 and 62° which do not overlap with brookite peaks. Brookite phase accompanied to anatase as clearly seen in the peak at 2θ of 30.8°. As duration increased to 6 h, brookite share increased and rutile hump appeared at 2θ of 27.4°. Figure 5.1 (b) shows the XRD patterns of powders synthesized using 1 M acid catalyzer at 140 °C. 1 h duration resulted in anatase formation with a small amount of brookite. Increasing hydrothermal dwell time to 3 h led an increase in anatase phase and extent of crystallinity. FWHM of the (110) peak decreased as a result of increasing crystallinity. After 6 h synthesis, brookite phase evolved in the structure. FWHM increased again due to the dissolution of anatase crystals in the acidic solution. Figure 5.1 (c) shows the XRD patterns of powders synthesized using 1 M acid catalyzer at 180 °C. Anatase, brookite and a trace amount of rutile were detected in the structure after 1 h of synthesis. Upon increasing synthesis duration to 3 h, brookite share increased. Finally, after 6 h of synthesis, the brookite phase diminished again and anatase phase remained as the only phase in the structure. Anatase and rutile phases formed after 1 h of synthesis at 110 °C using 1 M acid catalyzer. See Figure 5.1 (d) The calculations revealed that amount of rutile was more than anatase as indicated in Table 5.1. The intensity of (211) plane peak of rutile is bigger than that of (110) plane peak of rutile. Increasing synthesis duration causes much more anatase formation in the structure. However, the peak of (211) plane of rutile is still bigger than (110) plane of rutile. By increasing the duration to 6 h, anatase content increased as compared to rutile. Since the amount of the powder used for XRD analysis is always the same, the decrease of intensity of rutile peaks may be due to the dissolution of this phase by longer synthesis durations. XRD patterns of the powders synthesized at 140 °C using 3 M acid catalyzer are shown in Figure 5.1 (e). After 1 h synthesis, anatase and brookite phases formed in the structure. The share of the phases is given in Table 5.1. Brookite phase transformed to rutile as synthesis duration was

Table 5.1 Phase share and crystallite size of selected powders.

Sample Codes	Amount of Phases (wt %)			Average crystallite size (nm)		
	Anatase	Rutile	Brookite	Anatase	Rutile	Brookite
N800	NC*	-	-	NC	-	-
N111	89	8	3	6.23	NC	NC
N113	88	9	3	6.45	NC	NC
N116	86	8	6	7.34	NC	NC
N141	89	7	5	5.78	NC	NC
N143	>99	-	-	6.61	-	-
N146	64	5	31	4.54	NC	NC
N181	85	8	7	4.65	NC	NC
N183	63	5	32	5.48	NC	NC
N186	>99	-	-	7.02	NC	NC
N311	45	55	-	6.71	7.35	-
N313	80	20	-	6.83	7.15	-
N316	77	23	-	8.17	9.03	-
N341	93	4	3	6.78	NC	NC
N343	73	27	-	7.03	7.10	-
N346	87	-	13	7.54	-	NC
N381	>99	-	-	8.65	-	-
N383	>99	-	-	9.07	-	-
N386	7	93	-	NC	9.27	-
N811	56	44	-	4.09	7.03	-
N813	44	56	-	4.12	7.89	-
N816	-	>99	-	-	8.57	-
N841	50	50	-	7.07	8.33	-
N843	55	45	-	7.32	9.81	-
N846	>99	-	-	8.25	-	-
N881	91	7	6	8.45	NC	NC
N883	76	24	-	9.50	10.46	-
N886	59	41	-	6.23	8.32	-
HN843	-	>99	-	-	10.17	-

NC: Not calculated due to minor amount of crystallinity, and/or overlapping of peaks

increased to 3 h. The intensity of (101) plane peak of anatase decreased probably due to etching effect of anatase. After 6 h synthesis, the rutile phase diminished and the structure consisted of anatase and brookite again with a better crystallinity. Sample N343 has an orientation growth inside which is seen from the large (211) plane of rutile. The sample synthesized using 3 M acid catalyzer showed the strength of anatase phase for dissolution as compared to

rutile phase. Brookite phase also existed when 3 M acid catalyzer was used at 140 °C. When the temperature increased to 180 °C, structure consists of first anatase and brookite, then anatase and rutile and rutile and anatase after 6 h.

As the acid molarity was increased to 8 M, synthesis at 110 °C for 1 h resulted in anatase and rutile formation as shown in Figure 5.1 (g). Orientation was also noticed in the structure. Increasing the dwell time to 3 h resulted in more rutile formation in the structure with further orientation. Further increase in the time to 6 h resulted in phase pure rutile formation. Intensity of peaks for (111) and (101) planes of rutile phase increased with increasing hydrothermal dwell time.

As the temperature was increased to 140 °C synthesis for 1 h resulted in formation of anatase and rutile phases in the structure as shown in Figure 5.1 (h). Orientation was noted in the structure. The amount of phases in the structure is given in Table 5.1. Rutile content increased with increasing hydrothermal dwell time to 3 h. Further increase of time resulted in anatase formation with a small amount of brookite phase implying the dissolution of rutile in the structure by acid catalyzer. The XRD patterns of the powders synthesized at 180 °C with 8 M acid catalyzer are shown in Figure 5.1 (i). 1 h of synthesis resulted in formation of anatase, rutile, and brookite phases. The amount of rutile and brookite is quite small as compared to that of anatase phase. An orientation could not be noted. As time increased to 3 h the intensities of anatase peak and rutile peak were increased. Brookite phase was not present. Further increase of time caused a decrease in the intensity of anatase peak and an increase in rutile share. This finding proved that the anatase phase also dissolved at 180 °C with HNO₃ catalyzer effect.

Low HNO₃ concentrations yielded anatase and brookite crystals rather than rutile crystals at 110 °C. Similar findings have been reported in literature [142]. In contrast, in mild acidic media and at low temperatures, the solid precipitates into small particles that have low solubility in the liquid. Therefore, Ostwald ripening is negligible and anatase as the precipitated phase preserved [212]. In

this study, phase pure brookite was not obtained in any experiments. However, at a given temperature, brookite phase share increases by increasing time and for a given time brookite phase formation is promoted as temperature increases. Strong acid concentrations resulted in rutile formation in the structure.

It is controversial to find the exact phase by changing time and temperature due to dissolution of phases in the solution which does not make it thermodynamics any more. The HNO₃ assisted hydrothermal synthesis produced anatase-rutile mixtures due to the fact that Ti has higher affinity to NO₃⁻ ions than to Cl⁻ ions, which promoted anatase crystallization [142]. As the acid concentration increased, amount of rutile phase in the structure increased. This finding is consistent with the suggestion that a large number of NO₃⁻ ions would favor corner shared bonding between the complex ions [142]. Corner shared bonding promotes rutile, whereas anatase is promoted with edge shared bonding.

Strong acid concentrations and high temperatures promote the protonation of Ti-O-Ti bridges and activate dissolution-precipitation reactions that ultimately lead to rutile. HNO₃ also promotes rutile formation [212]. For example Shen et al. [213] have reported that HNO₃ assisted hydrothermal synthesis with H-titanate precursor results in phase pure rutile by splitting of titanates when acid molarity is more than 7. However, 8 M acid molarity yielded the formation of a mixture of anatase and rutile phases when TTIP was used as the precursor in this study. Sample N813 includes anatase and rutile phases together with some amount of amorphous phase. The lower peak intensities of the crystalline phase(s) suggest that degree of crystallinity in this sample is less than the other samples synthesized.

Figure 5.2 (a) shows the XRD patterns of sample N800 which indicated peaks located at 25.4, 37.6, 48, 54, and 63° corresponding to the (101), (004), (200), (105), and (204) planes of the anatase phase (JCPDS 21-1272), respectively. The XRD analysis revealed that major amount of amorphous phase exists in the

as dried sample, and the crystallization process initiates before hydrothermal synthesis in the presence of NO_3^- ions in the solution.

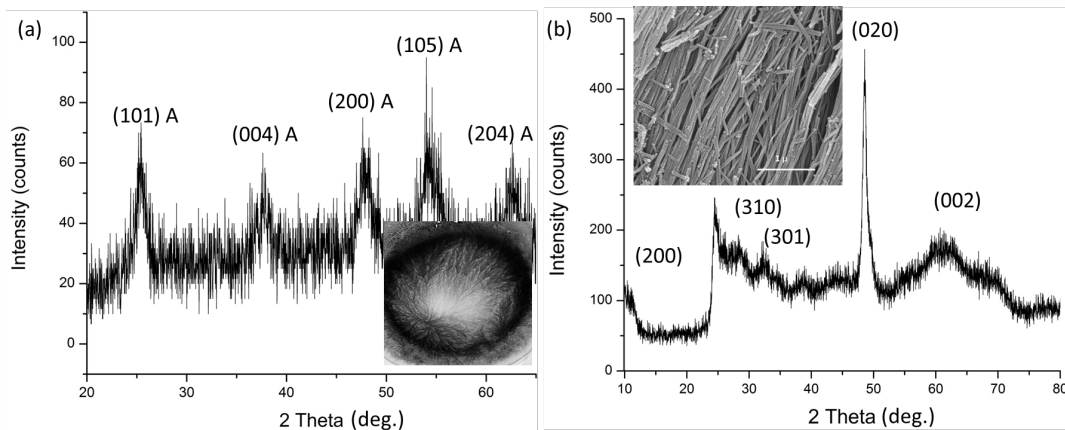


Figure 5.2 XRD patterns of (a) sample N800, inset shows photograph of precipitated powder, (b) H-titanate nanoribbons inset shows FESEM image of nanoribbons.

It is obvious that hydrothermal treatment promoted the crystallization process at temperatures as low as 110 °C, and enabled phase transformation from anatase to rutile phase. Upon hydrothermal treatment, the amorphous phase crystallized to anatase and rutile structures. The high pressure inside the reactor promoted the displacive and/or reconstructive transformations of crystallites, thus improved the crystallinity. Existence of rutile phase in samples N813 and N843 as opposed to sample N800 imply that the hydrothermal treatment favored the formation and growth of rutile crystallites. Further increase in synthesis temperature resulted in the existence of a mixture of anatase and rutile phases in the structure. As shown in Table 5.1, hydrothermal treatment of sample N843 yielded nearly equal amounts of anatase and rutile in the structure. When hydrothermal treatment temperature was increased to 180 °C keeping the acid molarity and time constant, the amount of anatase phase increased due to the smaller particle size obtained at this temperature which increased the surface energy. Furthermore, a mixture of anatase and rutile phases was obtained by 1 h

hydrothermal synthesis using 8 M acid concentration at 140 °C, while only anatase phase was obtained by 6 h hydrothermal synthesis in the same acid concentration and temperature. After 6 h of hydrothermal synthesis, the sample consisted of only anatase phase probably due to dissolution of rutile in the solution by the effect of severe acidic condition, and recrystallization to anatase.

Sample HN843, synthesized by inducing H-titanate nanoribbons, had only rutile phase as shown in the XRD pattern in Figure 5.3. The XRD pattern of hydrothermally synthesized nanoribbons is shown in Figure 5.2 (b) which indicates peaks at 9.4, 24.5, 28.5, 33.5, 48.5, and 62° corresponding to characteristic peaks of (200), (110), (310), (301), (020), and (002) planes of orthorhombic $H_2Ti_2O_5 \cdot H_2O$ (JCPDS Card No. 47-0124). The protonated titanates completely transformed to the rutile phase during hydrothermal treatment so that no trace of the titanates was detected in the XRD analysis.

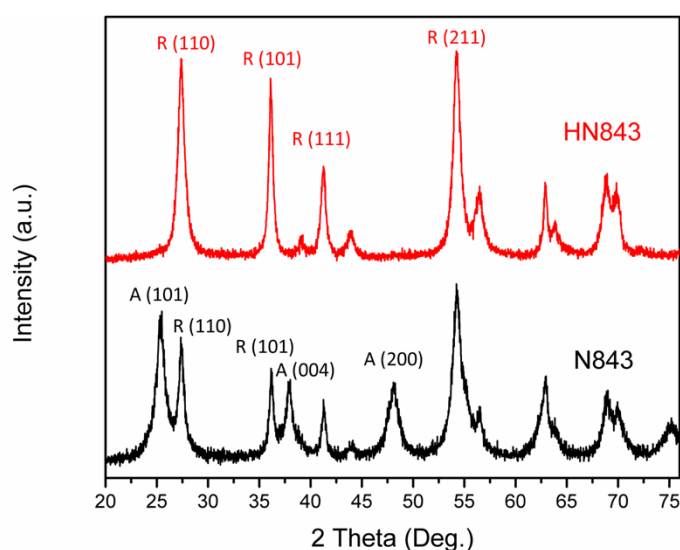


Figure 5.3 XRD patterns of samples N843 and HN843.

The calculated crystallite sizes of the selected samples showing no overlap during XRD analysis were presented also in Table 5.1. Among the hydrothermally synthesized powders, the smallest crystallite size (4.12 nm)

belonged to anatase crystals in sample N813. The largest crystallite size (10.46 nm) was measured for rutile crystals in sample HN843. Within the same sample, anatase crystals had smaller crystallite size than rutile crystals. The small difference between crystallite sizes of rutile and anatase may imply that anatase and rutile phases crystallized on the same crystallite. Conclusively, the crystallite size increases as the acid concentration, and hydrothermal synthesis temperature and duration are increased.

5.1.2 Morphological analysis

Figure 5.4 shows the FESEM analysis of powders synthesized at different temperatures and for different durations. As it is seen from the images, all the powders consist of nearly spherical nanostructures. The size of the powders is almost similar and any morphological difference of brookite phase could not be detected by FESEM analysis. As seen clearly in Figure 5.4 (a), there are some large particles that were probably crystallized in the early stages of the synthesis and grew as the time passed. These larger particles may be brookite phase and the dissolution may not be completed for these powders. In Figure 5.4 (b), a little bit smaller particles probably due to anatase phase domination in this structure were observed. Particle size distribution is almost homogenous in the structure. Figure 5.4 (c) shows the FESEM image of the powders synthesized at 140 for 6 h. Quite small particles are noticed in the structure. These powders were highly agglomerated possibly due to longer duration. In Figure 5.4 (d) the FESEM image of sample N181 indicates that nanoparticles were formed. These particles are probably the smallest nanostructures among all the structures synthesized. Although they are agglomerated, agglomeration was not more than the one observed in sample N146. Brookite phase was not detected in these powders because of the dissolution and recrystallization of the particles.

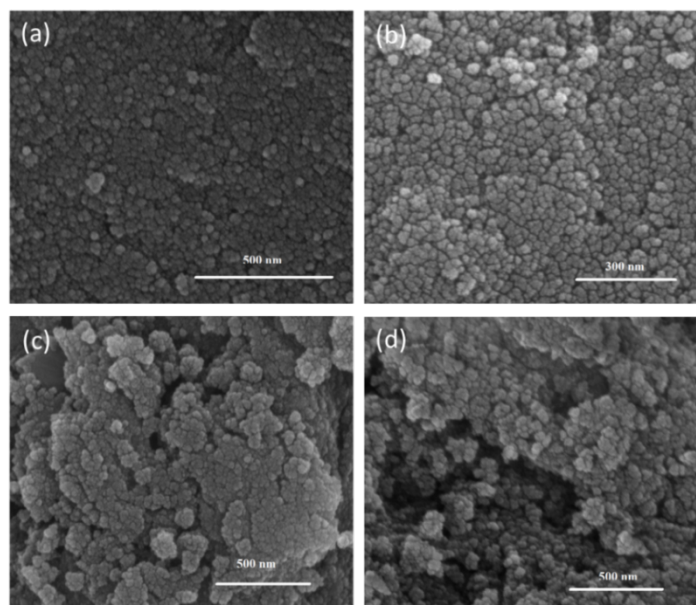


Figure 5.4 FESEM images of powders synthesized using 1 M acid catalyst at (a) 110 °C for 3 h, (b) 140 °C for 3 h, (c) 140 °C 6 h, (d) 180 °C for 1 h.

Figure 5.5 shows FESEM images of samples synthesized using 3 M acid catalyst. The oriented particles gathered in ellipsoid agglomerates as shown in Figure 5.5 (a). By the etching effect of catalyst, new particles formed in the structure which grew after 6 h as shown in Figure 5.5 (b). 1D structure was evolved at 140 °C. This newly evolved 1D structure shown in Figure 5.5 (c) grew on the ellipsoid shaped of agglomerates that also grew in 1D by the effect of acid catalyst. After 6 h synthesis, the 1D branched structures were dissolved again to form larger agglomerates as seen in Figure 5.5 (d). Powder synthesis at 180 °C resulted in larger nearly spherical particles with a size of nearly 40 nm. See Figure 5.5 (e). The particles agglomerated to a diameter of 200 nm without any particular shape. Further increase of duration to 6 h at 180 °C resulted in oriented ellipsoid agglomerates with some small nanoparticles as shown in Figure 5.5 (f).

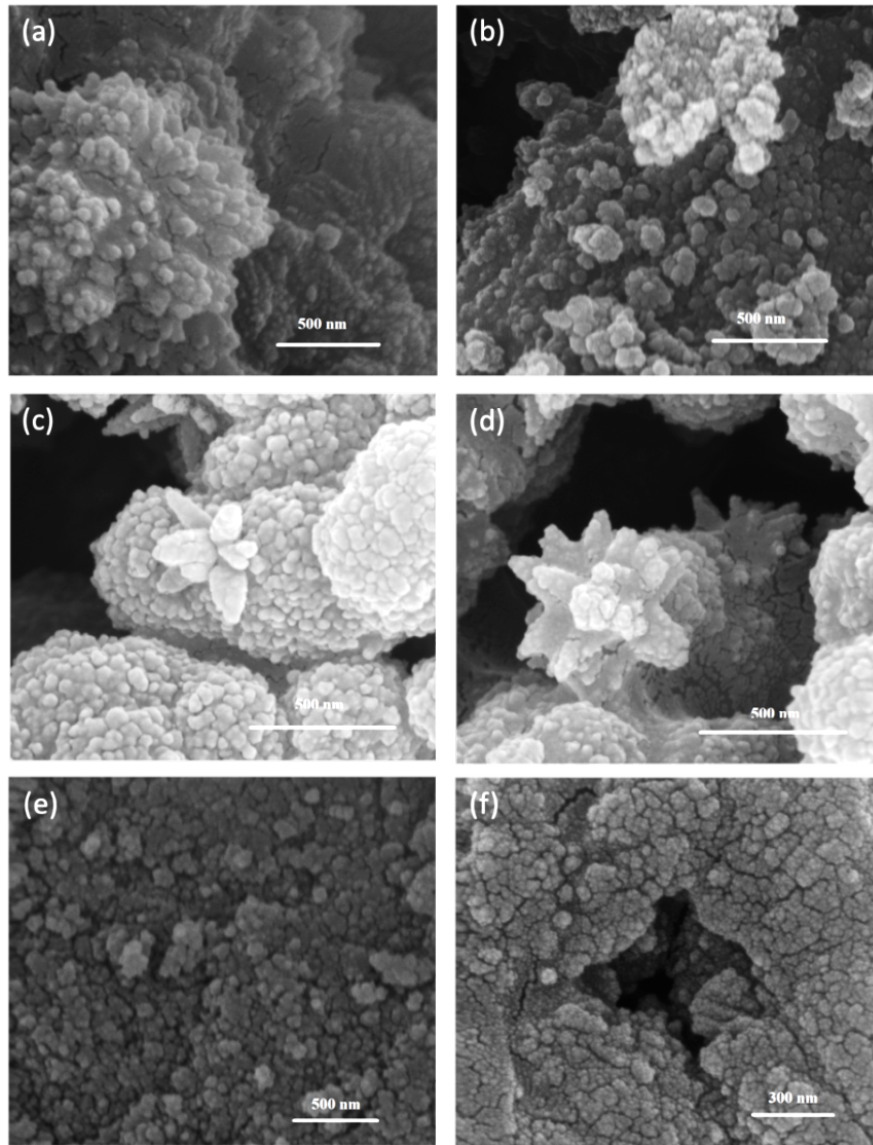


Figure 5.5 FESEM images of samples synthesized using 3 M acid catalyzer at (a) 110 °C for 1 h, (b) 110 °C for 6 h, (c) 140 °C for 3 h, (d) 140 °C for 6 h, (e) 180 °C for 3 h, and (f) 180 °C for 6 h.

Use of more amount of HNO_3 lead to a decrease in crystallite size in the powders. The development of a strong electrostatic repulsive force among the TiO_2 particles during peptization step and consequently formation of weakly agglomerated nanoparticles was probably responsible for this observation [212].

Figure 5.6 shows the FESEM images of the powders synthesized by using strong acidic concentrations. The morphology of sample N811, Figure 5.6 (a) consists of small particles with 1D orientation probably due to selective etching of acid catalyzer. Figure 5.6 (b) illustrates morphology of sample N813 that has highly porous arrays consisting of particles oriented through the inner side of array. Although this powder contains a mixture of anatase and rutile, no morphological difference was observed in this sample. Figure 5.6 (c) shows the morphology of sample N116 that is entirely in rutile structure. Oriented grains could easily be seen in the FESEM image. The rod-like structure stands in arrays touching to each other not separated. Etching of acid catalyzer dissolves some material that even rod edges touches to each other. Figure 5.6 shows the morphology of sample N841 that consists of anatase and rutile mixture. Oriented grains are also seen and edges of the rod like structures are more open in this sample. Figure 5.6 (c) shows morphology of sample N843 which again consists of anatase and rutile mixture. In this sample an exotic lotus-like structure was evolved among the ellipsoid aggregates. The domination of anatase phase increases the probability of being those ellipsoid particles in anatase crystal structure and lotus-like structure may be because of rutile. As stated earlier, orientation in rutile crystals is also noticed in the XRD patterns in Figure 5.1 (h). Figure 5.6 (d) shows powder morphological view of sample N841. Strong HNO_3 assisted hydrothermal synthesis at $140\text{ }^\circ\text{C}$ resulted in 1D oriented grains. However, rutile is very unstable under HNO_3 environment and may easily dissolve instead of growing. Thus, due to the need of low surface energy of anatase, this phase evolves in the solution. Rutile formation occurs accompanying to anatase. In Figure 5.6 (e), FESEM image of sample N843 shows ellipsoid agglomerates formed in lotus flower structure.

After 6 h of synthesis at $140\text{ }^\circ\text{C}$, all the oriented particles disappeared and small anatase particles formed as shown in Figure 5.6 (f) This observation proves rutile dissolution in HNO_3 environment. Synthesis at $180\text{ }^\circ\text{C}$ yields nanoparticles as shown in Figure 5.6 (g). These nanoparticles are in anatase

structure and did not transform to rutile. No orientation occurred after 3 h as shown in Figure 5.6 (h). After 6 h of synthesis, nanoparticles started to become oriented. However, 180 °C was not very proper for rutile existence and crystallinity decreased considerably as seen in Figure 5.6 (i).

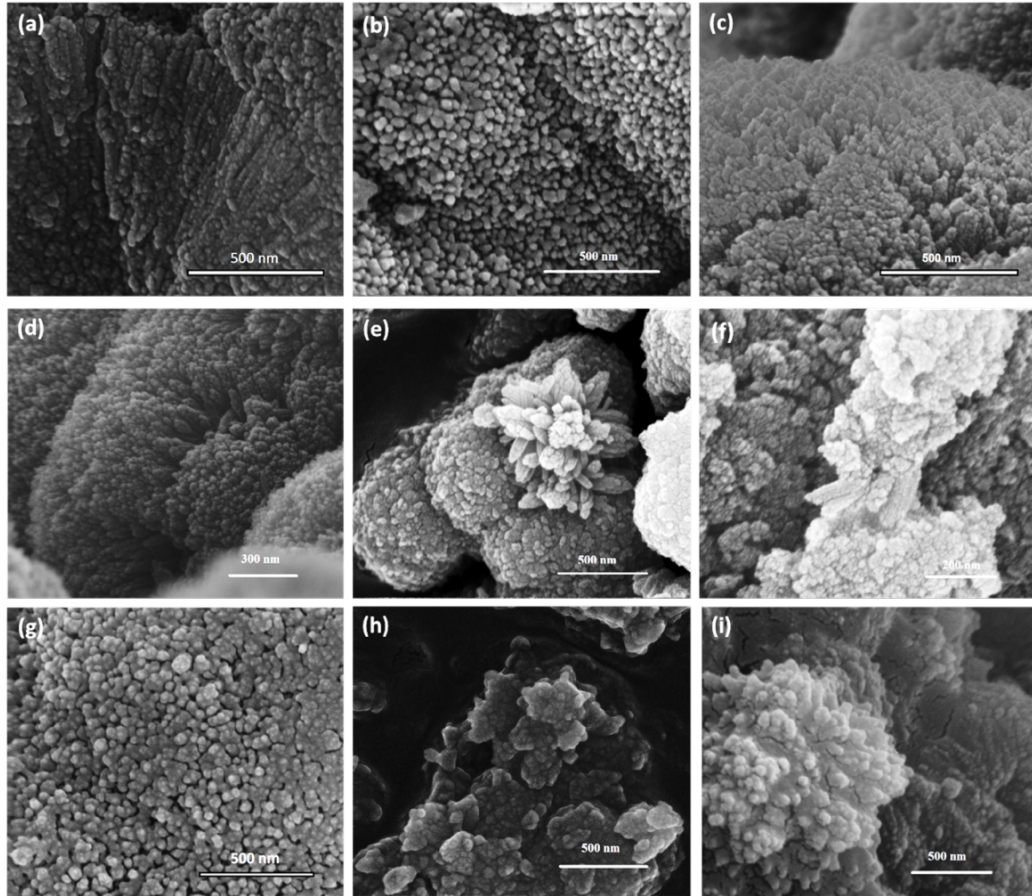


Figure 5.6 FESEM images of samples (a) N811, (b) N813, (c) N816, (d) N841, (e) N843, (f) N846, (g) N881, (h) N883, and (i) N886.

The crystallinity and morphology of the powders were also confirmed by SAED and HRTEM analyses. HRTEM analysis was conducted on samples N116, N386, N843, and HN843. The samples composed of anatase-rutile-brookite, rutile, anatase-rutile, and rutile phases, respectively and had nanosphere-like, nanoellipsoid-like, nanoellipsoids-nanoflowers, and nanoflowers morphologies,

respectively. HRTEM image of sample N116 shows the lattice fringes of three different phases inside as seen in Figure 5.7. The image depicts the domination of anatase phase with quite clear fringes belonging to anatase (004) planes, which is probably revealed by the acid etching effect. Rutile (110) planes are also detected in this region. There are some fringes which are not smooth in the image region. The lattice spacing of these fringes was calculated as 0.351, which corresponds to brookite (121) plane interlayer spacing. The destroyed symmetry that is a result of lattice distortion is attributed to the impurity elements like N. However, the morphology is not oriented and distortion is not considered to be a result of morphological variation. SAED pattern of the investigated area shows rings of polycrystalline material. The brightest ring which has a diameter of 5.3-5.6 nm shows the overlapping of anatase and brookite diffractions. The outer rings point out anatase 004, rutile 110, and brookite 121 planes.

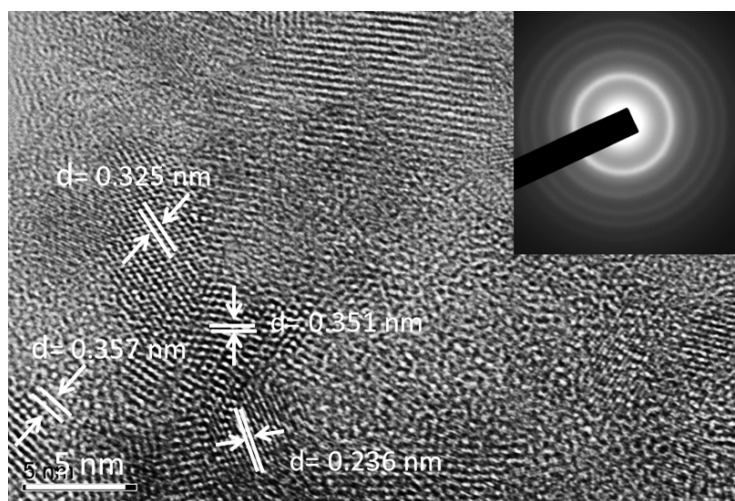


Figure 5.7 HRTEM image anatase, rutile and brookite region of sample N116 showing anatase, rutile and brookite region. Inset is the SAED pattern.

Figure 5.8 shows the sample N386 that consists of a large amount of rutile with a small share of anatase. As seen in Figure 5.8 (a) morphology consists of small grains that are single crystalline with clear (110) planes on the surface with a d

spacing of 0.33 nm. The increase in d spacing compared with the standard value is attributed to the fine grain size of powders. These particles are completely single crystalline and very porous as seen in Figure 5.8 (b). Grains are ellipsoid in shape with an average length of 7 nm and width of 4 nm signifying that there is a preferred orientation in the grains. In general, rutile powders smaller than 30 nm are very difficult to synthesis. Nonetheless, it is successfully realized in this experiment. Anatase fringes were not detected in HRTEM analysis. Only SAED analysis with a particular zone axis revealed {004} plane dots of anatase with {111} plane dots of rutile phase. In order to understand the mechanism for rutile formation in these powders, HRTEM analysis was done also for the powders synthesized at strong acidic conditions.

Flower shape structure was detected in the HRTEM analysis of sample N843 as depicted in Figure 5.9 (a) and (b). The agglomerated nanorods were determined as separating from the structure to yield a flower shape. Mali et al. [214] reported similar results. The surface planes of rods were determined by measuring the distance between fringes oriented in different directions. The measurements revealed that the d spacing is 3.33 Å between the fringes perpendicular to the rod axis as indicated in Figure 5.9 (c) and (d). This value of d spacing is ascribed to the (110) planes of rutile TiO₂. The findings suggest that the growth direction is [001] that is perpendicular to the [110] direction. The outcomes confirm to the interpretation that hydrothermal synthesis of Ti alkoxide with acid catalyzer results in single crystalline rods grew in the [001] direction [139]. The growth direction of oriented grain is obvious in Figure 5.9 (e) and (f) where the (110) planes are obvious. Underneath the (110) planes, anatase (004) planes at a d spacing of 2.37 Å are seen in the HRTEM image, which verifies that the crystallization of rutile phase occurs on the surface of anatase crystals during the hydrothermal synthesis.

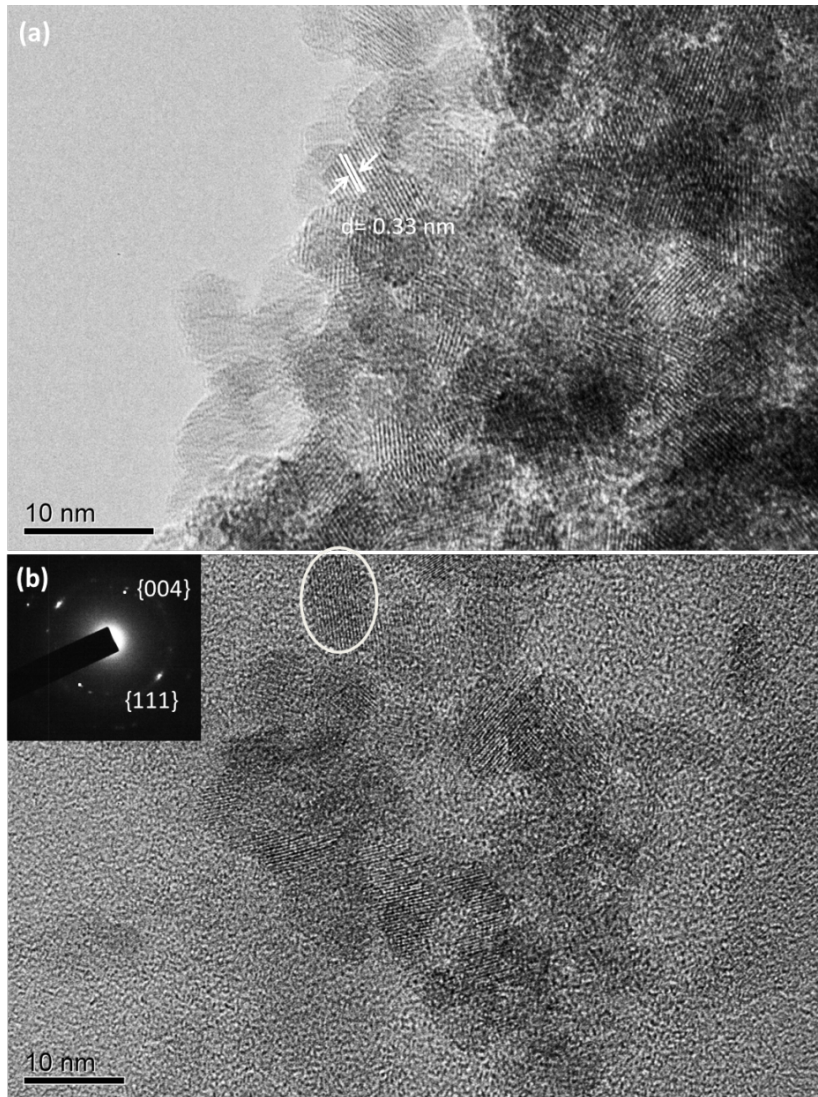


Figure 5.8 HRTEM image of sample N386 (b) Bright field image of powder inset SAED pattern showing (111) family of rutile (004) family of anatase.

SAED patterns of the sample, inset of Figure 5.9 (d) revealed the polycrystalline behavior of the structure. Anatase rings and rutile large spots are the two phases of the structure. The large spots of the (110) plane conform to the fringe measurements. The planes recognized by SAED analysis are tabulated in Table 5.2.

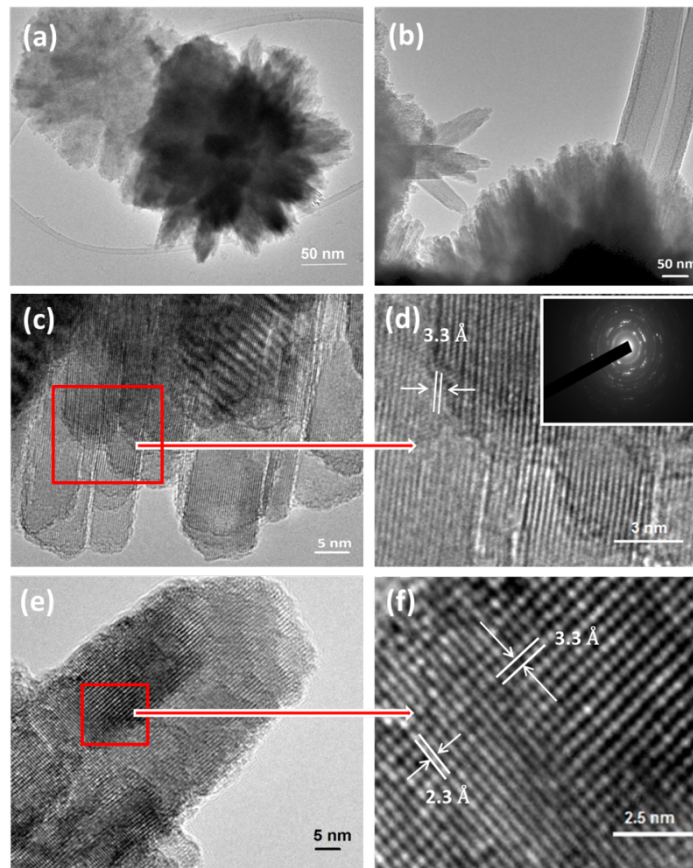


Figure 5.9 HRTEM images of sample N843 showing (a) general view, (b) rods, (c) fringes, (d) magnified view of the selected area given in (c) and inset image SAED pattern (diffraction planes are shown in Table 2), (e) growth of rutile on anatase, (f) view of the selected area in (e).

Table 5.2 Data obtained from SAED analysis of sample N843.

Reciprocal of Diameter (1/nm)	Interplanar spacing (Å)		Corresponding Crystallographic Plane (Phase)
	Calculated	Theoretical*	
5.62	3.55	3.52	101 (anatase)
6.00	3.33	3.25	110 (rutile)
7.87	2.54	2.49	101 (rutile)
8.42	2.37	2.38	004 (anatase)
8.70	2.29	2.29	001 (rutile)
9.16	2.18	2.19	111 (rutile)
11.722	1.71	1.70	105 (anatase)
12.50	1.60	1.57	211 (rutile)
13.31	1.50	1.48	204 (anatase)

*According to JCPDS database.

Figure 5.10 (a) shows the lattice fringes of the rutile ellipsoid crystallites in sample HN843 and histogram of the image. Distance 3.30 \AA between two lattice fringes corresponds to (110) plane of rutile. Figure 5.10 (b) shows a large flower structure taken from sample HN843. Anatase fringes were evidently lost in sample HN843. SAED pattern inserted to the image in Figure 5.10 (b) shows rutile diffraction spots. Enlargement of the crystallite resulted in smaller d spacing values. It is obvious from the comparison of Figure 5.9 and Figure 5.10 that even though samples N843 and HN843 were synthesized with the same hydrothermal test parameters, sample N843 consisted of rutile lotus 3D structure together with anatase nanocrystals but sample HN843 consisted of only rutile 3D structure due to the nanoribbon inducement.

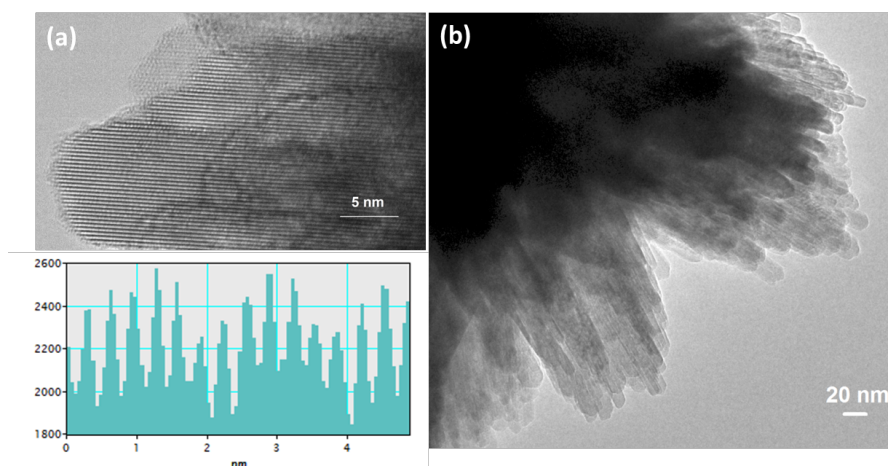


Figure 5.10 HRTEM images of sample powder HN843 (a) lattice fringes on the rods above picture histogram taken from the image, and (b) whole structure of one grain of sample HN843 consisting of small crystallizes.

5.1.3 Evolution Mechanism of TiO_2 nanostructures

In the light of the all experimental findings, the following mechanism is proposed for the evolution of TiO_2 nanostructures via strong HNO_3 assisted hydrothermal synthesis. The 3D structure is considered to reveal selective etching of the rod arrays in strong acidic media. The evolution of rods begins

with the formation of TiOH^{2+} by the hydrolysis of Ti^{3+} species. TiOH^{2+} oxidizes to Ti(IV) with dissolved O^{2-} in the solution. The Ti(IV) ions serve for growth units. Various morphologies of particles form by the influence of NO_3^- ions that promote anatase crystallization due to lower surface energy and affinity of NO_3^- ions to Ti atoms. Furthermore, the high pressure and temperature inside the reactor facilitate formation of anatase crystallites with a size less than 10 nm. In strong acid concentrations, anatase particles agglomerates quickly caused by the high energy of nanostructures. As the particles get bigger, their spherical shape changes to ellipsoids because of the compression of anatase crystal structure by the effect of strong acidic media as seen in Figure 5.8 (b). The (004) planes of anatase structure dominate the whole surface which were detected by SAED analysis of powders synthesized in 8 M acidic media as shown in Figure 5.9. The energetic planes increase the total energy of the system. Rutile transformation starts to decrease the energy. (110) plane of TiO_2 has the least energy according to the tight-binding model calculations that classify the surface energy of the planes in the order of $E(110) < E(100) < E(101) < E(001)$ [215]. Therefore, anatase to rutile phase transformation begins at the surface of the anatase structure. The high pressure inside the reactor should also be considered for anatase to rutile transformation. Since the molar volume of rutile is lower than anatase, high pressures favor anatase to rutile transformation. As a result of this transformation a core-shell structure evolves. The core-shell structure is etched by HNO_3 selectively to release the rutile surface of (110) planes. As the morphology turns into oriented grains, the growth of the most energetic plane of rutile (001) is limited by the NO_3^- ions in the solution. Thus, the oriented structure grows in the [001] direction forming a 1D structure in this plane. Because of etching, pedals grow in [001] direction and a lotus like structure forms. Similar results have been reported by Lin et al. [14] for the synthesis of rutile TiO_2 by HCl assisted hydrothermal treatment. Also those NO_3^- ions etches rutile that (111) plane of rutile was detected by SAED and XRD analysis clearly. Also experimental findings revealed that rutile planes

which dissolves easily in the HNO_3 solution compared to anatase because of the low resistance of its planes.

In the evolution of nanostructures, crystallography plays an important role as well. Both anatase and rutile phases are formed by TiO_6 octahedras arranged in different ways. Anatase phase is considered as a layered structure with more empty room outside TiO_6 octahedra and the layers are linked with each other by soft apical Ti–O bonds thus making its c direction to have good compressibility [216]. Consequently, compression of anatase from c axis is more practical than rutile. Thus, rutile growth continues based upon the skeleton formed by anatase structures. Anatase crystallization helps nanostructures to arrange in skew chains like the octahedral units inside the structure and is therefore vital for lotus structure formation.

Thermodynamically rutile is the most stable phase of TiO_2 for all processes catalyzed by HNO_3 at all temperatures in bulk scale in terms of free energy. However, as temperature increases particles are getting smaller and surface energy need arises in addition to formation energy. Energy required to form rutile surface is larger than anatase. Thus, anatase formation occurs for smaller crystallites. TiO_2 rod arrays grow on the surface of anatase grains by transformation of anatase to rutile phase assisted by temperature and pressure inside the reactor. However, rutile phase crystallized from anatase by surface transformation dissolves in the solution by the effect of strong acid at longer durations and anatase crystallizes again after 6 h.

In the case of inducing protonated H-titanate nanoribbons as nucleation site in the hydrothermal synthesis of TiO_2 nanostructures, H-titanate nanoribbons undertake, at least in part, the role of anatase structure. Anatase or rutile crystallites grow on H-titanate nanoribbons. Since the final structure is rutile, titanates are assumed to transform to rutile phase by splitting during hydrothermal treatment. While the transformations take place, released TiO_6 octahedras also serve as nucleation sites to attract the Ti atoms and complete the

crystallization. The H-titanate nanoribbons are considered to increase the rate of anatase crystallization and anatase to rutile transformation. Thus, complete crystallization of anatase or rutile occurs together with surface transformation of anatase to rutile structure. At the end of the hydrothermal treatment, a phase pure rutile 3D nanostructure evolving from agglomerated rutile nanorods via etching effect of HNO_3 is realized.

5.1.4 Photocatalytic activity of powders

The photocatalytic activity of selected powders with the highest crystallinity in terms of crystal structure and morphology was measured with respect to MB degradation. MB absorbance graphics of the selected powders synthesized are given in Figure 5.11. The powders synthesized using HNO_3 catalyzer showed very low photoactivity as compared to commercial TiO_2 powder, Degussa P25. The low photoactivity of the powders is probably due to highly oxidation ability of nitric acid catalyzer that provides good crystallinity but very low oxygen vacancy as discussed in Section 2.4. Another possible effect is NO_x species adsorbed to the TiO_2 surface inhibits photoactivity. During the test, observation with naked eyes revealed that MB molecules do not adsorb to the surface. After more washing repeat, photocatalytic activity increased a bit with adsorbing some of the MB molecules on the surface. In order to create oxygen vacancies, metal and nonmetal doping was done to the powders since better performance in DSSC and n-type semiconductor can be only achieved by oxygen vacancies. The oxygen vacancies were tried to accomplish by destroying neutral equilibrium. Results of the experiments of mono- and co-doping of TiO_2 is explained in Chapter 6.

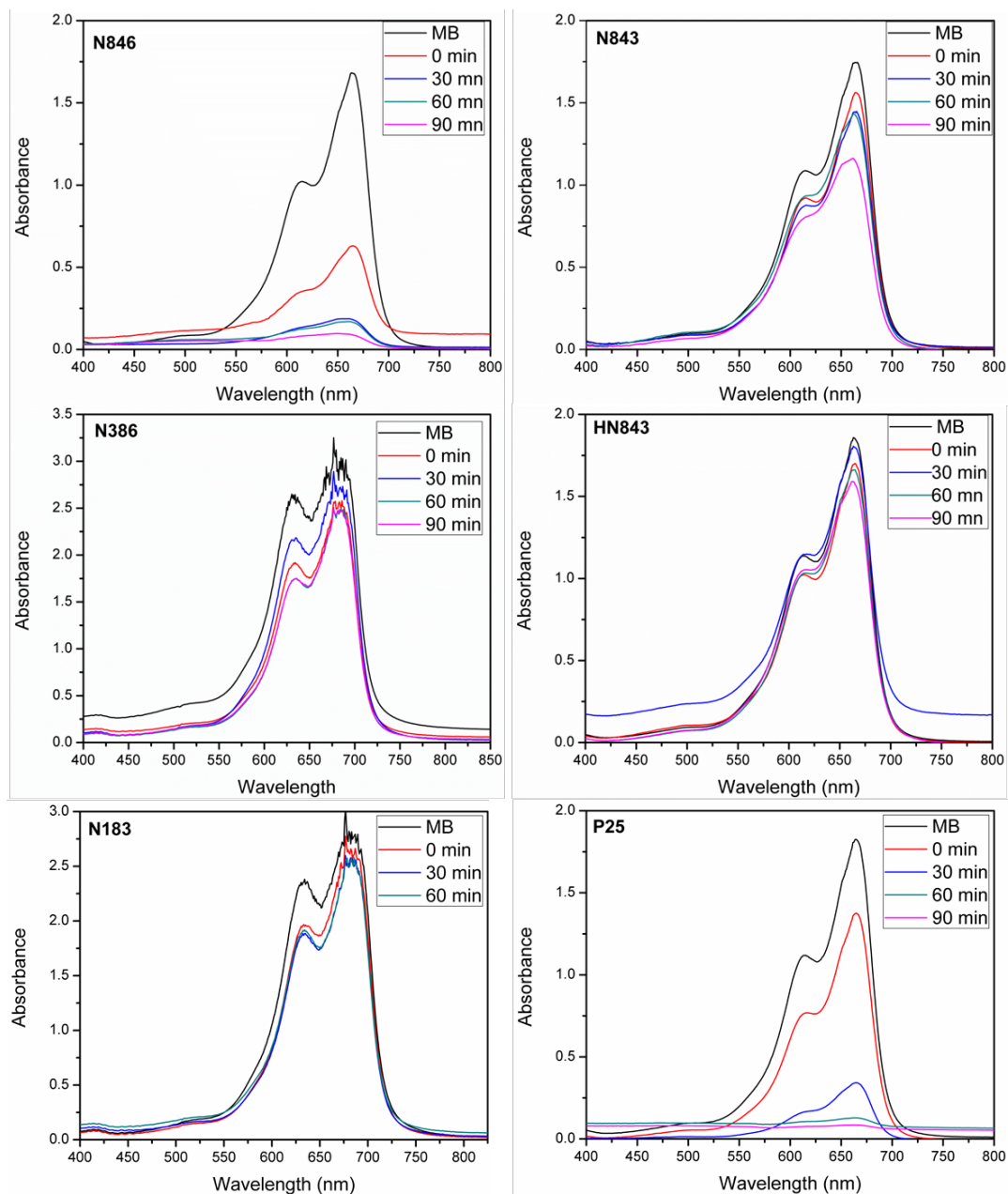


Figure 5.11 Absorbance spectra of solutions containing MB and powders.

CHAPTER 6

RESULTS and DISCUSSION: MONO-, CO- and TRIPLE-DOPING of TiO₂ NANOSTRUCTURES with Mo, Fe and N

6.1 General

The powders synthesized using HNO₃ catalyzer exhibited far less photocatalytic activity than P25 powder shows due to high oxidation conditions in the autoclave, which demolished the non-stoichiometry of TiO₂ and created oxygen deficient sites. Thus, doping was tried to improve the photocatalytic activity of TiO₂ powders. The purpose of this study was to enhance the light response and photocatalytic properties of rutile titania through mono-, co-, and triple- doping with Mo, Fe, and N through hydrothermal treatment and, to evaluate the optical properties of the structures synthesized. The photocatalytic activity of the doped TiO₂ powders was evaluated in terms of the degradation of MB solution under UV-light illumination. An optimum amount for each of the dopants was proposed for gaining the best photocatalytic performance. A formation mechanism was proposed for rutile titania. Photoactivity of powders were determined to investigate the suitability of these powders for DSSC applications.

6.1.1 XRD analysis

The XRD patterns of the undoped TiO₂ powder and the powders synthesized via HNO₃ assisted hydrothermal treatment using Mo and Fe as dopants are illustrated in Figure 6.1. The peak locations and their relative intensities for the phases shown were all cited from the JCPDS database. All powders showed the characteristic peaks corresponding to the rutile (JCPDS 21-1276) and/or anatase (JCPDS 21-1272) phases. No other peaks belonging to any other phases were detected suggesting that Fe³⁺ and Mo⁶⁺ ions doped into the TiO₂ lattice either by

substituting Ti^{4+} ions or taking a vacant position in the lattice. Nevertheless, XRD analysis may not be capable of detecting the Fe and Mo containing phases since the amount of Mo and Fe are small so that they are below the detection limit of the diffractometer.

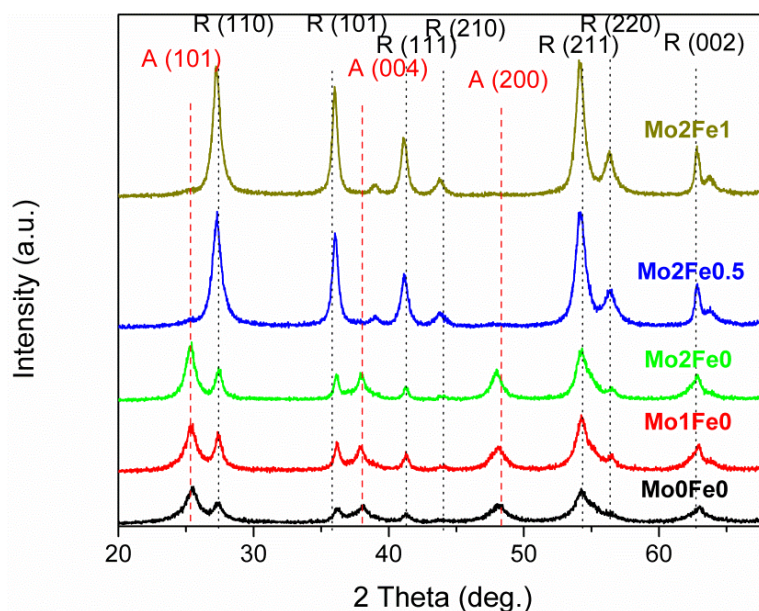


Figure 6.1 XRD patterns of un-doped, mono-doped and co-doped powders.

The XRD pattern of the undoped TiO_2 powder, sample Mo_0Fe_0 , shows peaks of both anatase and rutile planes as indicated in Figure 6.1. The anatase phase evolves when HNO_3 catalyzer is used during the hydrothermal process due to the high affinity of Ti atoms to NO_3^- ions [142]. Also, the autogenous pressure inside the reactor favors anatase formation instead of rutile, which results in transformation since rutile is a low temperature stable polymorph of TiO_2 . Thus, a mixture of anatase and rutile phases develops during hydrothermal synthesis as explained in detail in Section 5.1.1. Lower intensity of peaks in the XRD pattern as compared to the peaks in the doped-powders suggests that the amount of crystallinity in the undoped TiO_2 powder is lower than the crystallinity in the doped powders. Intensity of the XRD peaks increased by Mo doping as seen in the patterns in red and green color as depicted in Figure 6.1. The addition of 1 wt % Mo leads anatase

formation. But, rutile formation is promoted as Mo amount is increased to 2 wt % suggesting that Mo atoms first settle into anatase unit cell, then further doping promotes settlement of Mo atoms into the rutile structure. Anatase crystals start to transform to rutile crystals due to lattice deformation.

The XRD patterns of the Mo and Fe co-doped samples, in blue and yellow color in Figure 6.1, revealed that the anatase phase did not persist in these powders. Anatase crystals either might not form or might transform to rutile crystals during hydrothermal dwell. Increasing Fe dopant revealed sharper peaks with higher intensity. The intensity of (111) plane of rutile was more than the standard intensity of this plane with respect to (110) plane, suggesting that the dopant(s) exists in the lattice causing some change in the lattice structure.

Average grain size, crystal structure, and phase constituents detected by Rigaku 4.2 software were tabulated in Table 6.1. Mean crystallite size calculations revealed that doping of 1 wt % Mo into TiO₂ lattice increased the size of both anatase and rutile crystals. The increase in the size of the crystals is attributed to better crystallization caused by the dopant element that may decrease the etching effect of the acid catalyzer, in particular for the rutile crystals. In contrast, further increase of Mo to 2 wt % decreased the crystallite size probably due to suppressing effect of Mo atoms on the growth of crystallites. When 0.5 wt % Fe was doped to the structure, the crystallite size decreased further due to similar reasons with Mo while the crystallinity increased. However, further increases of Fe to 1 wt % increased the rutile crystallite size, following the trend of increasing crystallinity due to inhibiting solubility of the phase in HNO₃ solution. At this moment it is worthy to mention that dopant Fe atoms could be oxidized and play a significant role as a nucleation site for rutile phase crystallization.

Lattice parameters calculated by using XRD data were tabulated in Table 6.2. The “c” parameter of the anatase increased gradually while the “a” parameter remained almost constant despite increasing Mo doping although the ionic radii of Mo⁺⁶ is smaller than Ti⁺⁴. This finding supports increasing in the proportion of rutile phase

Table 6.1 Codes, crystal structures, crystallite size values and BET surface area of the samples.

Sample Code	Weight percentage of phases		Crystallite size of the phases (nm)		BET surface area (m ² /g)
	Anatase	Rutile	Anatase	Rutile	
Mo0Fe0	55	45	6.98	8.34	244.7
Mo1Fe0	47	53	9.80	13.18	128.8
Mo2Fe0	61	39	7.27	9.51	217.7
Mo2Fe0.5	0	>99	-	9.19	242.7
Mo2Fe1	0	>99	-	10.48	174.4

crystals in the structure by increasing the c parameter of anatase. Rutile lattice constants were more or less the same with those obtained by 1 wt % Mo doping signifying that Mo atom prefers to settle down in anatase structure and forces the structure to transform rutile by some lattice distortions. This is probably due to atomic interactions between Mo-O-Ti linking. When Mo doping was increased to 2 wt %, both “a” and “c” parameters increased meaning that Mo atoms started to diffuse into the rutile lattice or anatase crystals transform to rutile phase. Diffusion of Mo into the crystal lattice creates distortion which may also cause a decrease in crystallite size. The “a” parameter of the rutile increased while the “c” parameter decreased when Fe was incorporated to the structure, which has smaller ionic radii though. This may be also a result of rutile stabilization. Increasing “a” parameter may be a result of distortion by an extra dopant with Fe insertion.

Table 6.2 Crystallographic data of the powders synthesized.

Sample	2θ degree						Crystal Lattice	Crystal structure parameters			
	Anatase			Rutile				Anatase		Rutile	
	101	004	200	110	101	111	a	c	a	c	
	Mo0Fe0	25.38	38.02	48.19	27.40	36.14	41.30	T	3.77	9.46	4.59
Mo1Fe0	25.37	37.90	48.18	27.40	36.14	41.30	T	3.77	9.49	4.59	2.95
Mo2Fe0	25.32	37.81	48.08	27.40	35.98	41.10	T	3.78	9.51	4.59	2.97
Mo2Fe0.5	-	-	-	27.38	36.05	41.12	T	-	-	4.60	2.96
Mo2Fe1	-	-	-	27.36	36.00	41.0	T	-	-	4.60	2.96

*T=Tetragonal

BET surface area measurements revealed that sample Mo0Fe0 had the largest surface area, which had the smallest crystallite size for both anatase and rutile phases. Mo doping into the structure initially decreases the surface area due to the enlargement of crystallites. But further doping of Mo atoms in the structure increases the surface area as a result of the decrease in crystallite. Fe doping to the structure increased the surface area. This finding supported the data calculated for size of crystallites. However, 1 wt % Fe doping decreased the surface area since it consists of only rutile phase, and powders consisting of phase pure rutile have a large surface area.

6.1.2 ICP and XPS analysis

Table 6.3 presents the data obtained from ICP and XPS analyses for the powders. ICP analysis revealed that 71 wt % of the Mo atoms successfully placed in TiO₂ lattice by mono-doping. 80 % of the added Fe atoms and 52 % of the added Mo atoms placed in the lattice of TiO₂ in the case of co-doping. A decrease in Mo placement in the co-doped powder suggests more placement of the Fe atoms in the rutile titania crystal structure than the Mo atoms. This is probably due to proper ionic valance of Fe³⁺, which is closer to Ti⁴⁺ as compared to Mo⁶⁺. The settlement location and ionic radii of Fe³⁺ may also play a significant role. When the surface atomic concentrations were examined, Mo is detected in a lower value for both powders Mo1Fe0 and Mo2Fe0.5 as compared to the ICP results. However, quite less Fe was detected for sample Mo2Fe0.5 as compared to the ICP result. Also N was detected in all of the undoped, mono-doped, and co-doped samples. The highest amount of N was detected in sample Mo2Fe0.5 that might be called as triple-doped TiO₂ powder.

XPS spectra of samples Mo0Fe0, Mo1Fe0 and Mo2Fe0.5 are illustrated in Figure 6.2. The Ti2p_{3/2}, and Ti2p_{1/2} peaks of the samples are shown in Figure 6.2 (a). Ti2p peaks of samples Mo1Fe0 and Mo2Fe0.5 shifted to higher binding energies while the Ti2p_{3/2} peak of sample Mo0Fe0 kept its characteristic position. The shift

Table 6.3 Bulk and surface elemental compositions according to ICP and XPS analyses of powders.

Sample	ICP results (wt %)		Surface atomic concentration (at %)				
	Mo	Fe	Mo	Fe	N	Ti	O
Mo0Fe0	-	-	x	x	1.66	26.56	71.28
Mo1Fe0	0.79	x	0.53	x	1.59	29.11	68.38
Mo2Fe0	1.41	x	-	-	-	-	-
Mo2Fe0.5	1.03	0.39	0.86	0.14	4.10	29.51	65.12
Mo2Fe1	-	-	-	-	-	-	-

of binding energy is obvious for sample Mo2Fe0.5. This finding indicates that chemical bonding varied in sample Mo1Fe0 and especially in sample Mo2Fe0.5. The variation in chemical bonding is a possible result which is explained by the existence of Mo and/or Fe atoms replacing Ti atoms. The O1s XPS spectra of the samples are shown in Figure 6.2 (b). There are 2 overlapping peaks in the spectra.

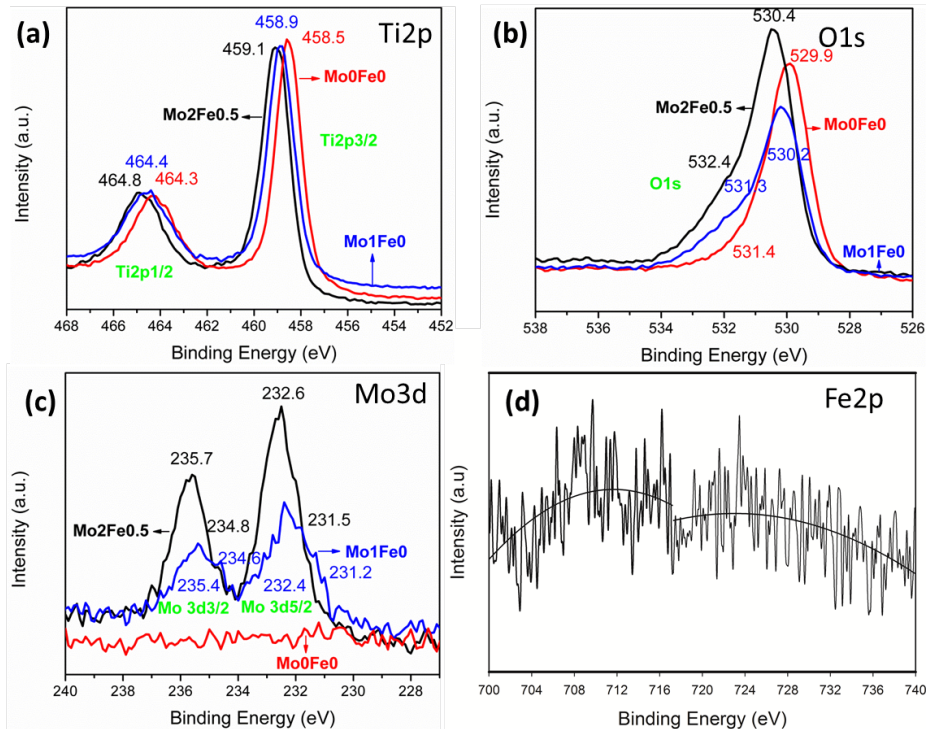


Figure 6.2 XPS spectra of powders Mo0Fe0, Mo1Fe0, and Mo2Fe0.5 (a) Ti2p, (b) O1s, (c) Mo3d, and (d) Fe2p.

The relatively low binding energy component may be associated with the crystal lattice oxygen in the oxide and higher binding energy component is attributed to the surface hydroxyl groups (Ti-OH). Sample Mo2Fe0.5 has the highest binding energy component of O due to the presence of oxygen ions in oxygen-deficient regions within the oxide matrix. Sample Mo1Fe0 has relatively higher binding energy component for hydroxyl groups as compared to Mo0Fe0. This finding is important for oxygen deficiency and correlatively for photoactivity.

Figure 6.2 (c) shows the Mo spectra of samples Mo0Fe0, Mo1Fe0, and Mo2Fe1. The two peaks suggest 2 different oxidation states for samples Mo1Fe0 and Mo2Fe0.5. The largest peak belongs to Mo(VI), indicating that the main valences of Mo in the samples were 6+, which are located at 232.6 eV and 235.7 eV while peaks located at 231.5 eV and 234.8 eV corresponded to Mo⁵⁺ [181]. The finding is interpreted as follows: most of the doped Mo ions exist as Mo⁶⁺ ions in TiO₂ lattice, but only some of the Mo ions are in Mo⁵⁺ ions. The presence of Mo⁵⁺ ions signifies inadequate oxygen in TiO₂ lattice to support Mo⁶⁺ ions. Thus, the existence of Mo⁵⁺ ions implies that sample Mo2Fe0.5 is in an oxygen deficient state (as one titanium atom needs two O atoms but one molybdenum atom needs three O atoms). The deficiency of O may be better for adsorbing oxygen, which is beneficial to photocatalytic degradation [217]. Figure 6.2 (d) shows the Fe 2p XPS spectrum of Mo1Fe0.5. Although the ICP analysis suggested 0.39 wt % Fe, the XPS analysis did not reveal an identical amount of Fe as indicated in Table 6.3. The difference between the results of the ICP and XPS analyses questions whether Fe atoms exist in the structure or not. XPS is a surface analysis technique, and oxidized Fe atoms settle in the core of the 3D structure to serve as a nucleation seed [218]. Alternatively, the two peaks belonging to the binding energies of the Fe 2p XPS peaks may have adapted to Fe³⁺ ions and settled as dopant in sample Mo2Fe0.5. This data exhibits a positive shift as compared to those in Fe₂O₃ (710.7 eV for 2p_{3/2} and 724.3 eV for 2p_{1/2}) the TiO₂ lattice forming Fe–O–Ti bonds and the electrons transferred from Fe³⁺ to Ti⁴⁺ species [219].

Figure 6.3 shows N1s spectra of un-doped, mono-doped and co-doped powders synthesized using strong acidic (8M) media. First, N1s peak was detected in all three powders. The highest peak intensity was obtained in co-doped powder, sample Mo2Fe0.5. This consequence reveals that doping of metal ions promotes solubility of N in the structure. A 396.9 eV is the typical binding energy of N and is attributed to the interstitial doping. The broad peak between 396–403 eV verifies the coexistence of substitutional and interstitial placement of N within the structure [220]. A N peak below 398 eV is attributed to the replacement of O atoms and peaks above 398 eV are attributed to NO_x species. XPS peaks of samples Mo0Fe0 and Mo1Fe0 at 400.3 eV and Mo2Fe0.5 at 400.1 eV may also be a result of Ti-N-O bonds. Based on to the electronegativity of the doped metal, linkage for sample Mo2Fe0.5 may be Mo-N-O and/or Fe-N-O. In general, the peak of N1s in the XPS spectrum ranges from 396–404 eV [167]. However, the binding energy of N1s is more controversial as it is highly dependent on the synthesis method. There are various chemical states of N doped into TiO₂ lattice the forms of N-Ti-O and Ti-O-N linkages that coexist in sample Mo2Fe0.5. The findings are in agreement with those reported in literature [167, 220].

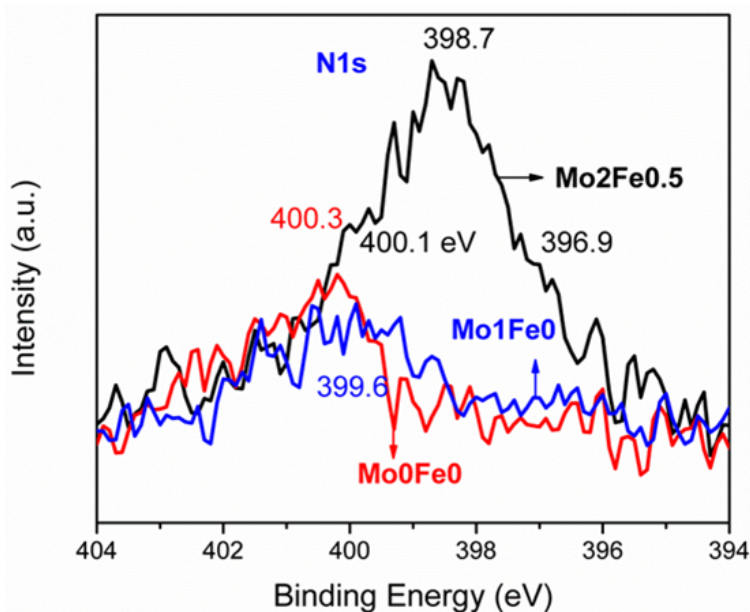


Figure 6.3 N1s XPS spectra of samples.

6.2 Microstructural analysis

Figure 6.4 shows the FESEM images of un-doped, mono-doped and co-doped TiO₂ nanostructures synthesized using various amounts of Mo and Fe dopants by HNO₃ assisted hydrothermal treatment. Figure 6.4 (a) shows the morphology of sample Mo0Fe0, which has flower-like rod arrays with a diameter of nearly 0.5 μm and spherical agglomerates with a diameter nearly 500 μm consisting ellipsoid nanoparticles. 1D structure was explained to be formed by the etching effect of anions in the solution to reveal a 3D microstructure as mentioned in previous chapter. The anatase and rutile phase mixture was reported to be existed in a core shell structure caused by the surface transformation from anatase to rutile that was obtained from 1D units as explained in Chapter 5. The anatase and rutile phase mixture existed in a core shell structure caused by the surface transformation from anatase to rutile. By adding Mo into the structure, particles became enlarged rod arrays made of small nano crystallites as illustrated in Figure 6.4 (b). The particle arrays shown in Figure 6.4 (a) were not observed in this sample. Figure 6.4 (c) shows the FESEM image of the powder that has 0.5 wt % Fe as a co-doping element. The number of rods increased by decreasing the width of individual rods in arrays. The increase is due to better crystallization besides etching, which may be caused by oxidized Fe in the core of the structure. Further increase of Fe doping to 1 wt % resulted in a microstructure with a diameter of nearly 3 μm composed of closely-spaced larger rod arrays as shown in Figure 6.4 (d). In this sample, the individual rod diameter decreased even further. Also crystallite size calculations and very high surface area of the powders analyzed by BET analysis revealed structures composed of nanocrystallites with an inner porosity forming a 3D structure.

Figure 6.5 shows the HRTEM images of samples Mo0Fe0, Mo2Fe0.5, and Mo2Fe1. A flower structure formed in sample Mo0Fe0 through a surface transformation from anatase to rutile, and growth occurred in the same [001] direction. The rod units have a diameter of nearly 10 nm each as seen in Figure 6.5 (a). The pure rod formation in sample Mo2Fe0.5 is shown in Figure 6.5 (b) with an

average diameter of 20 nm. Figure 6.5 (c) shows the lattice fringes of one of the rods of sample Mo0Fe0.5.

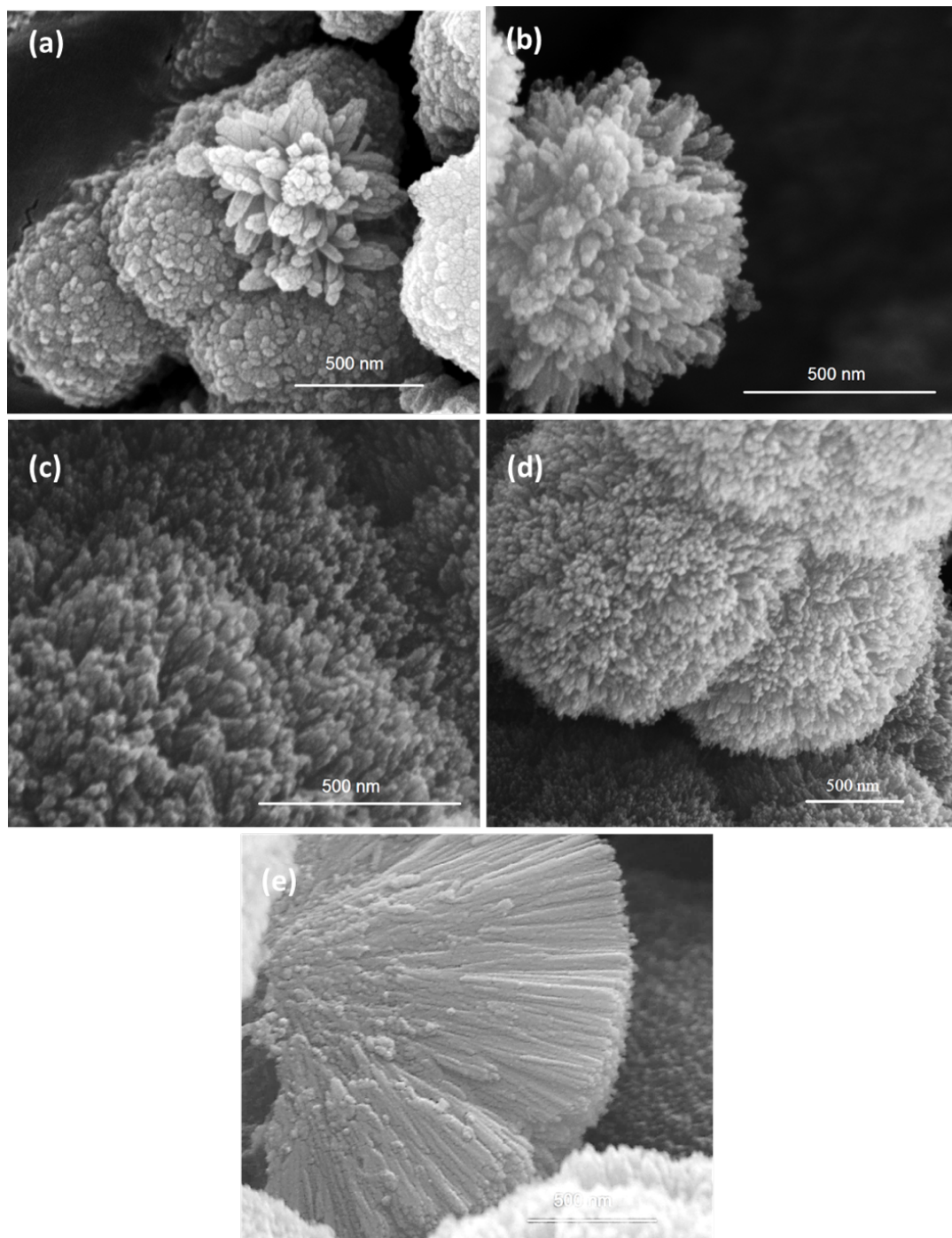


Figure 6.4 FESEM images of powders (a) Mo0Fe0, (b) Mo1Fe0, (c) Mo2Fe0, (d) Mo2Fe0.5, (e) Mo2Fe1.

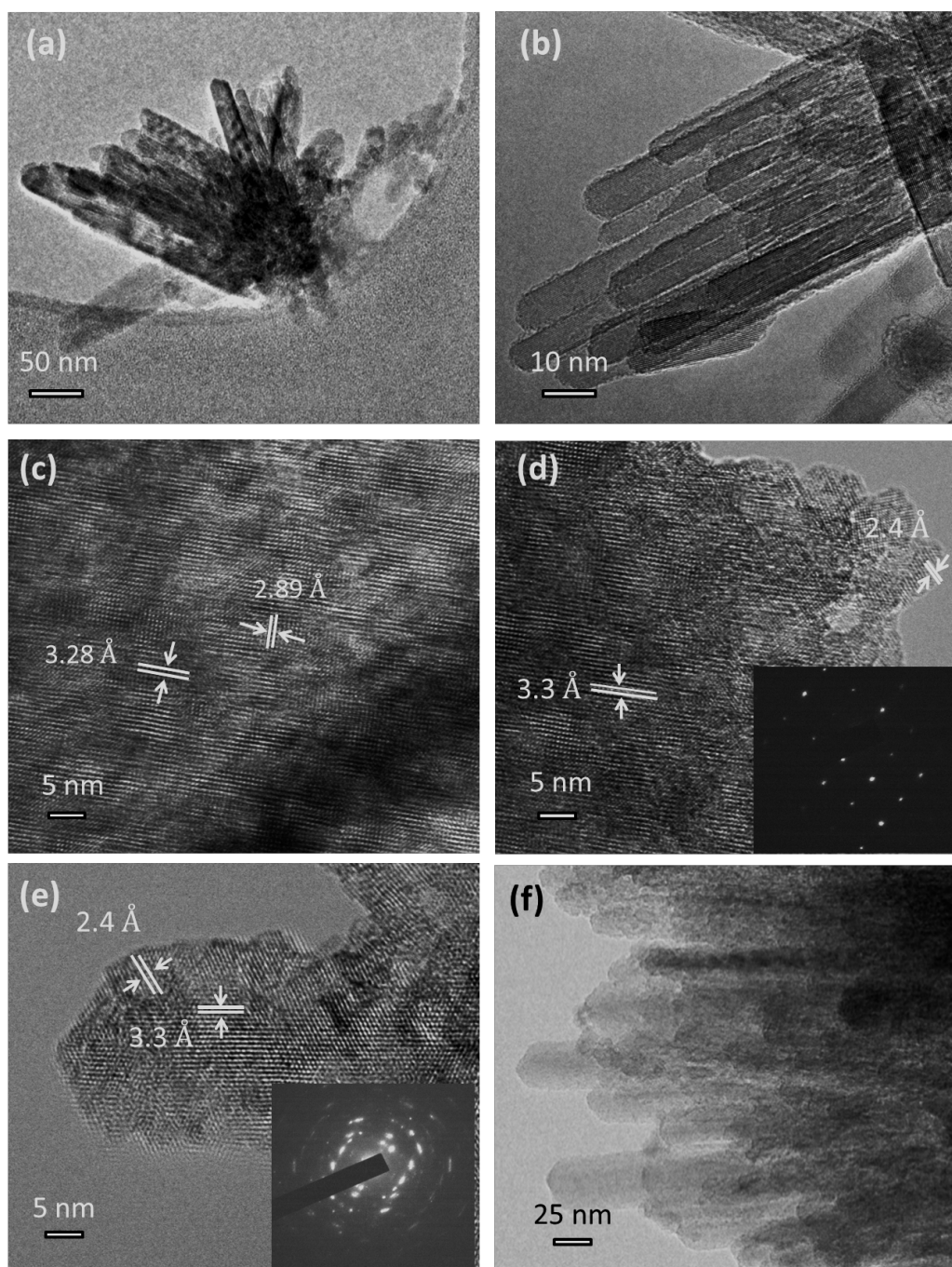


Figure 6.5 HRTEM images of un-doped and co-doped powders (a) Mo_0Fe_0 , (b) $\text{Mo}_2\text{Fe}_{0.5}$, (c) lattice fringes of unit rod in $\text{Mo}_2\text{Fe}_{0.5}$, (d) lattice fringes of edge of unit rod in $\text{Mo}_2\text{Fe}_{0.5}$ inset shows SAED pattern, (e) lattice fringes of unit rod in sample Mo_2Fe_1 , inset shows SAED pattern, and (f) enlarged rods of Mo_2Fe_1 .

Figure 6.5 (d) shows edge of the rods in this sample, which were covered by an amorphous phase. This amorphous phase may play a beneficial role in terms of photocatalytic properties because amorphous transition metal oxides increase the adsorption of MB. When the edges of the rods are examined carefully, a different d spacing value of 2.4 Å belonging to (060) plane of the MoO_3 phase is distinguished. SAED pattern inserted into the image shows dots belonging to (110) plane of rutile. However different oriented fringes are very clear in the main image as indicated in Figure 6.5 (d). Figure 6.5 (e) shows the rod edge of sample Mo_2Fe_1 . It is evident that MoO_3 crystallization increased on the (110) plane of rutile by taking out the Mo atoms from the bulk structure due to Fe ion placement. SAED pattern of this sample also shows polycrystalline behavior as seen in the inset in the image. Rod structure was also inserted as an inset image. Figure 6.5 (f) shows low magnification of rods shown in Figure 6.5. The EDS spectrum of sample Mo_2Fe_1 can be seen in Figure 6.6. The EDS analysis revealed that the sample consists of Ti, Mo, and Fe elements.

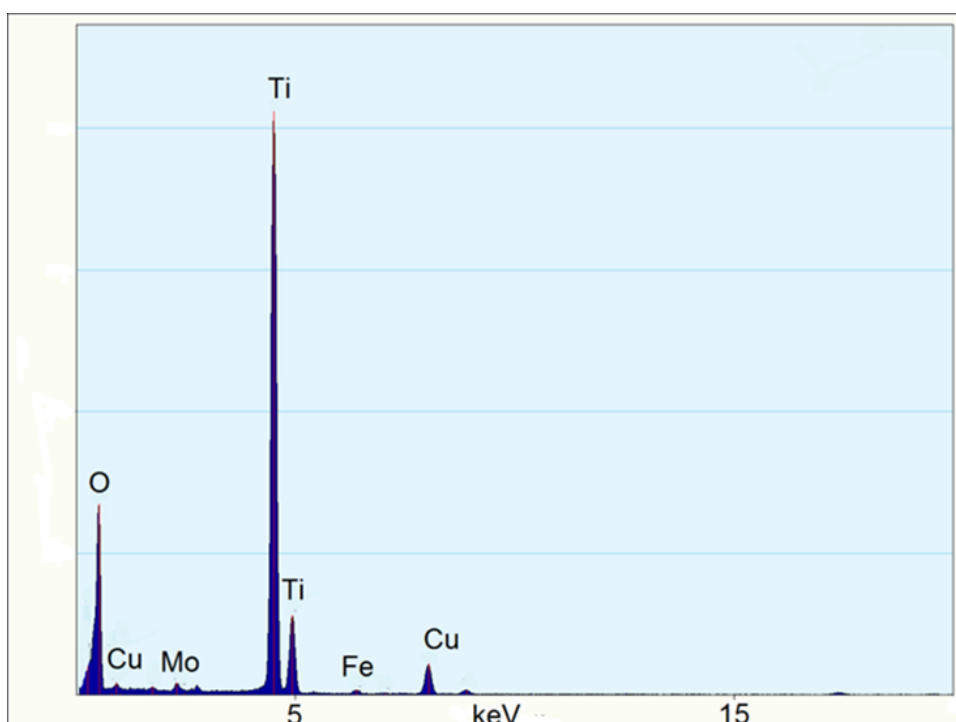


Figure 6.6 EDS analysis of sample Mo_2Fe_1 .

6.2.1 UV-Vis spectrophotometer and methylene blue photo-degradation test

UV-visible absorption spectra and Kubelka-Munk transformed band gap energies of samples Mo0Fe0, Mo1Fe0, Mo2Fe0, Mo2Fe0.5, and Mo2Fe1 are shown in Figure 6.7. Band gap energies for the powders, calculated by extrapolating the curve of $E_g - E$, are shown in Table 6.4. Sample Mo0Fe0 shows a considerable red shift due to the co-existence of anatase and rutile in the structure. These two phases shows a synergistic effect as previously reported by Quesada-Cabrera et al. [221]. When Mo is mono-doped and when Mo and Fe are co-doped to the structure, each atom incorporated to the structure steadily triggered a decrease in band gap energy. An increase in Mo doping from 1 to 2 wt % caused a notable red shift of the absorption edge. A red shift is generally beneficial to the photo degradation performance of TiO₂ nanoparticles, by inserting more valence electrons which can easily be turned into free charge-carriers by photons. Mo doping is reported to introduce a donor level under the conduction band of TiO₂, thereby reveals a narrower band gap [217].

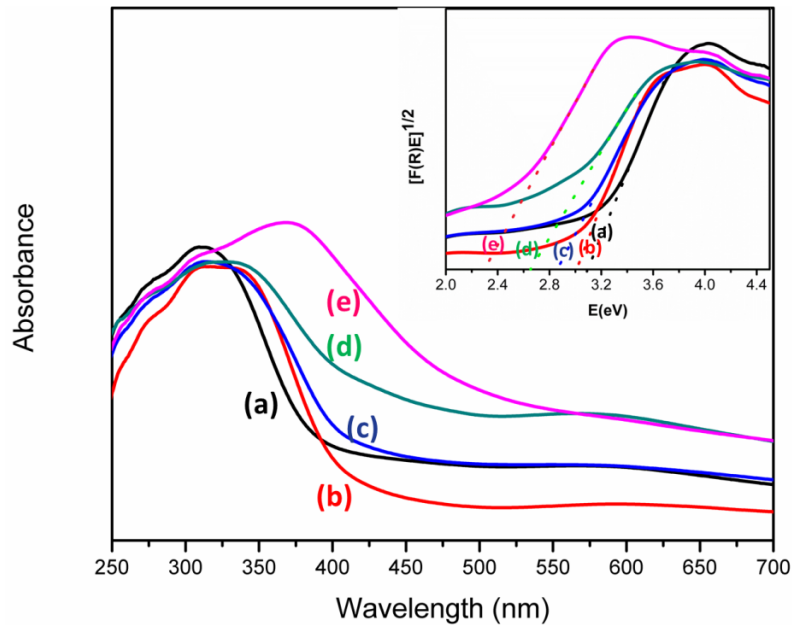


Figure 6.7 UV-visible absorption spectra and Kubelka-Munk transformed band gaps of samples (a) Mo0Fe0, (b) Mo1Fe0, (c) Mo2Fe0, (d) Mo2Fe0.5, and (e) Mo2Fe1.

Table 6.4 MB degradation rate after 90 min UV illumination, and band gaps as determined by using the Kubelka-Munk transformation of absorption data.

Sample Code	C/C ₀	Band Gap (eV)
MoFe0	0.48	3.09
Mo1Fe0	0.07	3.01
Mo2Fe0	0.46	2.86
Mo2Fe0.5	0.01	2.65
Mo2Fe1	0.75	2.30

Oxide formation of Mo may also play a significant role in decreasing band gap establishing a heterojunction similar with the case of anatase and rutile mixtures. Fe co-doping to the Mo doped sample offers a larger shift of the optical band gap values towards lower energies based on the amount of doped ion. However, band gap energy reduction is highest in sample Mo2Fe1. A probable reason for the lower band gap energy is the heterojunction between the crystalline MoO₃ regions and TiO₂ by increasing Fe doping.

MB degradation rate with respect to UV exposure duration and absorbance at the wavelength of 664 nm of the powders are depicted in Figure 6.8 (a). Values for the MB degradation rates of powders after 90 min exposure is given in Figure 6.8 (b). All un-doped, mono-doped and co-doped powders showed photocatalytic degradation ability. It is noted that washing the samples with DI water and sonication is very important for photoactivity. During experiments, it is clearly observed that without effectively washing the surface of the powders, MB molecules did not adsorb to the surface probably because of the presence of NO_x species on the surface. The NO_x species are considered to cause a hydrophobic surface. XPS analysis showed that, NO_x species are still on the surface of powders although they are washed by using ultrasonic cleaner. This finding is important for low MB degradation of powders synthesized by using HNO₃ catalyzer as mentioned in Chapter 4.

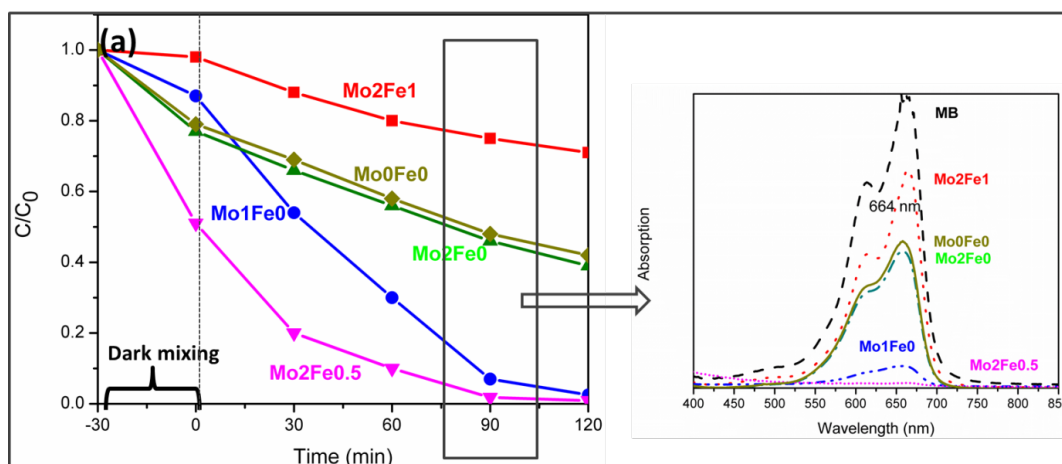


Figure 6.8 Variation of MB degradation rate with respect to UV exposure time and absorption curves of samples after 90 min UV exposure.

Sample Mo0Fe0 has considerable degradation ability. Much more activity is expected for sample Mo0Fe0 due to the synergistic effect of binary phase content, large surface area for MB adsorption, and the scattering effect of the 3D mesoporous structure built by 1D blocks, which provides benefiting from a large spectrum of light. However, highly oxidation atmosphere, lower crystallinity of this powder, NO_x species adsorbed at the surface and core shell growth of binary phases inhibited photoactivity. Mo doping into the structure increased photoactivity significantly, likely due to the increase in crystallinity, and the introduction of localized states and new donor levels into the forbidden band of TiO_2 , this may shift the absorption edge to enhance the photocatalytic activity. More doping of Mo increased photocatalytic activity further. After 90 min UV illumination, 44% of the dye molecules were still in the solution. A 0.5 wt % Fe doping along with 2 wt % Mo doping exhibited the best photocatalytic performance. In this powder, MB degradation was more than 99% after 120 min UV illumination. Besides the co-doping effect, amorphous oxide regions created by inserting a different type of dopant to the structure provide high photo degradation. Likewise, in dark, high adsorption was achieved by this sample as seen in Figure 6.8 (a). Fewer Fe atoms were detected by XPS analysis as compared to ICP and EDS analyses. This is a result of the core shell structure of oxidized Fe

and TiO₂. A core shell structure achieved by Fe insertion into the system might cause an increase in photocatalytic activity.

The interfacial charge-transfer process in a core shell structure of α -Fe₂O₃ and TiO₂ could be a driving force for enhanced photoactivity [218]. The degradation rate does not follow a linear trend, likely due to the high absorbance of MB molecules at the surface, which slows down surface-dye interactions, until all dyes on the active sites have been removed. The amount of degradation in the rutile phase is an achievement as this phase is commonly known as having relatively weak photocatalytic properties. Increasing the amount of Fe dopant had a negative impact on photoactivity due to the crystalline MoO₃ formation caused by removing more Mo atoms outside of the bulk as outlined by the HRTEM study. The decrease in absorption of MB molecules for the sample Mo2Fe1 shows that crystalline MoO₃ formation does not have the same affinity to MB molecules that amorphous oxides have. The lower band gap energies, resulting from discontinuity in band levels caused by extra dopants and the improper heterojunctions formed by oxidized Mo on the surface and/or oxidized Fe at the core, may cause recombination sites that have a negative effect on photoactivity [222]. MoO₃ has higher valence band (VB) potential than that of the potential of E(O₂/H₂O) (1.23 V vs NHE), E(*OH/OH⁻) (2.38 V vs NHE) and E(*OH/H₂O) (2.27 V vs NHE), which reduces the oxidation ability of photo generated holes and due to increasing amount of oxide structure on the surface photo generated electrons might not reach to the surface. Thus, photocatalytic activity is decreased to lowest value in sample Mo2Fe1 [223].

CHAPTER 7

RESULTS AND DISCUSSION: APPLICATION of TiO₂ NANOSTRUCTURES in DSSC

7.1 General

The aim of this study is to apply selected powders synthesized using hydrothermal method via acidic and basic catalyzer on DSSC photoanode in order to understand the effect of separately and collaboration of powders as bilayer in different crystal structure and morphology. Composite films were already studied intensely during the last few years and reported to become effective for enhanced efficiencies of DSSCs as reviewed in the literature part. However, there are still open doors in the field. In this study, 0D powders in 3 different crystal structure which were synthesized using acid assisted hydrothermal method, 1D and 2D powders in H-titanate form (consisting flakes and ribbons) synthesized using base assisted hydrothermal method and 3D powders in rutile crystal structure and synthesized using strong HNO₃ assisted hydrothermal method were applied separately and as composed with each other to form the semiconductor component of DSSC. Every powder has employed for different duties in the system to yield better performance from the cell. Powders are applied in the paste form according to the procedure explained carefully in Chapter 3. Depositing and sintering procedures were also explained in Chapter 3. Photoanodes were characterized using profilometer, UV-Vis spectrophotometer, XRD and FESEM. Photovoltaic and EIS measurements were done according to the procedure explained in Chapter 3.

7.2 Photoanode characterization

7.2.1 Thickness of TiO₂ films and dye loading

Figure 7.1 shows the thickness profile of sintered anodes prepared by using pastes PN846, P1-2D, PN843 and bilayer composite PHN843-PHN843 after sintering. Single layer coating of PN846 causes accumulation of paste on the edges of the scotch as seen in Figure 7.1 (a). The film thickness varies between 9 and 11 μm among the piled up regions. When pastes PN846 and PHN843 were coated in double layer as one onto another, the height difference between the edges and inside of the paste decreased considerably as seen in Figure 7.1 (b). The noise i.e., the surface roughness, increased by extra layers as compared to single layer coating. However, this noise is probably due to morphology of paste PHN843. When paste P1-2D, consisting of a mixture of 1D and 2D nano particles, were coated in single layer, coating thickness decreased slightly as seen in Figure 7.1 (c). The highest thickness inside the pile up region was measured 10 μm . In addition, a large micro crack was detected on the film, which arrives to FTO glass as seen in Figure 7.1 (c). Surface of paste P1-2D is rougher than that of paste PN846 probably due to nearly micrometer long ribbons. Profile of photoanode composed of paste PHN843 in single layer is shown in Figure 7.1 (d). The coating thickness of the film inside the piled up region in paste PHN843 changes quite roughly as compared to the coatings obtained when pastes PN846 and P1-2D are used. The ununiformed in film thickness is noted again due to the morphology of powders. Deep crack formation was not observed for this sample. The noise seen in bi-layer coating in Figure 7.1 (b) was not observed when the paste was coated as a single layer. The thickness of the pastes as measured using surface profilometer were listed in Table 7.1.

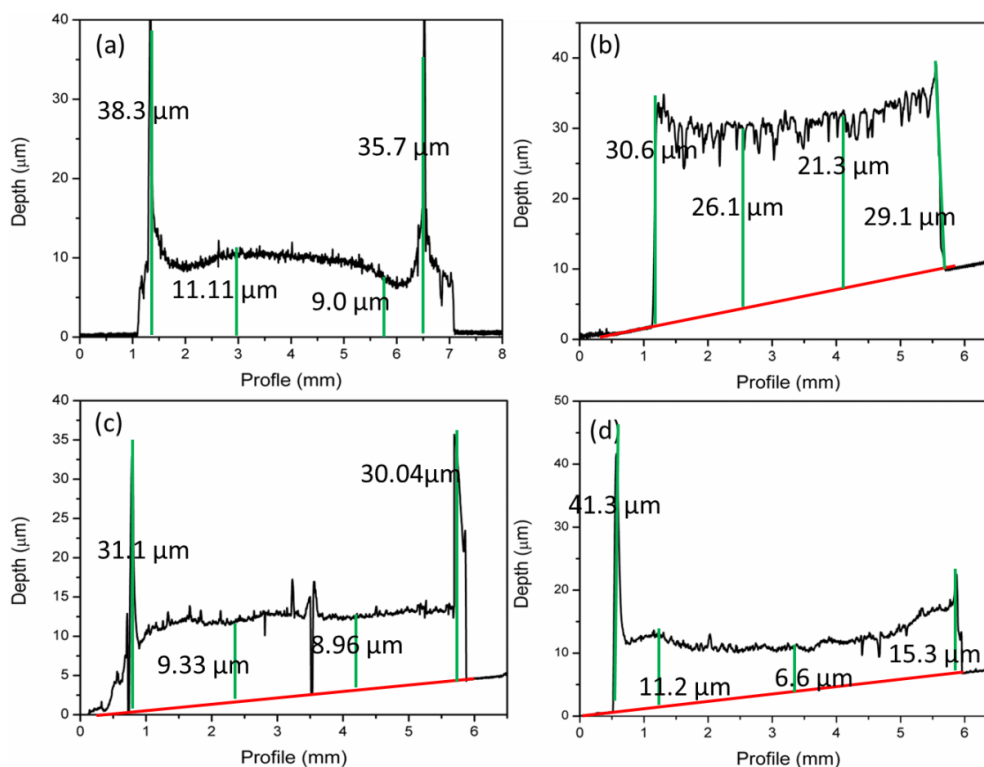


Figure 7.1 Thickness of coatings in different layers (a) single layer PN846, (b) bi-layer PN846 and PHN843, (c) single layer P1-2D, and (d) single layer PHN843.

Figure 7.2 (a) shows absorbance of N719 dye with respect to wavelength for various molarities (0.05, 0.1, and 0.2 mM). A graph showing the relation between dye molarity at 532 nm and absorbance is displayed in Figure 7.2 (b). The equation yielded from the fitted line shown in Figure 7.2 (b) is as follows;

$$y = 12.314x + 0.13$$

where, y is the absorbance at 532 nm and x is the molarity of N719 dye in ethanol solution. This equation was used to find the dye amount adsorbed to the TiO_2 surface in the working electrodes.

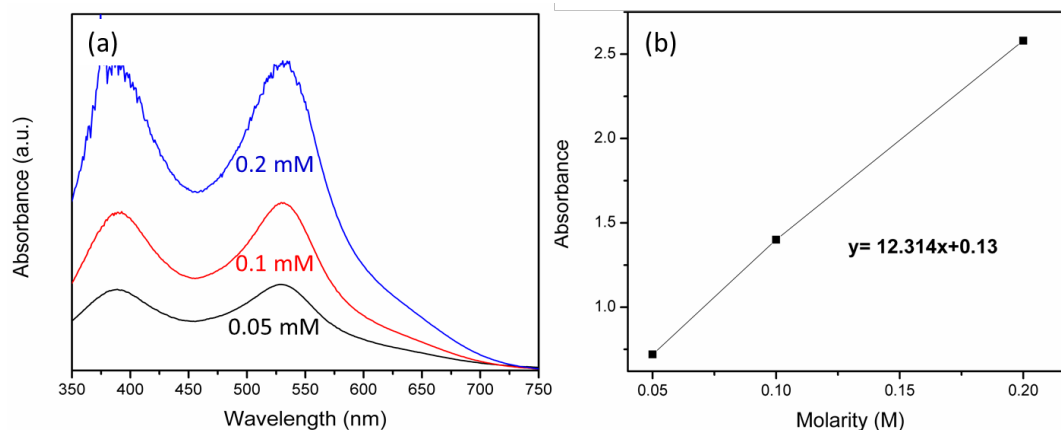


Figure 7.2 (a) Absorbance of dye solutions with different molarities in a particular range of light spectrum and (b) Change in absorbance at 532 nm of dye solutions with changing molarities.

The amounts of desorbed dye from photoanodes obtained by using pastes in single layer with a 0.64 cm^2 area are listed in Table 7.1. The highest absorption was obtained by paste PN846 that has the high reactive surface of anatase structure since the paste consists of predominantly anatase phase. Small particle size is another reason for the increase in the dye loading. The second dye loading was done by paste P1-2D. The high affinity of these structures to cationic dyes was mentioned in Chapter 4. Anatase content is also effective on high dye adsorption. Small particles around the 1D and 2D structures may also be another factor increasing dye loading. The third highest amount of dye was desorbed from paste PN116 probably due to high anatase content and low particle size. Even the powder consists of brookite and rutile as by product, dye loading is quite satisfactory. The next paste with fourth highest dye adsorption is paste PHN843. Although the paste consists of phase pure rutile, rather acceptable dye adsorption is probably due to mesoporous structure. Paste PN843 has lower dye adsorption on the surface although its relatively higher anatase content than paste PHN843. This may be a result of rutile structure of the surface which occurred by anatase-rutile surface transformation during hydrothermal synthesis, that could decrease the dye loading. Paste formed via Pechini method, paste PN846-p, has nearly similar dye molecules on its surface with paste PN846-t.

Table 7.1 Thickness and dye loading amounts of the cells.

Photoanode (0.64 cm ²)	Thickness (μm)	Desorbed dye (mol/cm ³)
PN116	13.57	1.23×10^{-4}
PN843	12.48	1.02×10^{-4}
PN846	10.59	1.45×10^{-4}
PN846-p	12.81	1.44×10^{-4}
PN846-t	11.82	1.49×10^{-4}
PHN843	12.46	1.08×10^{-4}
P1-2D	8.98	1.53×10^{-4}
PN846-PHN843	20.51	2.27×10^{-4}
PN846-PN843	21.07	2.45×10^{-4}
PN846-P1-2D	18.06	2.64×10^{-4}
PN846-PN116	22.47	2.48×10^{-4}
P1-2D-PHN843	19.64	2.48×10^{-4}

7.2.2 XRD analysis of TiO₂ films

XRD patterns of the sintered photoanodes coated with pastes in double layer are shown in Figure 7.3. Double layer coating was done for no detection of FTO peaks. The film thickness of double layer is about 20 μm . XRD penetration depth was assumed to be the same for pastes. All powders showed the characteristic peaks corresponding to the rutile (JCPDS 21-1276), brookite (JCPDS: 29-1360) and/or anatase (JCPDS 21-1272) phases. The percentages of the phases as calculated by using software and the formula given in Chapter 3 are tabulated in Table 7.2. FTO peaks were excluded during calculation of the phases.

XRD pattern of the sintered semiconductor layer formed using paste PN116, Figure 7.3 (a), revealed that the crystal structure of the powder consisting of anatase, rutile and brookite phases did not change after sintering. However, brookite share decreased slightly while rutile share increased. Brookite phase transformed partially to rutile during sintering at 500 °C due to small particle size and metastability of brookite phase at this temperature. FWHM of anatase (101) peak decreased after sintering as shown in Table 7.2.

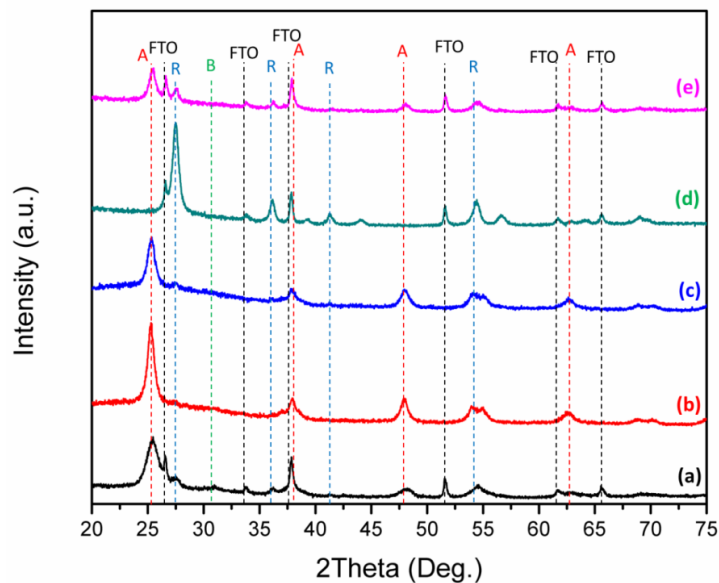


Figure 7.3 XRD patterns of semiconductor layers sintered at 500 °C (a) PN116, (b) P1-2D, (c) PN846, (d) PHN843, and (e) PN843.

Table 7.2 Crystal structure, weight percentages of phases and crystallite size.

Paste	Crystal Phase (wt %)			Change in FWHM (%)	
	Anatase	Rutile	Brookite	Anatase	Rutile
N116	85	10	5	20	NC
N846	96	4	-	24	-
N843	71	29	-	11	<1
HN843	>99	-	-	-	<1
N1-2D	>99	-	-	NC	-

*NC: Not calculated due to low crystallinity and/or overlapping.

FTO peaks were detected in this powder probably due to deformation on the surface of the film. Figure 7.3 (b) shows the XRD pattern of the semiconductor layer obtained using paste P1-2D. The anatase formation is obvious with phase transformation from titanate. The absence of titanate peaks in the pattern proves that the titanate structure transformed to TiO₂ structures as explained in detail in Chapter 4. XRD pattern of paste PN846, Figure 7.3 (c), indicates that rutile (110) peak at 2θ of 27.2° evolves besides anatase in this paste after sintering. Rutile formation was not expected at 500 °C, but phase transformation took place due to

low crystallite size of anatase particles. FWHM of the peak decreased considerably, which is advantageous for sintering. XRD pattern of the semiconductor layer obtained from paste PHN843 is depicted in Figure 7.3 (d). The film consists of solely rutile phase. FTO peak seen in this pattern was probably inhomogeneous film thickness and/or deformation on the film. The (211) plane intensity decreased, which is the highest intensity in powder HN846 as shown in Figure 4.4. The change of peak intensity infers morphological discrepancies in the powder at the paste after processing. FWHM does not change after sintering signifying that 500 °C is not an appropriate temperature for sintering of rutile particles. Figure 7.3 (e) shows the XRD pattern of the semiconductor film composed of paste PN843. The (211) plane intensity decreased again after processing of this paste, which is a sign of morphological transformation. Anatase share increased as compared to paste N843 due to further crystallization of the residual amorphous powder during sintering, which probably did not crystallize completely after hydrothermal process. FWHM of rutile phase did not change though. The change in FWHM of anatase (101) peak was lower than paste PN846 probably a result of anatase-rutile surface transformation that limits sintering of anatase particles. FTO peaks observed in this pattern are considered to occur due to analogous reasons with the previous pastes.

7.2.3 FESEM analysis

Figure 7.4 shows the FESEM images of the film prepared using paste PN846. Figure 7.4 (a) shows the cross section image of the paste produced by Pechini method. Thickness of the film changes between 10.31 and 13.33 μm in this region. Deep flaws formed through the FTO, when the photoanode was sintered according to the profile given in Chapter 3, as shown in Figure 7.4 (b). Tendency of the film to shrink is one of the reasons for the formation of the flaws. Shrinkage occurs due to inefficient viscosity of the paste that has a profound influence on the smoothness of the surface.

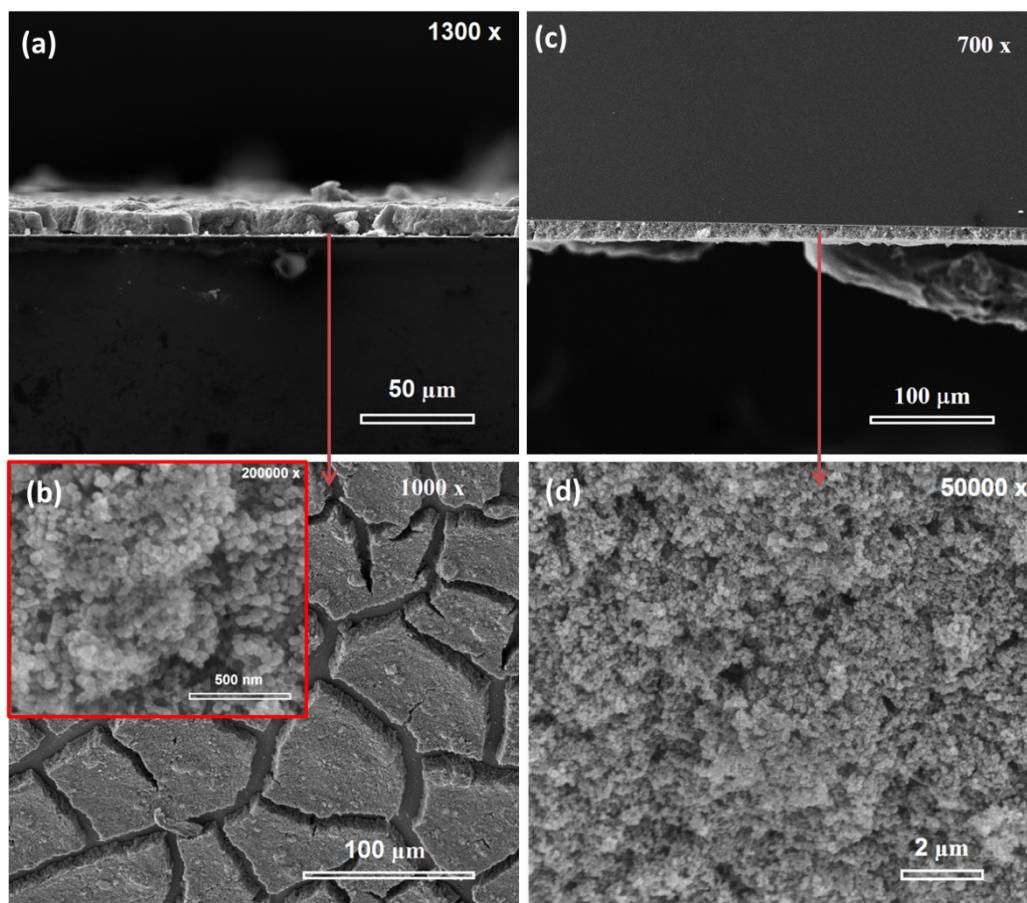


Figure 7.4 FESEM images of (a) paste PN846 prepared by using Pechini method, (b) Surface of the film, (c) paste PN846 prepared by Grätzel approach, (d) surface of the film.

The inset image shown in Figure 7.4 (b) is an image of the cross section of the same film with higher magnification. Porosities are seen easily in the image. Powders agglomerated and thus large pores formed. Figure 7.4 (c) shows the film produced by paste PN846 that was formed according to Grätzel's formula for screen printing deposition method. The arrays separated by deep flakes were not seen in this film. The thickness of the film varied between 12.04 and 16.20 μm . The morphology of the surface of the film shown in Figure 7.4 (d). illustrates that the pore size somewhat decreased but not as much as expected. The sintering of the nanoparticles seems efficient for electron transport if the pores are overlooked.

Figure 7.5 shows the semiconductor layer obtained by paste PN843. The thickness of the film is nearly 13 μm . Flower structure was not noticed both in cross section and in surface examinations of the paste. Structure formed by small nanoparticles that were oriented in one direction partially. Large pores existing in the structure formed probably during binder removal stage in sintering.

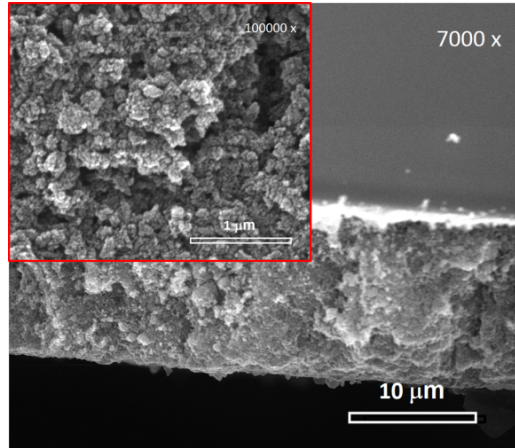


Figure 7.5 Cross section of semiconductor layer obtained by PN843 inset image surface morphology of coating.

Figure 7.6 (a) shows the cross section of the film formed using a mixture of 1D and 2D powders via Grätzel's approach. The thickness of the film is not homogenous and smooth as shown in Figure 7.6 (a). The morphology of the film depicted in Figure 7.6 (b) shows that several micrometers long one-dimensional particles became smaller and decreased to nearly 500 nm. The deformation of 1D structure by shortening is probably due to grinding of powder for several minutes to form a paste. Existence of deformed particles is beneficial because shorter nanoribbons are good in terms of surface area and also detrimental due to lack of transport among the particles, which will cause recombination at the end of the grain. The untransformed particles distributed among the 1D structures transformed to anatase phase by heat treatment at 500 $^{\circ}\text{C}$. These nanoparticles were deliberately left in the structure since they are useful for dye adsorption by increasing the surface area.

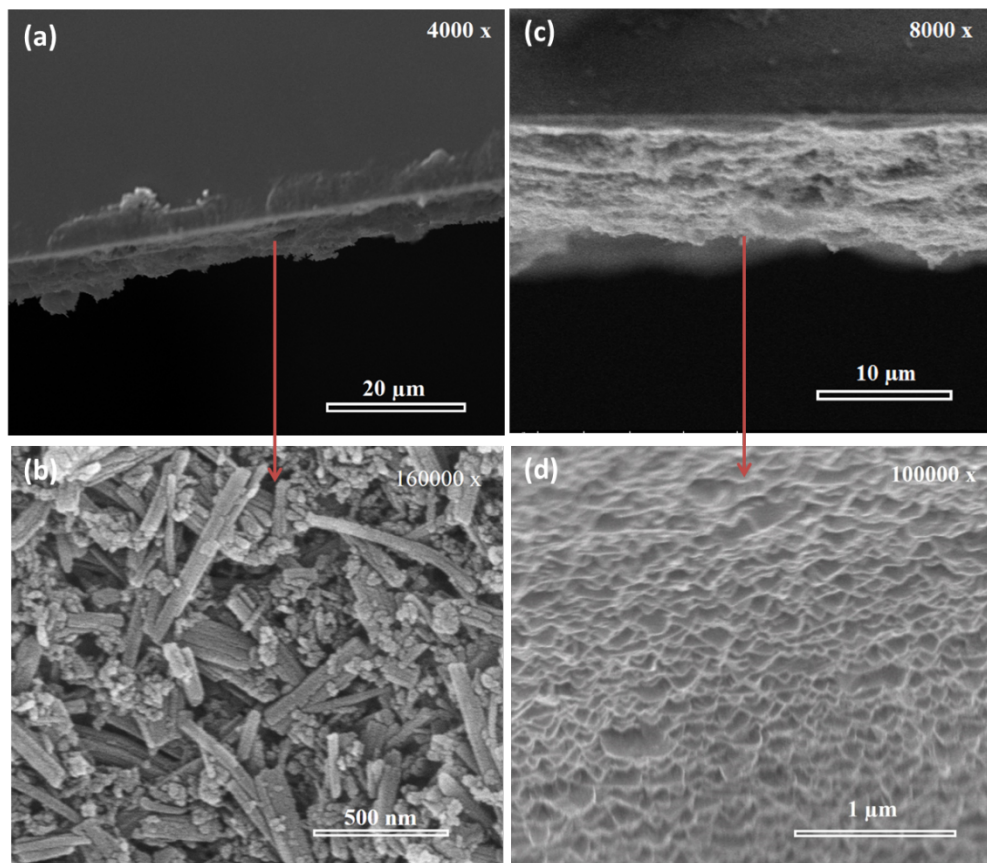


Figure 7.6 FESEM images taken from two different regions (a) cross section of paste P1-2D, (b) morphology of P1-2D, (c) cross section of paste P1-2D, (d) morphology of paste P1-2D.

Figure 7.6 (c) shows the cross section of semiconductor film formed by 2D sheets in paste P1-2D via Grätzel's approach. Film thickness is not smooth in this sample though. Large pores between layers are seen clearly. The adhesion of film seems better as compared to the film formed from 1D powders. The morphology of the powder shows continuity throughout the surface as indicated in Figure 7.6 (d) The very well sintering of the particles is advantageous for charge transport through the FTO glass. Uniform structure implies that 2D sheets were not damaged by grinding and mixing.

Figure 7.7 shows the FESEM images of pastes PN116, PHN843, and PN846. Figure 7.7 (a) shows the semiconductor film made of paste PN116 via Grätzel's

approach. As seen in the image, there is some porosity in the structure. As compared to semiconductor film obtained by pastes PN846 or P1-2D, pores are considerably smaller. Sintering of particles in the film seems completed. Figure 7.7 (b) shows the image of the semiconductor film made of paste PHN843 via Grätzel's approach. The original powder morphology demolished. The pores are obvious. Especially, cross section view shows large pores inside the structure. Porous structure was noted for this paste previously. However, morphological analysis of anodes obtained by pastes PHN843, PN843 and P1-2D shows that paste preparation is not a suitable method for deposition of 1D and 3D structures.

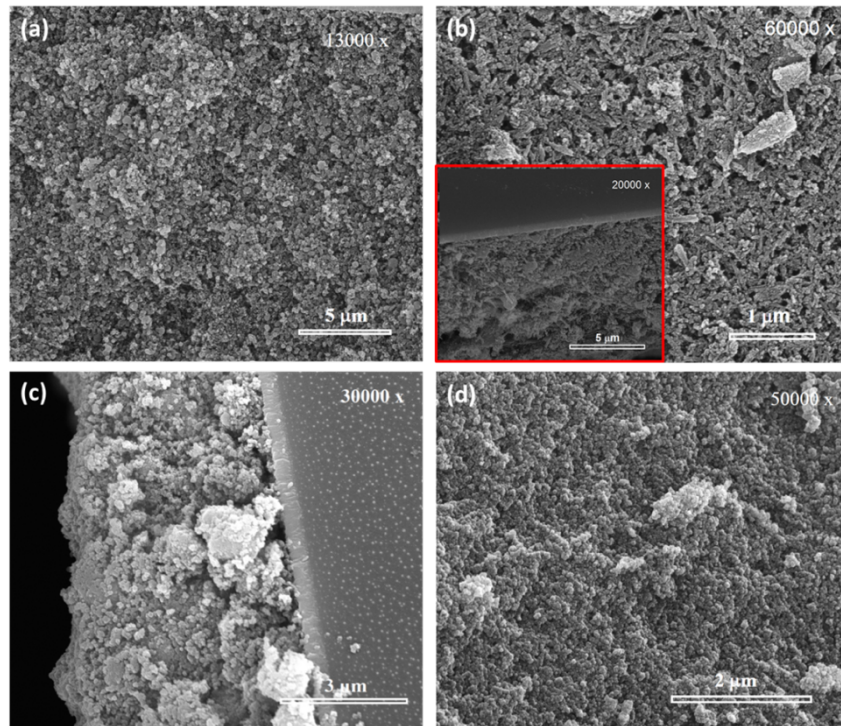


Figure 7.7 FESEM images of (a) PN116 (b) PHN843 inset image cross section view of the coating (c) cross section of PN116 (d) PN846-p pechini with decreased viscosity.

After morphological analysis it is realized that instead of deposition by preparing paste, these kind of structures are better deposited directly onto TCO substrate. The deformation of particles during grinding of paste is essential for pastes with

well distributed nanoparticles. Figure 7.7 (c) shows the cross section view of semiconductor film obtained by using paste PN116. The powders were highly agglomerated probably due to inefficient separation during mixing of paste for alcohol evaporation. Agglomeration also inhibits adhesion to the FTO surface. Figure 7.7 (d) shows the morphology of paste prepared using PN846P powder via Pechini method. Viscosity of the paste decreased by adding 2 more drops of ethylene glycol. Deposition of the film produced via Pechini method was easier as compared to that produced via Grätzel's approach. As seen in the image, porosity decreased considerably. Sintering process of particles seems well enough for charge transport. Use of TTIP as additive is considered to be very effective for Pechini method. Pechini method may also be preferred due to low cost of starting materials as compared to Grätzel's approach.

The FESEM images of TiCl_4 treated paste PN846 prepared via Grätzel's approach is shown in Figure 7.8. As seen clearly in Figure 7.8 (a), amount of pores decreased considerably after TiCl_4 treatment. Sintering seems better in this sample as compared to the untreated one. Furthermore, the thickness of the paste is quite smooth as depicted in Figure 7.4 (d). Thickness is also quite smooth as depicted in Figure 7.8 (c). TiCl_4 treatment was reported to be highly efficient for nanoparticle interaction [11]. However, very large cracks formed in the paste as indicated in Figure 7.8 (d). The cracks could not be eliminated ever by TiCl_4 treatment. Any crack formation was not observed with Pechini method with decreased viscosity. In this study, TTIP post treatment was not applied even though TTIP post treatment could be more efficient than TiCl_4 post treatment.

Figure 7.9 shows the FESEM images of binary films applied on FTO glass. As seen in Figure 7.9 (a) layer adhesion to FTO glass did not take place completely and pastes were peeled from FTO and each other when 0D (paste PN846) and 1D powders (paste P1-2D) were used together. Low adhesion to FTO in 0D and 0D pairs formed using pastes PN846 and PN116 was shown in Figure 7.9 (b) The layers also did not become integrated. The bi-layer morphology of paste PN846-PN843 has the best integration to each other and adhesion to FTO glass.

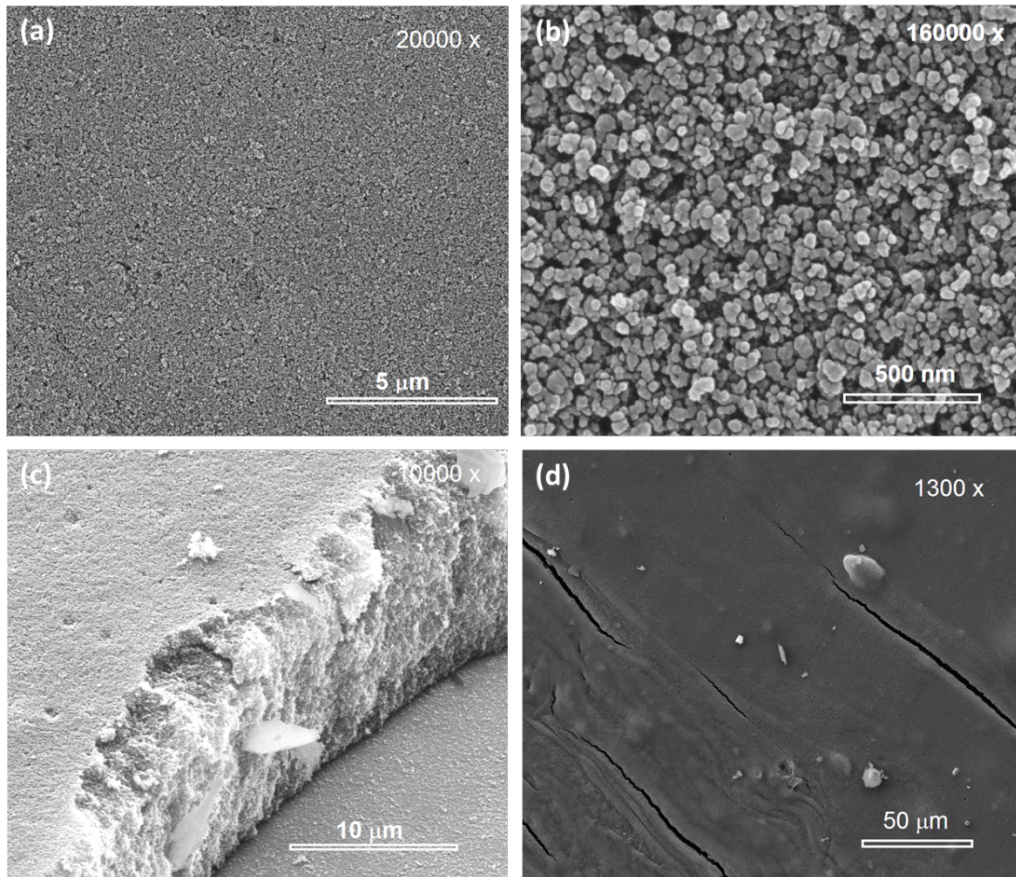


Figure 7.8 FESEM images of PN846-t (a) general surface view, (b) High magnification surface morphology, (c) thickness of paste with cross section view, and (d) low magnification view of the surface.

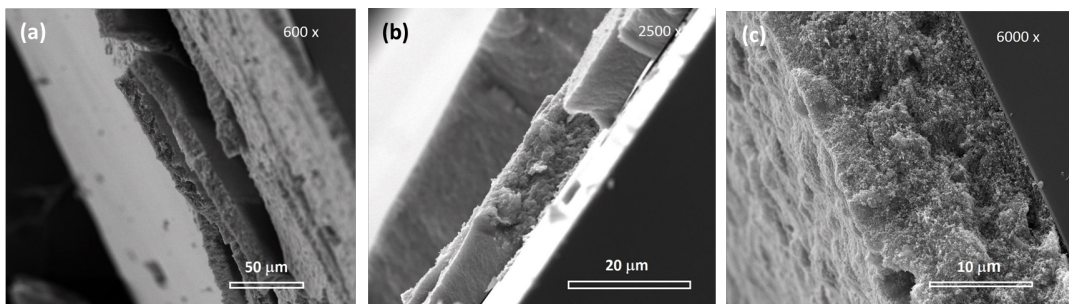


Figure 7.9 Bi-layer photoanodes (a) PN846-P1-2D, (b) PN846-PN116 (c) N846-PN843.

7.2.4 UV-vis spectrophotometer

Figure 7.10 shows transmission spectra of the semiconductor single layers formed by using pastes prepared via Grätzel's approach. The lowest transmission obtained by paste PHN843 as depicted in Figure 7.10 (a) is probably due to scattering effect inside the structure by rutile crystals. Larger rod-like grains in this paste may also cause low transmission of light. Moreover, rutile crystals in this paste are responsible for low transmission due to high refractive index of this polymorph of TiO_2 [15]. Paste PN843 shows higher transmission probably due to small anatase grains inside the structure. See Figure 7.10 (b). Lower transmission as compared to other samples is probably due to scattering ability of rutile crystals inside the composite structure. Similar effect is observed in paste PHN843. As seen in Figure 7.10 (c) and (d), pastes PN116 and PN846 have similar transmission spectra although paste PN846 contains more anatase phase than paste PN116. Higher rutile content of paste PN116 is expected to cause more scattering and lower transmission. However, brookite content of paste N116 may increase transmission of light inside the structure. The semiconductor layer obtained by paste PN846 have higher transmittance than paste PN116 at lower wavelength part of the spectrum due probably to higher valance maximum of anatase phase. Also lower grain size of anatase in paste PN116 may be effective on comparable transmission.

Semiconductor layer formed by using paste P1-2D was analyzed 4 times by rotating the glass in device holder due to composition of different morphologies. Minimum and maximum transmission was shown in Figure 7.10 (e) and (f), respectively. Probably sheet like part of the film showed highest transmission due to low thickness of the structure. Lowest transmission was yielded by 1D morphologies that helps scattering. Although XRD analysis did not detect $\text{TiO}_2(\text{B})$, there might be some amount of this polymorph in the powder due to slightly higher band gap value (3.31 eV after calcination) of the powder as shown in Table 4.2. The high transmission of 1D part as compared to paste PHN843 is probably crystal structure difference. In addition, small grains among the 1D particles might be effective on higher transmission.

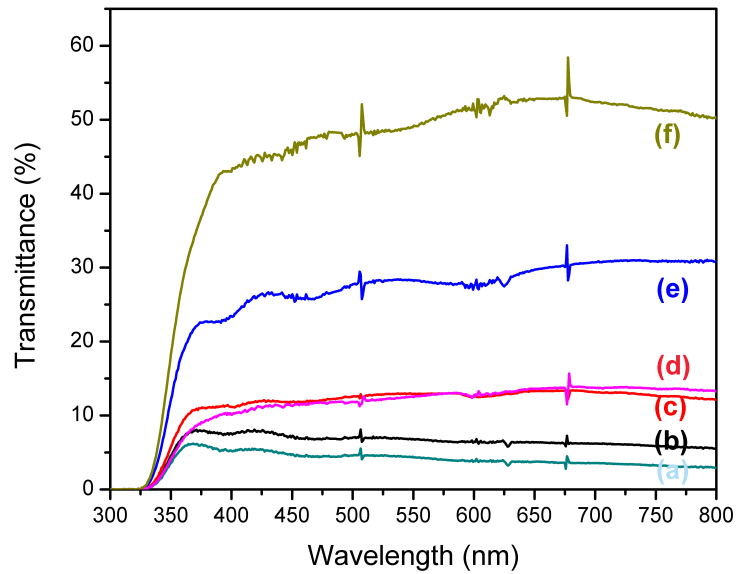


Figure 7.10 Transmission spectra of single layered pastes (a) PHN843, (b) PN843, (c) PN846, (d) PN116, (e) P1D and (f) P2D.

7.3 Photovoltaic and EIS measurements

Figure 7.11 shows the J-V curves of seven different pastes. The data obtained by I-V curves was also tabulated in Table 7.3.

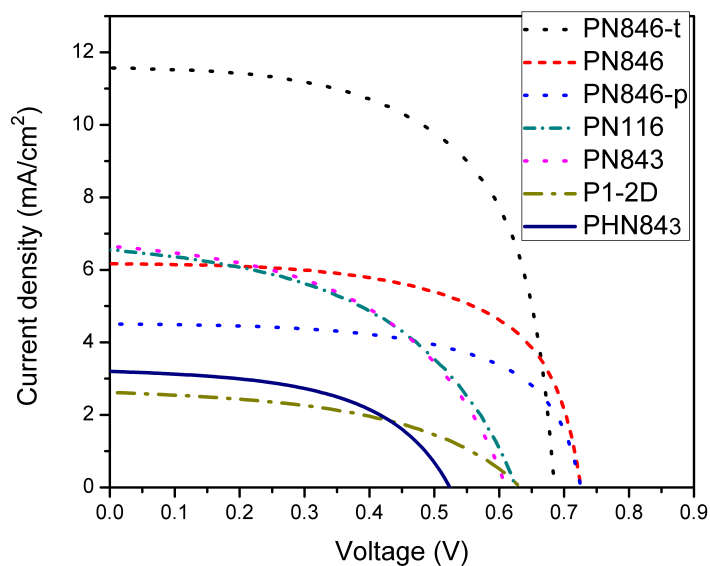


Figure 7.11 J-V curves of DSSCs with single layer photoanode.

Table 7.3 Data obtained by solar simulator measurements for 1 cm² exposed area.

Paste	V _{oc} (V)	J _{sc} (mA/cm ²)	V _{max} (V)	I _{max} (mA)	FF (%)	η (%)
PN846	0.71	6.10	0.64	4.48	66	2.86
PN846-t	0.68	11.51	0.54	8.95	62	4.85
PN846-p	0.71	4.49	0.61	3.31	63	2.00
PN843	0.61	6.65	0.41	4.42	45	1.82
PN116	0.62	6.64	0.42	4.56	47	1.92
P1-2D	0.63	2.62	0.48	1.63	47	0.78
PHN843	0.52	3.21	0.37	2.39	52	0.88

The lowest V_{oc} was obtained by PHN843 as shown in Figure 7.11. Shunt resistance seems low while series resistance is high. High series resistance is probably caused by grain boundaries in polycrystalline 1D rod like structures. Because the conduction band of anatase is 0.2 V more negative than that of rutile, a larger maximum photovoltage could be obtained on anatase than on rutile if the same redox mediator is employed. Although rutile structure is reported to have comparable V_{oc} with anatase structure by architecting the morphology [9], V_{oc} is the lowest among the seven cells made-up in this study. The low V_{oc} is probably due to rutile content and inefficient touch points of particles which decreases electron accumulation on Fermi band. The low I_{sc} is considered to be caused by low adhesion of film onto FTO, which results in dark current. Kambe and co-workers [224] declared that the diffusion coefficient of conduction band electrons in rutile is significantly smaller than that in anatase. P1-2D showed slightly lower current and higher voltage values as depicted in Figure 7.11 although its anatase crystal structure. Increasing series resistance is observed in this cell though. The 0 D nanoparticles around the 1 and 2 D nano particles may decrease the I_{sc} because of grain boundaries although larger amount of dye adsorption. However, anatase crystal structure let higher voltage compared to PHN843. Figure 7.11 shows the J-V performance of PN116. The current value increased compared to P1-2D while V_{oc} is similar. The addition of rutile is reported to significantly enhance the photocurrent and overall solar conversion efficiency of anatase photoanodes due to synergistic effect. Shen et al. [225] reported 7.24 % efficiency using anatase, C-doped rutile, and C-doped brookite composites. When the cell is compared to paste

PN843 shown in Figure 7.11, brookite phase does not have an important effect on the performance that PN843 have similar results except slight increase of I_{sc} and decrease of V_{oc} . PN843 showed the lowest FF among the cells which shows that there is much between the maximum values and theoretical values. As it is seen clearly the highest J_{sc} and V_{oc} were obtained by the pastes including high amount of anatase nano particles. This is not a surprising fact that anatase nano particles were mentioned as a superior charge carrier scaffold earlier. However, paste formation method is important though. When a comparison was done between three different pastes including same powder which were gathered together by Grätzel's method, Pechini method and $TiCl_4$ treated Grätzel paste, the highest current were obtained by PN846-t which was treated by $TiCl_4$ before and after paste application as shown in Figure 7.11. $TiCl_4$ treatment is reported very important for V_{oc} due to positive charging of surface by this treatment [226]. However, V_{oc} of treated paste was lower compared to untreated paste which is probably due to agglomeration of particles in the treatment solution due to high activity of $TiCl_4$. Grätzel's paste showed higher performance compared to Pechini paste although pechini paste was smoother and easier applicable. Both pechini and Grätzel pastes showed higher V_{oc} compared to treated cell. In DSSCs, an increase in V_{oc} at a given charge density implies an upward shift of Fermi level [227]. Large anatase content of these pastes resulted in highest voltage. This is probably due to agglomeration of powders which is a result of shrinkage caused by tension by inappropriate amount of viscosity of the paste. Figure 7.12 shows the J-V curves of DSSCs built by bilayer photoanodes using composite pastes. Table 7.4 shows the data of the DSSCs as measured by a solar simulator per 1 cm^2 exposed area. The J-V curve of the DSSC built by bilayer pastes P1-2D and PHN843 composite is the lowest among the DSSCs built. FF calculated by J-V data revealed a low value for this cell. Low shunt resistance and high sheet resistance is two probable result for the low FF. The low V_{oc} may be due to high rutile content of the composite. In addition, rod structure on top of the nano particles that have low interaction might favor traps for electron recombination. Low J_{sc} is considered

a result of high rutile content and low interaction between the particles in spite of the high light scattering ability of rutile phase.

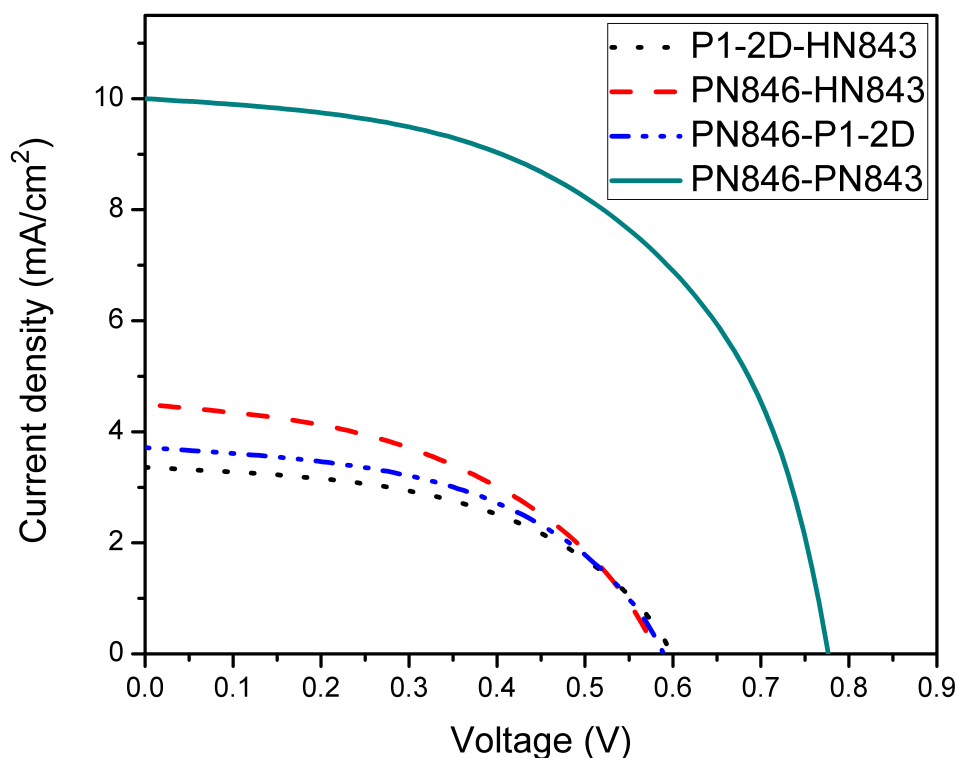


Figure 7.12 J-V curves of DSSCs built by composite pastes.

The J-V curve of the DSSC built by pastes N846-P1-2D composite yielded the lowest FF factor. Indeed, sheet resistance is not satisfied for the cell. High anatase content might be effective on the relatively high current. V_{oc} decreased as compared to the previous cell probably due to low interaction between the particles that resulted in trap sites. The J-V curve of the DSSC built by pastes PN846 and PHN843 gave low FF probably due to high sheet resistance in this cell. Photocurrent increased as compared to the previous cells. The increase in photocurrent is considered a result of high scattering ability of the light inside the rutile structure.

Table 7.4 Data of cells built by paste composites obtained by solar simulator measurements for 1 cm² exposed area.

Composites	V _{oc} (V)	J _{sc} mA(cm ²)	V _{max} (V)	I _{max} (mA)	FF (%)	η (%)
PN846-PHN843	0.58	4.58	0.47	2.65	48	1.24
PN846-P1-2D	0.63	3.71	0.48	2.29	47	1.09
PN846-PN843	0.78	9.72	0.56	7.61	56	4.26
P1-2D-PHN843	0.60	3.36	0.41	2.41	49	0.99

Despite the low interaction between the layers, V_{oc} and J_{sc} is satisfactory. In the system, anatase layer is considered to work as active layer for energy conversion and rutile top layer works as scattering layer. Figure 7.12 shows the J-V curve of the DSSC built using PN846 and PN843 paste composite. The highest FF reveals lowest sheet and shunt resistances. Also V_{oc} of the bi-layered cell is highest among all the cells assembled. The highest V_{oc} is considered to be a result of higher electron accumulation in the Fermi layer of anatase particles with the aid of rutile top layer which might increase light harvesting by scattering. The surprising part of the curve is the high current obtained by the cell. The top layer which is a mixture of anatase and rutile and the down layer which has an anatase domination with small amount of rutile showed the highest performance in terms of low recombination, high scattering of light inside the structure and high diffusion of charge carriers inside the semiconductor layer among the bi-layer structures. Synergistic effect of anatase and rutile binary phase may also be effective on the highest performance.

Figure 7.13 shows EIS measurement results of DSSCs built by different pastes as photoanode and parameters revealed by fitting the data are tabulated in Table 7.5. The sheet resistances obtained by EIS measurements changes between 20 and 50 Ω as shown in Table 7.5. The lowest sheet resistance 20.71 Ω obtained by PN846-t includes FTO resistance and 50 μm spacer which increases the resistance of electrolyte. The higher series resistances taken by other cells up to 49.22 Ω may be related to counter electrode and/or electrolyte. Both parts charge transport

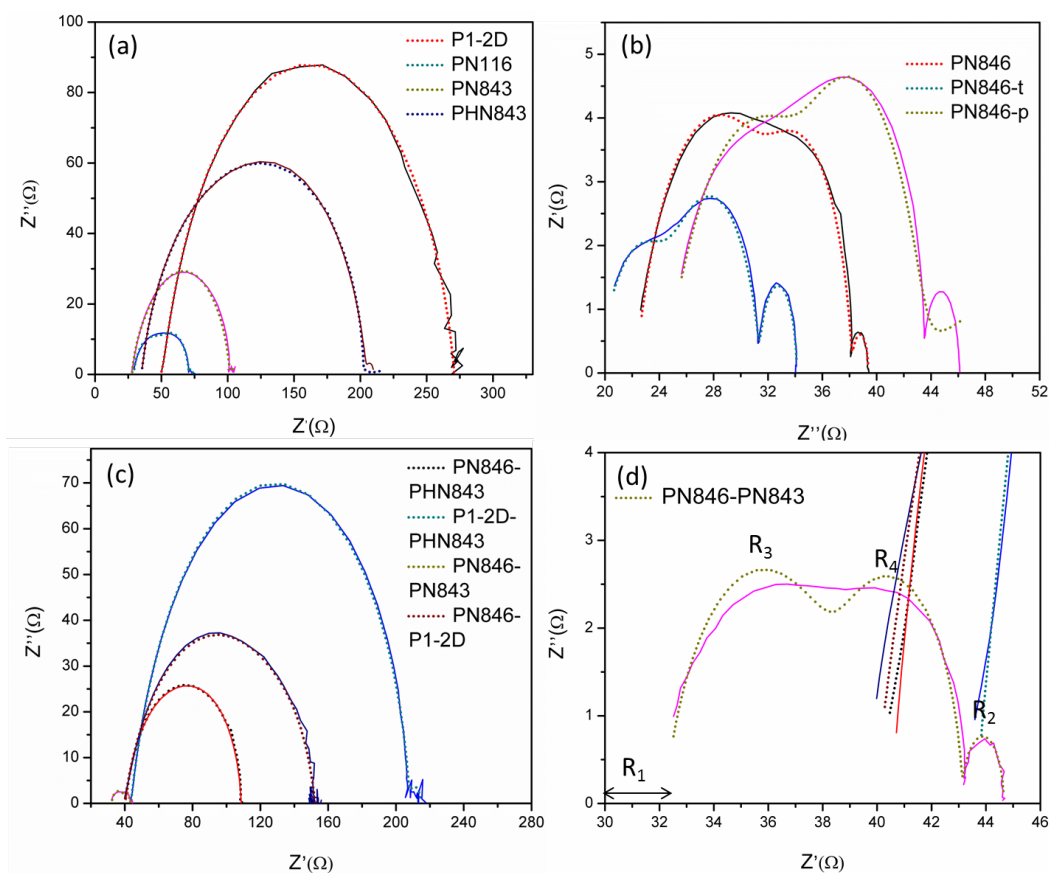


Figure 7.13 Nyquist plots of DSSCs built by different pastes (a) P1-2D, PN116, PN843, PHN843, (b) PN846, PN846-t, PN846-p, (c) PN846-PHN843, P1-2D-PHN843, PN86-PN843, PN846-P1-2D, (d) PN846-PN843 signal enlarged view (dots represent fitting curve while solid lines represent raw data).

Table 7.5 Fitted resistances for EIS measurements of electrodes.

Photoanode	R_1 (Ω)	R_2 (Ω)	R_3 (Ω)	R_4 (Ω)
P1-2D	49.22	4.2	48.03×10^3	216
PN116	29.08	21.74	3.015	19.92
PN843	27.96	3.99	23.15	50.67
PHN843	35.43	5.23	30.84	139
PN846	22.63	1.14	4.21	11.79
PN846-p	25.63	49.7×10^3	5.48	11.91
PN846-t	20.71	5.52	2.64	6.37
PN846-PHN843	40.47	46.64	13.7×10^2	21.60
PN846-PN843	32.52	1.49	3.84	7.11
PN846-P1-2D	40.28	101.5	9.67×10^{-6}	11.04
P1-2D-PHN843	43.59	18.91	6.40	145.6

ability depends on time due to several reasons such as decreasing activity of Pt after several hours, penetration of electrolyte. Thus, different series resistance might be related to these parameters that is consistent with I-V measurements. R_2 also varies in different cells although all the counter electrodes were prepared with similar procedure. This is considered to become a result of different preservation periods of cells. When R_3 and R_4 are examined, the highest R_3 and R_4 were revealed by P1-2D. Low current is probably due to low transportation of electron in the layer. The high R_4 also reveals low recombination between particle and electrolyte. One may think this low recombination as a benefit. However, low transportation effects current which decreases the cell efficiency. Although PN116 has low R_3 , relatively higher R_4 value leads low efficiency which makes sense when R_3 is assumed as resistance for recombination and R_4 as charge transfer. Both R_3 and R_4 are higher in PN846 probably due to agglomerations and large porosities in the structure. R_4 is quite high in PHN843 probably due to lack of touch point of particles. Rutile structure of the layer may also be a reason for low electron mobility.

Photoanodes formed by PN846 have the lowest resistances among single layer anodes. The lowest among the three cells which employed PN846 as semiconductor layer was revealed by PN846-t. Pechini paste has also very comparably small R_3 and R_4 although photovoltaic measurements revealed low current. However, as seen from the high R_2 , the impedance test was done 2 days later than photovoltaic measurements and while Pt resistance increased, R_3 and R_4 increased due to penetration of electrolyte. Charge transfer resistances of bi-layer structures are very high except PN846-PN843 which includes only nanoparticles in the morphology. PN846-P1-2D also have very low R_4 value. However low R_3 which is probably related to recombination of electrons at the TiO_2 -electrolyte interface causes low current and efficiency of the cell.

CHAPTER 8

CONCLUSIONS

8.1 Syntheses of one dimensional titanate and TiO₂ nanostructures

- Single phase Na_{2-x}H_xTi₃O₇.H₂O is obtained by amorphous TiO₂ precursor in the base assisted hydrothermal process. Calcined products synthesized by using amorphous TiO₂ as precursor consist of single anatase phase.
- Ribbon structure is exfoliated using P25 precursor while flakes are exfoliated in different shapes using anatase precursor.
- Both H and Na-titanate structures yield considerably higher adsorption of MB molecules as compared to calcined samples including different TiO₂ polymorphs. The best photocatalytic activity and superior adsorption are realized in the calcined product synthesized by using amorphous precursor.

8.2 Hydrothermal syntheses of TiO₂ nanostructures using acid catalyzer

- Anatase phase evolves dominantly with brookite and rutile phases using 1M acid catalyzer at various temperatures and durations during hydrothermal process. Anatase and rutile phases mostly evolve when 3 M acid catalyzer is used at various temperatures and durations. Phase pure rutile is realized using 8 M acid catalyzer.
- Using titanate seeds remotes >99 % rutile formation in the structure when 8M acid catalyzer is used during synthesis at 140 °C for 3 h.

- FESEM analysis revealed that as rutile share increases rod formation takes place in the morphology by surface transformation from anatase phase. Rod arrays resembling lotus flower formed through acid etching.

8.3 Mono-, co- and triple-doping of TiO₂ nanostructures with Mo, Fe and N

- N is doped into the system autogenously from HNO₃ in the co-doped powder with Mo and Fe. The final crystal structure is rutile in rod array morphology.
- Fe atoms is considered to settle down in the core of the structure serving as a nucleation seed while Mo oxidizes partially on the surface of particles during synthesis.
- In excess of 99% photo degradation of MB after 2 h of UV-illumination is obtained by triple-doped rutile structure.

8.4 Application of TiO₂ nanostructures in DSSC

- The highest dye adsorption is obtained using anatase 1D-2D mixed powders and lowest adsorption is obtained by rutile containing powders.
- FESEM analysis showed morphological variations in pastes prepared by using 1D and 3D powders are probably due to grinding step applied in the preparation of pastes.
- Among single layer DSSCs, the highest photovoltaic efficiency is obtained using anatase particle dominated paste as 4.86 % by TiCl₄ treatment.
- In bi-layer DSSCs, the highest photoactivity is obtained using anatase dominated down layer and anatase rutile mixture as top layer as 4.26 %.

CHAPTER 9

FUTURE WORKS

The following works are recommended to be done in future.

- Heat treatment of protonated titanate structures obtained by amorphous precursor should be examined carefully using Rietveld analysis in order to calculate the exact phase proportion of anatase and TiO_2 (B).
- Electronic properties of titanate structures should be examined using EIS for charge carrying media applications.
- It was observed that hetero-mixture of anatase-rutile-brookite structures in different ratios can be synthesized using HNO_3 catalyzed hydrothermal treatment. Photoactivity of this structure with respect to phases present should be investigated using Rietveld refinement.
- N doping without extra dopant should be examined in the powders synthesized by acid assisted hydrothermal process. Surface properties of the powders should be studied. The electronic behavior of the powders should be studied using EIS analysis.
- Effect of triple doping with Mo, N and Fe on the efficiency of DSSCs should be investigated.
- Epitaxial growth of nanoflowers synthesized using HNO_3 catalyzer should be conducted to decrease adsorption problems in the bi-layer photoanodes of DSSCs.

BIBLIOGRAPHY

- 1 O. Morton, "Solar energy: A new day dawning?: Silicon Valley sunrise," *Nature*, vol. 443, p. 19, 2006.
- 2 M. Grätzel, B. Oregan, "A low-cost, high-efficiency solar cell based on dye-sensitized colloidal TiO₂ films," *Nature*, vol. 353, p. 737, 1991.
- 3 K. Kakiage, Y. Aoyama, T. Yano, K. Oyaf, J.-I. Fujisawa, M. Hanaya, "Highly-efficient dye-sensitized solar cells with collaborative sensitization by silyl-anchor and carboxy-anchor dyes," *Chem. Commun.*, vol. 51, p. 15894, 2015.
- 4 S. Mathew, A. Yella, P. Gao, R. Humphry-Baker, B. F. E. Curchod, N. Ashari-Astani, I. Tavernelli, U. Rothlisberger, Md. K. Nazeeruddin, M. Grätzel, "Dye sensitized solar cells with 13 % efficiency achieved through the molecular engineering of porphyrin sensitizers," *Nature Chemistry*, vol. 6, p. 242, 2014.
- 5 D. Wei, "Dye Sensitized Solar Cells," *Int J Mol Sci.*, vol. 11, p. 1103, 2010.
- 6 C. H. Lee, S. W. Rhee, H. W. Choi, "Preparation of TiO₂ nanotube/nanoparticle composite particles and their applications in dye-sensitized solar cells," *Nanoscale Res Lett.*, vol. 7, p. 48, 2012.
- 7 N. A. Jadhav, P. K. Singh, H. W. Rhee, S. P. Pandey, B. Bhattacharya, "Effect of structure texture and morphology modulation on efficiency of dye sensitized solar cells," *Int. J. Electrochem. Sci.*, vol. 9, p. 5377, 2014.
- 8 L. Chu, Z. Qin, J. Yang, X. Li, "Anatase TiO₂ nanoparticles with exposed {001} facets for efficient dye-sensitized solar cells," *Sci. Rep.*, vol. 12143, 2015.
- 9 N.-G. Park, J. van de Lagemaat, A. J. Frank, "Comparison of dye-sensitized rutile-and anatase-based TiO₂ solar cells," *J. Phys. Chem. B*, vol. 104, p. 8989, 2000.
- 10 K. Basu, D. Benetti, H. Zhao, L. Jin, F. Vetrone, A. Vomiero, F. Rosei, "Enhanced photovoltaic properties in dye sensitized solar cells by surface treatment of SnO₂ photoanodes," *Sci. Rep.*, vol. 23312, 2016.
- 11 M. Ye, X. Wen, M. Wang, J. Iocozzia, N. Zhang, C. Lin, Z. Lin, "Recent advances in dye-sensitized solar cells: from photoanodes, sensitizers and electrolytes to counter electrodes," *Materials Today*, vol. 18, no. 3, p. 155, 2015.
- 12 J.-Y. Liao, B.-X. Lei, D.-B. Kuang, C.-Y. Su, "Tri-functional hierarchical TiO₂ spheres consisting of anatase nanorods and nanoparticles for high efficiency dye-sensitized solar cells," *Energy Environ. Sci.*, vol. 4, p. 4079, 2011.
- 13 W. Shao, F. Gu, C. Li, M. Lu, "Highly efficient dye-sensitized solar cells by using a mesostructured anatase TiO₂ electrode with high dye loading capacity," *Ind. Eng. Chem. Res.*, vol. 49, p. 9111, 2010.
- 14 Ji. Lin, Y.-U. Heo, A. Nattestad, Z. Sun, L. Wang, J. H. Kim, S. X. Dou, "3D hierarchical rutile TiO₂ and metal-free organic sensitizer producing dye-sensitized solar cells 8.6% conversion efficiency," *Sci. Rep.*, vol. 4, p. 5769, 2014.

- 15 S. M. Gupta, M. Tripathi "A review of TiO₂ nanoparticles," *Chinese Sci Bull*, vol. 56, p. 1639, 2011.
- 16 A. Di Paola, M. Bellardita, L. Palmisano, "Brookite, the least known TiO₂ photocatalyst," *Catalysts*, vol. 3, p. 36, 2013.
- 17 Z. Lin, J. Wang, *Low-cost Nanomaterials: Toward Greener and More Efficient Energy Applications*, London: Springer, 2014.
- 18 S. H. Ko, C. P. Grigoropoulos, *Hierarchical Nanostructures for Energy Devices*, Cambridge: Royal Society of Chemistry, 2014.
- 19 S.-C. Tjong, *Nanocrystalline Materials: Their synthesis-structure-property relationships and applications*, Waltham: Elsevier, 2013.
- 20 W.-Q. Wu, B.-X. Lei, H.-S. Rao, Y.-F. Xu, Y.-F. Wang, C.-Y. Su, D.-B. Kuang, "Hydrothermal fabrication of hierarchically anatase TiO₂ nanowire arrays on FTO glass for dye-sensitized solar cells," *Sci. Rep.*, vol. 3, p. 1352, 2013.
- 21 S. Almajdalawi, V. Pavlinek, M. Mrlik, Q. Cheng, P. Piyamonacha, M. Pastorek, M. Stenicka, "Solvothermal synthesis of different TiO₂ morphology and their electrorheological characteristics," in *Journal of Physics: Conference Series*, 412, 2012.
- 22 M. Alzamani, A. Shokuhfar, E. Eghdam, S. Mastali, "Influence of catalyst on structural and morphological properties of TiO₂ nanostructured films prepared by sol-gel on glass," *Progress in Natural Science: Materials International*, vol. 23, no. 1, p. 77, 2013.
- 23 J.-M. Wu, "Low-temperature preparation of titania nanorods through direct oxidation of titanium with hydrogen peroxide," *Cryst. Growth.*, vol. 269, p. 347, 2004.
- 24 P. S. Shinde, C. H. Bhosale, "Properties of chemical vapour deposited nanocrystalline TiO₂ thin films and their use in dye-sensitized solar cells," *Journal of Analytical and Applied Pyrolysis*, vol. 82, p. 83, 2008.
- 25 L.-C. Jiang, W.-D. Zhang, "Electrodeposition of TiO₂ nanoparticles on multiwalled carbon nanotube arrays for hydrogen peroxide sensing," *Electroanalysis*, vol. 21, p. 988, 2009.
- 26 J. Guo, S. Zhu, Z. Chen, Y. Li, Z. Yu, Q. Liu, J. Li, C. Feng, D. Zhang, "Sonochemical synthesis of TiO₂ nanoparticles on graphene for use as photocatalyst," *Ultrasonics Sonochemistry*, vol. 18, no. 5, p. 1082, 2011.
- 27 X. Wang, J. Tian, C. Fei, L. Lv, Y. Wang, G. Cao, "Rapid construction of TiO₂ aggregates using microwave assisted synthesis and its application for dye-sensitized solar cells," *RSC Adv.*, vol. 5, p. 8622, 2015.
- 28 K. Byrappa, M. Yoshimura, *Handbook of Hydrothermal Technology*, Waltham: Elsevier, 2013.
- 29 W. Shockley, H. J. Queisser, "Detailed balance limit of efficiency of p-n junction solar cells," *J. Apply. Phys.*, vol. 32, p. 510, 1961.
- 30 National Renewable Energy Laboratory, "Research Cell Efficiency Records," 2012. [Online]. Available: http://www.nrel.gov/npv/images/efficiency_chart.jpg. [Accessed 01 September 2012].
- 31 National Instruments, 2012. [Online]. Available: <http://www.ni.com/white->

paper/7230/en/.

- 32 H. Tributsch, "Reaction of excited chlorophyll molecules at electrodes and in photosynthesis," *Photochem. Photobiol.*, vol. 16, p. 261, 1972.
- 33 N. Vlachopoulos, P. Liska, J. Augustynski, M. Graetzel, "Very efficient visible light energy harvesting and conversion by spectral sensitization of high surface area polycrystalline titanium dioxide films," *J. Am. Chem. Soc.*, vol. 110, p. 1216, 1988.
- 34 B. O'Regan, M. Grätzel, "A low cost high efficiency solar cell Based on dye sensitized colloidal TiO₂ films," *Nature*, vol. 353, p. 737, 1991.
- 35 A. Yella, H. W. Lee, H. N. Tsao, C. Yi, A. K. Chandiran, M. K. Nazeeruddin, E. W. Diau, C. Y. Yeh, S. M. Zakeeruddin, M. Grätzel, "Porphyrin-sensitized solar cells with cobalt (II/III)-based redox electrolyte exceed 12 percent efficiency," *Science*, vol. 334, p. 629, 2011.
- 36 J. Barber, B. Andersson, "Revealing the blueprint of photosynthesis," *Nature*, vol. 370, p. 31, 1994.
- 37 H.-Y. Chen, D.-B. Kuang, C.-Y. Su "Hierarchically micro/nanostructured photoanode materials for dye-sensitized solar cells," *J. Mater. Chem.*, vol. 20, p. 15475, 2012.
- 38 J. Barbe, F. Arendse, P. Comte, M. Jirousek, F. Lanzmann, V. Shklover, M. Grätzel, "Nanocrystalline titanium oxide electrodes for photovoltaic applications," *J. Am. Ceram. Soc.*, vol. 80, p. 3157, 1997.
- 39 Y. Kusumawati, "Oxide and composite electron transport layers for efficient dye-sensitized solar cells," Paris, 2015.
- 40 Y. V. Zubavichus, Y. L. Slovokhotov, M. K. Nazeeruddin, S. M. Zakeeruddin, M. Grätzel, V. Shklover, "Structural characterization of solar cell prototypes based on nanocrystalline TiO₂ anatase sensitized with Ru complexes. X-ray diffraction, XPS and XAFS spectroscopy study," *Chem. Mater.*, vol. 14, p. 3556, 2002.
- 41 M. Grätzel, "Conversion of sunlight to electric power by nanocrystalline dye-sensitized solar cells," *Journal of Photochemistry and Photobiology A: Chemistry*, vol. 164, p. 3, 2004.
- 42 L. Moreira Gonçalves, V. de Zea Bermudez, H. Aguilar Ribeiro, A. Magalhães Mendes, "Dye sensitized solar cells: A safe bet for the future," *Energy and Environmental Science*, vol. 1, p. 655, 2008.
- 43 A. Hagfeldt, M. Grätzel, "Molecular photovoltaics," *Acc. Chem. Res.*, vol. 33, p. 269, 2000.
- 44 J. Desilvestro, M. Graetzel, L. Kavan, J. Moser, J. Augustynski, "Highly efficient sensitization of titanium dioxide," *J. Am. Chem. Soc.*, vol. 107, p. 2988, 1985.
- 45 H. Wolpher, S. Sinha, J. Pan, A. Johansson, M. J. Lundqvist, P. Persson, R. Lomoth, J. Bergquist, L. Sun, V. Sundström, B. Akermark, T. Polívka, "Synthesis and electron transfer studies of ruthenium-terpyridine -based dyes attached to nanostructured TiO₂," *Inorganic Chem.*, vol. 46, p. 638, 2007.
- 46 T. Horiuchi, H. Miura, K. Sumioka, S. Uchida, "High efficiency of dye-sensitized solar cells based on metal free indoline dyes," *J. of Am. Chem. Soc.*, vol. 126, p. 12218, 2004.

- 47 G. Wolfbauer, A. M. Bond, J. C. Eklund, D. R. MacFarlane, "A channel flow cell system specifically design to test the efficiency of redox shuttles in dye sensitized solar cells," *Solar energy materials and solar cells*, vol. 70, p. 85, 2001.
- 48 Q. Li, X. Chen, J. Zhao, L. Qiu, Y. Zhang, B. Sun, F. Yan, "Organic ionic plastic crystal-based electrolytes for solid-state dye sensitized solar cells," *J. Mater. Chem.*, vol. 22, p. 6674, 2012.
- 49 W. Maiaugree, S. Lowpa, M. Towannang, P. Rutphonsan, A. Tangtrakarn, S. Pimanpang, P. Maiaugree, N. Ratchapolthavisin, W. Sang-aroon, W. Jarernboon, V. Amornkitbamrung, "A dye sensitized solar cell using natural counter electrode and natural dye derived from mangosteen peel waste," *Sci. Rep.*, vol. 5, no. 15230, 2015.
- 50 M. Grätzel, "Dye sensitized solar cells," *J. Photochem. Photobiol. C*, vol. 4, p. 145-, 2003.
- 51 Y. Li, H. Wang, Q. Feng, G. Zhou, Z.-S. Wang, "reduced graphene oxide–TaON composite as a high-performance counter electrode for $\text{Co}(\text{bpy})^{33+/2+}$ -mediated dye-sensitized solar cells," *ACS Appl. Mater. Interfaces*, vol. 16, p. 8217-, 2013.
- 52 R.-Y. Yao, Z.-J. Zhou, Z.-L. Hou, X. Wang, W.-H. Zhou, S.-X. Wu, "Surfactant-free CuInS_2 nanocrystals: an alternative counter-electrode material for dye-sensitized solar cells," *ACS Appl. Mater. Interfaces*, vol. 5, p. 3143, 2013.
- 53 M. M. Byranvand, A. N. Kharat, M. H. Bazargan "Titania nanostructures for dye-sensitized solar cells," *Nano Micro Letters*, vol. 4, p. 253, 2012.
- 54 H. Yu, S. Zhang, H. Zhao, B. Xue, P. Liu, G. Will, "High-performance TiO_2 photoanode with an efficient electron transport network for dye-sensitized solar cells," *J. Phys. Chem. C*, vol. 113, p. 16277, 2009.
- 55 S. F. Shaikh, R. S. Mane, B. K. Min, Y. J. Hwang, O.-s. Joo. "D-sorbitol-induced phase control of TiO_2 nanoparticles and its application for dye-sensitized solar cells," *Sci. Rep.*, vol. 6, 20103, 2016.
- 56 J. Wu, Z. Lan, S. Hao, P. Li, J. Lin, M. Huang, L. Fang, Y. Huang, "Progress on the electrolytes for dye-sensitized solar cells," *Pure Appl. Chem.*, vol. 80, p. 2241, 2008.
- 57 D. Zhao, T. Peng, L. Lu, P. Cai, P. Jiang, Z. Bian, "Effect of annealing temperature on the photoelectrochemical properties of dye-sensitized solar cells made with mesoporous TiO_2 nanoparticles," *The Journal of Physical Chemistry C*, vol. 112, p. 8486, 2008.
- 58 R. Katoh, A. Huijser, K. Hara, T. J. Savenije, L. D. A. Siebbeles, "effect of the particle size on the electron injection efficiency in dye-sensitized nanocrystalline TiO_2 films studied by time-resolved microwave conductivity (TRMC) measurements," *J. Phys. Chem. C*, vol. 111, p. 10741, 2007.
- 59 A. Tricoli, A. S. Wallerand, M. Righettoni, "Highly porous TiO_2 films for dye sensitized solar cells," *J. Mater. Chem.*, vol. 22, p. 14254, 2012.
- 60 A. Sedghi, H. N. Miankushki, "The effect of drying and thickness of TiO_2 electrodes on the photovoltaic performance of dye-sensitized solar cells," *Int. J. Electrochem. Sci.*, vol. 10, p. 3354, 2015.

- 61 S. Zhang, X. Yang, Y. Numata, L. Han, "Highly efficient dye-sensitized solar cells: progress and future challenges," *Energy Environ. Sci.*, vol. 6, p. 1443, 2013.
- 62 V. Baglio, M Girolamo, V. Antonucci, A. S. Arico, "Influence of TiO₂ film thickness on the electrochemical behaviour of dye-sensitized solar cells," *Int. J. Electrochem. Sci.*, No: 6 p. 3375, 2011.
- 63 P. M. Sommeling, B. C. O'Regan, R. R. Haswell, H. J. P. Smit, N. J. Bakker, J. J. T. Smits, J. M. Kroon, J. A. M. van Roosmalen "Influence of a TiCl₄ post-treatment on nanocrystalline TiO₂ films in dye-sensitized solar cells," *J. Phys. Chem. B*, vol. 110, p. 19191, 2006.
- 64 H. Choi, C. Nahm, Jo. Kim, J. Moon, S. Nam, D.-Ry. Jung, B. Park, "The effect of TiCl₄-treated TiO₂ compact layer on the performance of dye-sensitized solar cell," *Current Applied Physics*, vol. 12, p. 737. 2012.
- 65 C.-H. Tsai, Y.-T. Tsai, T.-W. Huang, Sui-Ying Hsu, Y.-F. Chen, Y.-H. Jhang, L. Hsieh, C.-C. Wu, Y.-S. Chen "Influences of stacking architectures of TiO₂ nanoparticle layers on characteristics of dye-sensitized solar cells," *Journal of Nanomaterials*, vol. 2013, p. 915461, 2013.
- 66 H. Liu, W. Jiang, L. Yin, Y. Shi, B. Chen, W. Jiang, Y. Ding, "Enhanced photovoltaic performance of dye-sensitized solar cells with TiO₂ micro/nano-structures as light scattering layer," *J Mater Sci: Mater Electron*, vol. 27, p. 5452, 2016.
- 67 N. Mir, K. Lee, I. Paramasivam, P. Schmuki, "Optimizing TiO₂ nanotube top geometry for use in dye-sensitized solar cells," *Chem. Eur. J.*, vol. 18, p. 11862, 2012.
- 68 H.-Y. Chen, T.-L. Zhang, J. Fan, D.-B. Kuang, C.-Y. Su, "Electrospun hierarchical TiO₂ nanorods with high porosity for efficient dye-sensitized solar cells," *ACS Appl. Mater. Interfaces*, vol. 5, p. 9205, 2013.
- 69 J. Huo, Y. Hu, H. Jiang, W. Huang, Y. Li, W. Shao, C. Li, "Mixed solvents assisted flame spray pyrolysis synthesis of TiO₂ hierarchically porous hollow spheres for dye-sensitized solar cells," *Ind. Eng. Chem. Res.*, vol. 53, p. 11029, 2013.
- 70 H.-J. Son, C. Prasittichai, J. E. Mondloch, L. Luo, J. Wu, D. W. Kim, O. K. Farha, J. T. Hupp, "Dye stabilization and enhanced photoelectrode wettability in water-based dye-sensitized solar cells through post-assembly atomic layer deposition of TiO₂," *J. Am. Chem. Soc*, vol. 135, p. 11529, 2013.
- 71 M. Lv, D. Zheng, M. Ye, J. Xiao, W. Guo, Y. Lai, L. Sun, C. Lin, J. Zuo, "Optimized porous rutile TiO₂ nanorod arrays for enhancing the efficiency of dye-sensitized solar cells," *Energy Environ. Sci.*, vol. 6, p. 1615, 2013.
- 72 M. Ye, D. Zheng, M. Lv, C. Chen, C. Lin, Z. Lin, "Hierarchically structured nanotubes for highly efficient dye-sensitized solar cells," *Advanced Materials*, vol. 25, p. 3039, 2013.
- 73 Y. Shi, C. Zhu, L. Wang, W. Li, K. K. Fung, N. Wang, "Asymmetric ZnO panel-like hierarchical architectures with highly interconnected pathways for free-electron transport and photovoltaic improvements," *Chemistry - A European Journal*, vol. 19, p. 282, 2012.

- 74 A. Bahramian, "High conversion efficiency of dye-sensitized solar cells based on coral-like TiO₂ nanostructured films: synthesis and physical characterization," *Ind. Eng. Chem. Res.*, vol. 52, p. 14837, 2013.
- 75 S.-C. Chiao, B. G. Bovard, H. A. Macload, "Repeatability of the composition of titanium oxide films produced by evaporation of Ti₂O₃," *Applied Optics*, vol. 37, p. 5284, 1998.
- 76 M. Levin, C. R. L Robbins, H. F. Mcmurdie, *Phase Diagrams for Ceramists*, M.K. Reser, Ed., Ohio: The American Ceramic Society, 1964.
- 77 H. Shi, R. Magaye, V. Castranova, J. Zhao, "Titanium dioxide nanoparticles: a review of current toxicological data," *Part Fibre Toxicol.*, vol. 10, 2013.
- 78 M. Grätzel, "Photoelectrochemical cells," *Nature*, vol. 414, p. 338, 2001.
- 79 A. Fujishima, K. Honda, "Electrochemical photolysis of water at a semiconductor electrode," *Nature*, vol. 238, p. 37, 1972.
- 80 M. Kurtoglu, "Effect of doping on the photocatalytic, electronic and the mechanical properties of sol-gel titanium dioxide films," Ph.D Thesis, Drexel University, 2011.
- 81 A. Fujishima, T. N. Rao, D. A. Tryk, "Titanium dioxide photocatalysis," *J. Photochem. Photobiol. C*, vol. 1, p. 1, 2000.
- 82 N. A. Dubrovinskaia, "Experimental and theoretical identification of a new high pressure TiO₂ polymorph," *Phys. Rev. Lett.*, vol. 87, p. 275501, 2001.
- 83 L. S. Dubrovinsky, "The hardest known oxide," *Nature*, vol. 410, p. 653, 2001.
- 84 R. Marchant, L. Brohan, M. Tournoux, "TiO₂ (B) a new form of titanium dioxide and the potassium octatitanate K₂Ti₈O₁₇," *Mater. Res. Bull.*, vol. 15, p. 1129, 1980.
- 85 S.-D. Mo, M. Y. Ching, "Electronic and optical properties of three phases of titanium dioxide: Rutile, anatase, and brookite," *PhRvB*, vol. 51, p. 13023, 1995.
- 86 M. Grätzel, "Solar energy conversion by dye-sensitized photovoltaic cells," *Inorg. Chem.*, vol. 44, p. 6841, 2005.
- 87 L. Linsebigler, G. Lu, J. T. Yates, "Photocatalysis of TiO₂ surface: principles, mechanisms, and selected results," *Chemical Reviews*, vol. 95, p. 735, 1995.
- 88 N. T. Nolan, "Sol-gel synthesis and characterization of novel metal oxide nanomaterials for photocatalytic applications," Ph.D Thesis, Dublin Institute of Technology, 2010.
- 89 K. Zakrzewska, "Nonstoichiometry in TiO_{2-y} studied by ion beam methods and photoelectron spectroscopy," *Advances in Materials Science and Engineering*, vol. 2012, p. 13, 2012.
- 90 U. Balachandran, N. G. Eror, "Electrical conductivity in nonstoichiometric titanium dioxide at elevated temperatures," *J. Mater. Sci.*, vol. 23, p. 2676, 1988.
- 91 M. Nowotny, "Defect disorder semiconducting properties and chemical diffusion of titanium dioxide single crystal," Ph.D Thesis, UNSW, 2006.
- 92 C. D. Valantine, G. Pacchioni, A. Selloni, "Origin of the different photoactivity of N-doped anatase and rutile TiO₂," *PhRvB*, vol. 70, p. 85116,

- 2004.
- 93 S. Iijima, "Helical microtubules of graphitic carbon," *Nature*, vol. 354, p. 56, 1991.
 - 94 D. V. Bavykin, J. M. Friedrich, F. C. Walsh, "Protonated titanates and TiO₂ nanostructured materials: Synthesis, properties, and applications," *Adv. Mater.*, p. 2807, 2006.
 - 95 D. V. Bavykin, F. C. Walsh, *Titanate and Titania Nanotubes: Synthesis, Properties and Applications*, Cambridge: Royal Society of Chemistry, 2010.
 - 96 T. Kasuga, M. Hiramatsu, A. Hoson, T. Sekino, K. Niihara, "Formation of titanium oxide nanotube," *Langmuir*, vol. 14, p. 3160, 1998.
 - 97 J. Boudon, A. L. Papa, J. Paris, N. Millot, "Titanate nanotubes as a versatile platform for nanomedicine," in *Nanomedicine*, One Central Press (OCP), A. Seifalian, A. De Mel, D. M. Kalaskar Ed., p. 403, 2014.
 - 98 L. Zhang, Q. Zhang, J. Li, "Layered titanate nanosheets intercalated with myoglobin for direct electrochemistry," *Advanced Functional Materials*, vol. 17, p. 1958, 2007.
 - 99 J. Li, Z. Tang, Z. Zhang, "Pseudocapacitive characteristic of lithium ion storage in hydrogen titanate nanotubes," *Chemical Physics Letters*, vol. 418, p. 506, 2006.
 - 100 Q. X. Deng, C. Z. Huang, W. Xie, H. C. Xu, M. D. Wei, "Synthesis and application of titanate nanotubes," *Applied Mechanics and Materials*, no. 331, p. 400, 2013.
 - 101 A. Turki, H. Kochkar, C. Guillard, G. Berhault, A. Ghorbel, "Effect of Na content and thermal treatment of titanate nanotubes on the photocatalytic degradation of formic acid," *Applied Catalysis B: Environmental*, vol. 139, p. 401, 2013.
 - 102 G. H. Jain, L. A. Patil, P. P. Patil, U. P. Mulik, K. R. Patil, "Studies on gas sensing performance of pure and modified barium strontium titanate thick film resistors," *Mater Sci*, vol. 30, p. 9, 2007.
 - 103 P. Hoyer, "Formation of a titanium dioxide nanotube array," *Langmuir*, vol. 12, p. 1411, 1996.
 - 104 J. C. Hulteen, C. R. Martin, "A general template-based method for the preparation of nanomaterials," *J. Mater. Chem.*, vol. 7, p. 1075, 1997.
 - 105 D. Gong, C. A. Grimes, O. K. Varghese, W. Hu, R. S. Singh, Z. Chen, E. C. Dickey, "Titanium oxide nanotube arrays prepared by anodic oxidation," *Journal of Materials Research*, vol. 16, p. 3331, 2001.
 - 106 Q. Chen, G. Du, S. Zhang, L. M. Peng, "The structure of trititanate nanotubes," *Acta Crystallogr.*, vol. 58, p. 587, 2002.
 - 107 G. H. Du, Q. Chen, R. C. Che, Z. Y. Yuan, L.-M. Peng "Preparation and structure analysis of titanium oxide nanotubes," *Appl. Phys. Lett.*, vol. 79, p. 3702, 2001.
 - 108 D. Wu, J. Liu, X. Zhao, A. Li, Y. Chen, N. Ming, "Sequence of events for the formation of titanate nanotubes, nanofibers, nanowires, and nanobelts," *Chem. Mater.*, vol. 18, p. 547, 2006.
 - 109 A. Bo, H. Zhan, J. Bell, H. Zhu, Y. Gu, "Mechanical bending properties of sodium titanate (Na₂Ti₃O₇) nanowires," *RSC Adv.*, vol. 4, p. 56970, 2014.

- 110 M. Zhang, Z. Jin, J. Zhang, X. Guo, J. Yang, W. Li, X. Wang, Z. Zhang, "Effect of annealing temperature on morphology, structure and photocatalytic behavior of nanotubed $\text{H}_2\text{Ti}_2\text{O}_4(\text{OH})_2$," *Journal of Molecular Catalysis A: Chemical*, vol. 217, p. 203, 2004.
- 111 S. Pavasupree, Y. Suzuki, S. Pivsa-Art, S. Yoshikawa, "Synthesis and characterization of nanoporous, nanorods, nanowires metal oxides," *Science and Technology of Advanced Materials*, vol. 6, p. 224, 2005.
- 112 D. V. Bavykin, V. N. Parmon, A. A. Lapkin, F. C. Walsh, "The effect of hydrothermal conditions on the mesoporous structure of TiO_2 nanotubes," *J. Mater. Chem.*, vol. 14, p. 3370, 2004.
- 113 W. Zhou, H. Liu, R. I. Boughton, G. Du, J. Lin, J. Wang, D. Liu, "One-dimensional single-crystalline Ti–O based nanostructures: properties, synthesis, modifications and applications," *J. Mater. Chem.*, vol. 20, p. 5993, 2010.
- 114 S. Zhang, L. M. Peng, Q. Chen, G. H. Du, G. Dawson, W. Z. Zhou, "Formation mechanism of $\text{H}_2\text{Ti}_3\text{O}_7$ nanotubes," *Phys. Rev. Lett.*, vol. 91, No: 25, 2003.
- 115 H.-H. Ou, S.-L. Lo, "Review of titania nanotubes synthesized via the hydrothermal treatment: Fabrication, modification, and application," *Separation and Purification Technology*, vol. 58, p. 179, 2007.
- 116 E. Morgado Jr., M. A. S. de Abreu, O. R. C. Pravia, B. A. Marinkovic, P. M. Jardim, F. C. Rizzo, A. S. Araújo, "A study on the structure and thermal stability of titanate nanotubes as a function of sodium content," *olid State Sciences*, vol. 8, p. 888, 2006.
- 117 Q. Zhang, L. Gao, J. Sun, and S. Zheng, "Preparation of long TiO_2 nanotubes from ultrafine rutile nanocrystals," *Chem. Lett.*, vol. 31, p. 226, 2002.
- 118 Z.-Y. Yuan, B.-L. Su, "Titanium oxide nanotubes, nanofibers and nanowires," *Colloids Surf. A*, vol. 5241, p. 173, 2004.
- 119 D. V. Bavykin, S. N. Gordeev, A. V. Moskalenko, A. A. Lapkin, F. C. Walsh, "Apparent two-dimensional behavior of TiO_2 nanotubes revealed by light absorption and luminescence," *J. Phys. Chem.*, vol. 109, p. 8565, 2005.
- 120 S. Ribbens, I. Caretti, E. Beyers, S. Zamani, E. Vinck, S. Van Doorslaer, P. Cool, "Unraveling the photocatalytic activity of multiwalled hydrogen trititanate and mixed-phase anatase/trititanate nanotubes: A combined catalytic and EPR Study," *J. Phys. Chem. C*, vol. 115, p. 2302, 2011.
- 121 H. Yu, J. Yu, B. Cheng, "Photocatalytic activity of the calcined H-titanate nanowires for photocatalytic oxidation of acetone in air," *Chemosphere*, vol. 66, p. 2050, 2007.
- 122 J. Qu, C. Lai, "One-dimensional TiO_2 nanostructures as photoanodes for dye-sensitized solar cells," *Journal of Nanomaterials*, vol. 2013, 762730 2013.
- 123 I. Tacchini, A. Ansón-Casaos, Y. Yu, M.T. Martínez, M. Lira-Cantu, "Hydrothermal synthesis of 1D TiO_2 nanostructures for dye sensitized solar cells," *Materials Science and Engineering B*, vol. 177, p. 19, 2012.
- 124 H. Yin, Y. Wada, T. Kitamura, S. Kambe, S. Murasawa, H. Mori, T. Sakata,

- S. Yanagida, "Hydrothermal synthesis of nanosized anatase and rutile TiO₂ using amorphous phase TiO₂," *J. Mater. Chem.*, vol. 11, p. 1694, 2001.
- 125 Z. R. Ismagilov, L. T. Tsikoza, N. V. Shikina, V. F. Zarytova, V. V. Zinoviev, N. Zagrebelnyi, "Synthesis and stabilization of nano-sized titanium dioxide," *Russian Chemical Reviews*, vol. 78, p. 873, 2009.
- 126 M. Cerna, C. Guillard, E. Puzenat, M. Vesely, P. Dzik, "Hydrothermal synthesis of TiO₂: influence of process conditions on photocatalytic activity," *International Journal of Chemical and Environmental Engineering*, vol. 2, 2011.
- 127 T.-D. N. Phan, H. D. Pham, T. V. Cuong, E. J. Kim, S. Kim, E. W. Shin, "A simple hydrothermal preparation of TiO₂ nanomaterials using concentrated hydrochloric acid," *Journal of Crystal Growth*, vol. 312, p. 79, 2009.
- 128 M. Ahmadi, M. R. Ghasemi, H. H. Rafsanjani, "Study of different parameters in TiO₂ nanoparticles formation," *Journal of Materials Science and Engineering*, vol. 5, p. 87, 2011.
- 129 J. Ovenstone, K. Yanagisawa, "Crystallization of anatase from amorphous titania using the hydrothermal technique: Effects of starting material and temperature," *J. Phys. Chem. B*, vol. 103, p. 7781, 1999.
- 130 S. T. Aruna, S. Tirosh, A. Zaban, "Nanosize rutile titania particle synthesis via a hydrothermal method without mineralizers," *J. Mater. Chem.*, vol. 10, p. 2388, 2000.
- 131 M. Andersson, L. Österlund, S. Ljungström, A. Palmqvist, "Preparation of nanosize anatase and rutile TiO₂ by hydrothermal treatment of microemulsions and their activity for photocatalytic wet oxidation of phenol," *J. Phys. Chem. B*, vol. 106, p. 10674, 2002.
- 132 J. N. Nian, H. Teng, "Hydrothermal synthesis of single-crystalline anatase TiO₂ nanorods with nanotubes as the precursor," *J Phys Chem B*, vol. 110, p. 4193, 2006.
- 133 S. Dai, Y. Wu, T. Sakai, Z. Du, H. Sakai, M. Abe, "Preparation of highly crystalline TiO₂ nanostructures by acid-assisted hydrothermal treatment of hexagonal-structured nanocrystalline titania/cetyltrimethylammonium bromide nanoskeleton," *Nanoscale Res Lett.*, vol. 5, p. 1829, 2010.
- 134 W. Zhou, X. Liu, J. Cui, D. Liu, J. Li, H. Jiang, J. Wang, H. Liu, "Control synthesis of rutile TiO₂ microspheres, nanoflowers, nanotrees and nanobelts via acid-hydrothermal method and their optical properties," *CrystEngComm*, vol. 13, p. 4557, 2011.
- 135 G. J. Wilson, G. D. Will, R. L. Frost, S. A. Montgomery, "Efficient microwave hydrothermal preparation of nanocrystalline anatase TiO₂ colloids," *J. Mater. Chem.*, vol. 12, p. 1787, 2002.
- 136 H. Wang, P. Liu, X. Cheng, P. Liu, L. Zheng, "Effect of surfactants on synthesis of TiO₂ nano-particles by homogeneous precipitation method," *Powder Technology*, vol. 188, p. 52, 2008.
- 137 Y. Dai, C. M. Cobley, J. Zeng, Y. Sun, Y. Xia, "Synthesis of anatase TiO₂ nanocrystals with exposed {001} facets," *Nano Lett.*, vol. 9, p. 2455, 2009.
- 138 X. Feng, K. Shankar, O. K. Varghese, M. Paulose, T. J. Latempa, C. A. Grimes, "Vertically aligned single crystal TiO₂ nanowire arrays grown

- directly on transparent conducting oxide coated glass: synthesis details and applications," *Nano Lett.*, vol. 8, p. 3781, 2008.
- 139 B. Liu, E. S. Aydil, "Growth of oriented single-crystalline rutile TiO₂ nanorods on transparent conducting substrates for dye-sensitized solar cells," *J. Am. Chem. Soc.*, vol. 131, p. 3985, 2009.
- 140 E. Hosono, S. Fujihara, K. Kakiuchi, H. Imai, "Growth of submicrometer-scale rectangular parallelepiped rutile TiO₂ films in aqueous TiCl₃ Solutions under hydrothermal conditions," *Am. Chem. Soc.*, vol. 126, p. 7790, 2004.
- 141 N. Erdogan, J. Park, A. Ozturk, "Hydrothermal synthesis of 3D TiO₂ nanostructures using nitric acid: Characterization and evolution mechanism," *Ceram. Int.*, vol. 42, p. 5985, 2016.
- 142 S. M. Klein, J. H. Choi, "Synthesis of rutile titania powders: agglomeration, dissolution, and reprecipitation phenomena," *J. Mater. Res.*, vol. 18, p. 1457, 2003.
- 143 A. Matthews, "The crystallization of anatase and rutile from amorphous titanium dioxide under hydrothermal condition," *American Mineralogist*, vol. 61, p. 419, 1976.
- 144 U. Diebold, "The surface science of titanium dioxide," *Surface Science Reports*, vol. 48, p. 53, 2003.
- 145 S. G. Kumar, K. S. R. K. Rao, "Polymorphic phase transition among the titania crystal structures in solution based approach: From precursor chemistry to nucleation process," *Nanoscale*, vol. 6, p. 11574, 2014.
- 146 J.-G. Li, T. Ishigaki, X. Sun, "Anatase, brookite, and rutile nanocrystals via redox reactions under mild hydrothermal conditions: phase-selective synthesis and physicochemical properties," *J. Phys. Chem. C*, vol. 111, p. 4969, 2007.
- 147 A. Pottier, C. Chanéac, E. Tronc, L. Mazerolles, J.-P. Jolivet, "Synthesis of brookite TiO₂ nanoparticles by thermolysis of TiCl₄ in strongly acidic aqueous media," *J. Mater. Chem.*, vol. 11, p. 1116, 2001.
- 148 I. Keesmann, "Zur hydrothermalen synthese von brookit," *Z. Anorg. Allg. Chem.*, vol. 346, p. 30, 1966.
- 149 E. Schwarzmann, K.-H. Ognibeni, "Notizen: Hydrothermale synthese von brookit TiO₂ / hydrothermal synthesis of brookite TiO₂," *Z. Naturforsch B*, vol. 29, p. 435, 1974.
- 150 T. Wakamatsu, T. Fujiwara, K. N. Ishira, P. H. Shingu, "Formation of brookite-type TiO₂ titania by mechanical alloying," *J. Jpn. Soc. Powder Powder Metall.*, vol. 48, p. 950, 2001.
- 151 K. Tomita, V. Petrykin, M. Kobayashi, M. Shiro, M. Yoshimura, M. Kakihana, "Water-soluble titanium complex for the selective synthesis of nanocrystalline brookite, rutile, and anatase by a hydrothermal method," *Angew. Chem. Int.*, vol. 45, p. 2378, 2006.
- 152 H.-B. Kim, H. Kim, W. I. Lee, D.-J. Jang, "Hierarchical mesoporous anatase TiO₂ nanostructures with efficient photocatalytic and photovoltaic performances," *J. Mater. Chem. A*, vol. 3, p. 9714, 2015.
- 153 T. Luttrell, S. Halpegamage, J. Tao, A. Kramer, E. Sutter, M. Batzill, "Why is anatase a better photocatalyst than rutile? - Model studies on epitaxial

- TiO₂ films," *Sci. Rep.*, vol. 4, No: 4043, 2014.
- 154 G. Veréb, T. Gyulavári, Zs. Pap, L. Baia, K. Mogyorósi, A. Dombi, K. Hernádi, "Visible light driven photocatalytic elimination of organic- and microbial pollution by rutile-phase titanium dioxides: new insights on the dynamic relationship between morpho-structural parameters and photocatalytic performance," *RSC Adv.*, vol. 5, p. 66636, 2015.
 - 155 L.-L. Lai, J.-M. Wu, "Hollow TiO₂ microspheres assembled with rutile mesocrystals: Low-temperature one-pot synthesis and the photocatalytic performance," *Ceram. Int.*, vol. 41, p. 12317, 2015.
 - 156 A. Zaleska-Medynska, "Doped-TiO₂: a review," *Recent Patents on Engineering*, vol. 2, p. 157, 2008.
 - 157 S. George, S. Pokhrel, Z. Ji, B. L. Henderson, T. Xia, L. Li, J. I. Zink, A. E. Nel, L. Mädler, "Role of Fe doping in tuning the band gap of TiO₂ for photo-oxidation induced cytotoxicity paradigm," *J Am Chem Soc.*, vol. 133, p. 11270, 2011.
 - 158 N. Erdogan, J. Park, A. Ozturk, "Synthesis and enhanced photocatalytic activity of molybdenum, iron, and nitrogen triple-doped titania nanopowders," *Ceram. Int.*, vol. 42, p. 16766, 2016.
 - 159 K. Karthik, S. K. Pandian, N. V. Jaya, "Effect of nickel doping on structural, optical and electrical properties of TiO₂ nanoparticles by sol-gel method," *App. Surf. Sci.*, vol. 256, p. 6829, 2010.
 - 160 B. Choudhury, A. Choudhury, "Luminescence characteristics of cobalt doped TiO₂ nanoparticles," *Journal of Luminescence*, vol. 132, p. 178, 2012.
 - 161 R. Ren, Z. Wen, S. Cui, Y. Hou, X. Guo, J. Chen, "Controllable Synthesis and Tunable Photocatalytic Properties of Ti³⁺-doped TiO₂," *Sci. Rep.*, vol. 5, No: 10714, 2015.
 - 162 T. Ohno, M. Akiyoshi, T. Umebayashi, K. Asai, T. Mitsui, M. Matsumura "Preparation of S-doped TiO₂ photocatalysts and their photocatalytic activities under visible light," *Applied Catalysis A: General*, vol. 265, p. 115, 2004.
 - 163 M. Faraji, M. Sabzali, S. Yousefzadeh, N. Sarikhani, A. Ziashahabi, M. Zirak, A. Z. Moshfegh, "Band engineering and charge separation in the Mo_{1-x}W_xS₂/TiO₂ heterostructure by alloying: first principle prediction," *RSC Adv.*, vol. 5, p. 28460, 2015.
 - 164 A. E. Pirbazari, "Sensitization of TiO₂ nanoparticles with cobalt phthalocyanine: an active photocatalyst for degradation of 4-Chlorophenol under visible light," *Procedia Materials Science*, vol. 11, p. 622, 2015.
 - 165 G. Feng, S. Liu, Z. Xiu, Y. Zhang, J. Yu, Y. Chen, P. Wang, X. Yu, "Visible light photocatalytic activities of TiO₂ nanocrystals doped with upconversion luminescence agent," *J. Phys. Chem. C*, vol. 112, p.13692, 2008.
 - 166 S. Sato, "Photocatalytic activity of NO_x-doped TiO₂ in the visible light region," *Chem Phys Lett*, vol. 123, p. 126, 1986.
 - 167 R. Asahi, T. Morikawa, T. Ohwaki, K. Aoki, Y. Taga, "Visible-light photocatalysis in nitrogen-doped titanium dioxide," *Science*, vol. 193, p. 269, 2001.
 - 168 H. Yu, X. Zheng, Z. Yin, F. Tag, B. Fang, K. Hou, "Preparation of nitrogen-

- doped TiO₂ nanoparticle catalyst and its catalytic activity under visible light," *Chin. J. Chem. Eng.*, vol. 15, p. 802, 2007.
- 169 C. Burda, Y. Lou, X. Chen, J. L. Gole, "Enhanced nitrogen doping in TiO₂ nanoparticles," *Nano Letters*, vol. 3, p. 1049, 2003.
- 170 A. Khataee, G. A. Mansoori, Nanostructured titanium dioxide materials: properties, preparation and applications, Singapore: World Scientific, 2012.
- 171 C. Shifu, C. Lei, G. Shen, C. Gengyu, "The preparation of nitrogen-doped photocatalyst TiO_{2-x}N_x by ball milling," *Chemical Physics Letters*, vol. 413, p. 404, 2005.
- 172 F. Spadavecchia, G. Cappelletti, S. Ardizzone, M. Ceotto, L. Falciola, "Electronic structure of pure and N-Doped TiO₂ nanocrystals by electrochemical experiments and first principles calculations," *J. Phys. Chem. C*, vol. 115, p. 6381, 2011.
- 173 M. V. Dozzi, E. Selli, "Doping TiO₂ with p-block elements: Effects on photocatalytic activity," *Journal of Photochemistry and Photobiology C: Photochemistry Reviews*, p. 13, 2013.
- 174 O. Ola, M. M. Maroto-Valer, "Transition metal oxide based TiO₂ nanoparticles for visible light induced CO₂ photoreduction," *App. Catal. A: General*, vol. 502, p. 114, 2015.
- 175 H. Yan, X. Wang, M. Yao, X. Yao, "Band structure design of semiconductors for enhanced photocatalytic activity: The case of TiO₂," *Progress in Natural Science: Materials International*, vol. 23, p. 402, 2013.
- 176 Y. Gai, J. Li, S. S. Li, J. B. Xia, S. H. Wei, "Design of narrow-gap TiO₂: a passivated codoping approach for enhanced photoelectrochemical activity," *Phys. Rev. Lett*, vol. 102, 0336402, 2009.
- 177 A. Kubacka, B. Bachiller-Baeza, G. Colón, M. Fernández-García, "Doping level effect on sunlight-driven W, N-co-doped TiO₂-anatase photo-catalysts for aromatic hydrocarbon partial oxidation," *Applied Catalysis B: Environmental*, vol. 93, p. 274, 2010.
- 178 H. Liu, Z. Lu, L. Yue, R. Xiong, "(Mo + N) codoped TiO₂ for enhanced visible-light photoactivity," *Applied Surface Science*, vol. 257, p. 9355, 2011.
- 179 W.-J. Yin, H. Tang, S.-H. Wei, M. M. Al-Jassim, J. Turner, Y. Yan, "Band structure engineering of semiconductors for enhanced photoelectrochemical water splitting: The case of TiO₂," *Phys. Rev. B*, vol. 82, 045106, 2010.
- 180 R. Long, N. J. English, "First-principles calculation of nitrogen-tungsten codoping effects on the band structure of anatase-titania," *Appl. Phys. Lett.*, vol. 94, 132102, 2009.
- 181 M. Zhang, J. Wu, J. Hou, J. Yang, "Molybdenum and nitrogen Co-Doped titanium dioxide nanotube arrays with enhanced visible light photocatalytic activity," *Science of Advanced Materials*, vol. 5, p. 535, 2013.
- 182 H. Liu, R. Xiong, "Photocatalytic activity of Mo+Fe Co-doped titanium dioxide nanoparticles prepared by sol-gel method," *Journal of Wuhan University of Technology-Mater Sci Ed*, vol. 28, p. 44, 2013.
- 183 T.-H. Kim, V. Rodríguez-González, G. Gyawali, S.-H. Cho, T. Sekino, S.-W. Lee, "Synthesis of solar light responsive Fe, N co-doped TiO₂

- photocatalyst by sonochemical method," *Catalysis Today*, vol. 212, p. 75, 2013.
- 184 Z. Sun, J. H. Kim, Y. Zhao, D. Attard, S. X. Dou, "Morphology-controllable 1D-3D nanostructured TiO₂ bilayer photoanodes for dye-sensitized solar cells," *Chem Commun (Camb)*, vol. 49, p. 966, 2013.
- 185 C. B. Song, Y. H. Qiang, Y. L. Zhao, X. Q. Gu, L. Zhu, J. Song, X. Liu, "Dye-sensitized solar cells based on graphene-TiO₂ nanoparticles/TiO₂ nanotubes composite films," *Int. J. Electrochem. Sci.*, vol. 9, p. 8090, 2014.
- 186 P. Zhang, Z. Hu, Y. Wang, Y. Qin, W. Li, J. Wang, "A bi-layer composite film based on TiO₂ hollow spheres, P25 and multi-walled carbon nanotubes for efficient photoanode of dye-sensitized solar cell," *Nano-Micro Letters*, vol. 8, p. 232, 2016.
- 187 L. Yang, W. W.-F. Leung, "Application of a bilayer TiO₂ nanofiber photoanode for optimization of dye-sensitized solar cells," *Adv. Mater.*, vol. 23, 2011.
- 188 S. S. Mali, H. Kim, C. S. Shim, W. R. Bae, N. L. Tarwal, S. B. Sadale, P. S. Patil, Jin-H. Kim, C. K. Hong, "Single-step synthesis of 3D nanostructured TiO₂ as a scattering layer for vertically aligned 1D nanorod photoanodes and their dye-sensitized solar cell properties," *CrystEngComm*, vol. 15, p. 5660, 2013.
- 189 E. Parvazian, F. Karimzadeh, M. H. Enayati, "Photovoltaic characterization and electrochemical impedance spectroscopy analysis of dye-sensitized solar cells based on composite TiO₂-MWCNT photoelectrodes," *Journal of Electronic Materials*, vol. 43, p. 1450, 2014.
- 190 M. Wang, S. Zhang, Z. F. Du, L. D. Sun, D. L. Zhao, "Novel dye-sensitized solar cell architecture using TiO₂-coated Ag nanowires array as photoanode," *Rare Met.*, vol. 1, p. 1, 2015.
- 191 H.-N. Kim, J. H. Moon, "Enhanced photovoltaic properties of Nb₂O₅-coated TiO₂ 3D ordered porous electrodes in dye-sensitized solar cells," *ACS Appl. Mater. Interfaces*, vol. 4, p. 5821, 2012.
- 192 J. Lin, Y. Peng, A. R. Pascoe, F. Huang, Y.-B. Cheng, Y.-U. Heo, A. Nattestad, W. Seung, S. K. Kim, H. J. Yoon, S.-W. Kim, Y. Yamauchi, S. X. Dou, J. H. Kim, "A bi-layer TiO₂ photoanode for highly durable, flexible dye-sensitized solar cells," vol. 3, p. 4679, 2015.
- 193 W. Song, Y. Gong, J. Tian, G. Cao, H. Zhao, C. Sun, "Novel photoanode for dye-sensitized solar cells with enhanced light-harvesting and electron-collection efficiency," *ACS Appl. Mater. Interfaces*, vol. 8, p. 13418, 2016.
- 194 H. Wang, B. Wang, J. Yu, Y. Hu, C. Xia, J. Zhang, R. Liu, "Significant enhancement of power conversion efficiency for dye sensitized solar cell using 1D/3D network nanostructures as photoanodes," *Sci. Rep.*, vol. 5, 9305, 2015.
- 195 Y. Chen, Z. Chen, "Three-dimensional ordered TiO₂ hollow spheres as scattering layer in dye-sensitized solar cells," *Applied Physics A*, vol. 122, p. 195, 2016.
- 196 X. Lü, X. Mou, J. Wu, D. Zhang, L. Zhang, F. Huang, F. Xu, S. Huang, "Improved-performance dye-sensitized solar cells using Nb-doped TiO₂

- electrodes: Efficient electron injection and transfer," *Adv. Funct. Mater.*, vol. 20, p. 509, 2010.
- 197 Ji. Yu, Y. Yang, R. Fan, H. Zhang, L. Li, L. Wei, Y. Shi, K. Pan, H. Fu, "Er³⁺ and Yb³⁺ co-doped TiO_{2-x}F_x up-conversion luminescence powder as a light scattering layer with enhanced performance in dye sensitized solar cells," *J. Power Sources*, vol. 243, p. 436, 2013.
- 198 A. E. Shalan, M. M. Rashad, "Incorporation of Mn²⁺ and Co²⁺ to TiO₂ nanoparticles and the performance of dye-sensitized solar cells," *Applied Surface Science*, vol. 283, p. 975, 2013.
- 199 Y. Duan, N. Fu, Q. Zhang, Y. Fang, X. Zhou, Y. Lin, "Influence of Sn source on the performance of dye-sensitized solar cells based on Sn-doped TiO₂ photoanodes: A strategy for choosing an appropriate doping source," *Electrochimica Acta*, vol. 107, p. 473, 2013.
- 200 B. Roose, S. Pathak, U. Steiner, "Doping of TiO₂ for sensitized solar cells," *Chem. Soc. Rev.*, vol. 44, p. 8326, 2015.
- 201 S. P. Lim, A. Pandikumar, H. N. Lim, R. Ramaraj, N. M. Huang, "Boosting photovoltaic performance of dye-sensitized solar cells using silver nanoparticle-decorated N, S-Co-Doped-TiO₂ photoanode," *Sci. Rep.*, vol. 5, 11922, 2015.
- 202 S. K. Park, T. K. Yun, J. Y. Bae, "Fabrication N, F, and N/F-doped TiO₂ photoelectrodes for dye-sensitized solar cells," *J. Nanosci. Nanotech.*, vol. 15, p. 5967, 2015.
- 203 S. K. Park, J. S. Jeong, T. K. Yun, J. Y. Bae, "Preparation of carbon-doped TiO₂ and its application as a photoelectrodes in dye-sensitized solar cells," *J Nanosci Nanotechnol.*, vol. 2, p. 1529, 2015.
- 204 H. Su, Y.-T. Huang, Y.-H. Chang, P. Zhai, N. Y. Hau, P. Chun H. Cheung, W.-T. Yeh, T.-C. Wei, S.-P. Feng "The synthesis of Nb-doped TiO₂ nanoparticles for improved-performance dye sensitized solar cells," *Electrochimica Acta*, vol. 182, p. 230, 2015.
- 205 K. H. Ko, Y. C. Lee, Y. J. Jung, "Enhanced efficiency of dye-sensitized TiO₂ solar cells (DSSC) by doping of metal ions," *J. Colloid Interface Sci.*, vol. 283, p. 482, 2005.
- 206 S. Ito, P. Chen, P. Comte, M. K. Nazeeruddin, P. Liska, P. Péchy, M. Grätzel, "Fabrication of screen-printing pastes from TiO₂ powders for dye-sensitized solar cells," *Prog. Photovolt: Res. Appl.*, vol. 15, p. 603, 2007.
- 207 C. M. Ronconi, E. C. Pereira, "Electrocatalytic properties of Ti/TiO₂ electrodes prepared by the Pechini method," *Journal of Applied Electrochemistry*, vol. 31, p. 319, 2001.
- 208 Q. Wang, J.-E. Moser, M. Grätzel, "Electrochemical impedans spectroscopic analysis of dye-sensitized solar cells," *J. Phys. Chem. B*, vol. 109, p. 14945, 2005.
- 209 H. Lu, Y. Wang, Y. Wang, W. Liang, J. Yao, "Adjusting phase transition of titania-based nanotubes via hydrothermal and post treatment," *RSC Adv.*, vol. 5, p. 89777, 2015.
- 210 H. Lu, J. Zhao, L. Li, J. Zheng, L. Zhang, L. Gong, Z. Wang, Z. Zhu, "A systematic study on evolution mechanism of titanate nanostructures in the

- hydrothermal process," *Chemical Physics Letters*, vol. 508, p. 258, 2011.
- 211 V. Bellat, R. Chassagnon, O. Heintz, L. Saviot, D. Vandroux, N. Millot, "A multi-step mechanism and integrity of titanate nanoribbons," *Dalton Trans.*, vol. 44, p. 1150, 2015.
- 212 M. Motazari-Pour, N. Riahi-Noori, A. Mehdikhani, "Synthesis of single-phase anatase TiO₂ nanoparticles by hydrothermal treatment with application potential for photoanode electrodes of dye sensitized solar cells," *Journal of Ceramic Processing Research*, vol. 14, p. 595, 2013.
- 213 L. Shen, N. Bao, Y. Zheng, A. Gupta, T. An, K. Yanagisawa, "Hydrothermal splitting of titanate fibers to single-crystalline TiO₂ nanostructures with controllable crystalline phase, morphology, microstructure, and photocatalytic activity," *J. Phys. Chem. C*, vol. 12, p. 8809, 2008.
- 214 S. S. Mali, C. A. Betty, P. N. Bhosale, R. S. Devan, Y. R. Ma, S. S. Kolekar, P. S. Patil, "Hydrothermal synthesis of rutile TiO₂ nanoflowers using Brønsted acidic ionic liquid [BAIL]: synthesis, characterization and growth mechanism," *CrystEngComm*, vol. 14, p. 1920, 2012.
- 215 P. K. Schelling, N. Yu, J. W. Halley, "Self-consistent tight-binding atomic-relaxation model of titanium dioxide," *Phys. Rev. B*, vol. 58, p. 1279, 1998.
- 216 W.-J. Yin, S. Chen, J.-H. Yang, X.-G. Gong, Y. Yan, and S.-H. Wei, "Effective band gap narrowing of anatase TiO₂ by strain along a soft crystal direction," *App. Phys. Lett.*, vol. 96, 221901, 2010.
- 217 S.-Y. Luo, B.-X. Yan, J. Shen, "Enhancement of photoelectric and photocatalytic activities: Mo doped TiO₂ thin films deposited by sputtering," *Thin Solid Films*, vol. 522, p. 361, 2012.
- 218 J. Liu, S. Yang, W. Wu, Q. Tian, S. Cui, Z. Dai, F. Ren, X. Xiao, C. Jiang, "3D flowerlike α -Fe₂O₃@TiO₂ core-shell nanostructures: General synthesis and enhanced photocatalytic performance," *ACS Sustainable Chem.*, vol. 3, p. 2975, 2015.
- 219 W. Li, X. Liu, H. Li, "Hydrothermal synthesis of graphene/Fe³⁺-doped TiO₂ nanowire composites with highly enhanced photocatalytic activity under visible light irradiation," *J. Mater. Chem.*, vol. 3, p. 15214, 2015.
- 220 Y. Cong, J. Zhang, F. Chen, M. Anpo, D. He, "Preparation, photocatalytic activity, and mechanism of nano-TiO₂ Codoped with nitrogen and iron (III)," *J. of Phys. Chem. C*, vol. 111, p. 10618, 2007.
- 221 R. Quesada-Cabrera, C. Sotelo-Vazquez, J. C. Bear, J. A. Darr, I. P. Parkin, "Photocatalytic evidence of the rutile-to-anatase electron transfer in titania," *Adv. Mater. Interfaces*, vol. 1, 1400069, 2014.
- 222 I. A. Perales-Martínez, V. Rodríguez-González, S.-W. Lee, S. Obregón, "Facile synthesis of InVO₄/TiO₂ heterojunction photocatalysts with enhanced photocatalytic properties under UV-vis irradiation," *J. Photochem. Photobiol. A*, vol. 299, p. 152, 2015.
- 223 M. Lu, C. Shao, K. Wang, N. Lu, X. Zhang, P. Zhang, M. Zhang, X. Li, Y. Liu, "p-MoO₃ Nanostructures/n-TiO₂ nanofiber heterojunctions: Controlled fabrication and enhanced photocatalytic properties," *Appl. Mater. Interfaces*, vol. 6, p. 9004, 2014.
- 224 S. Kambe, S. Nakade, Y. Wada, T. Kitamura, S. Yanagida, "Effects of

- crystal structure, size, shape and surface structural differences on photo-induced electron transport in TiO₂ mesoporous electrodes," *J. Mater. Chem.*, vol. 12, p. 723, 2002.
- 225 Z. Shen, G. Wang, H. Tian, J. Sunarso, L. Liu, J. Liu, S. Liu, "Bi-layer photoanode films of hierarchical carbon-doped brookite-rutile TiO₂ composite and anatase TiO₂ beads for efficient dye-sensitized solar cells," *Electrochimica Acta*, vol. 216, p. 429, 2016.
- 226 S. Wang, X. Zhang, G. Zhou, Z. S. Wang, "Double-layer coating of SrCO₃/TiO₂ on nanoporous TiO₂ for efficient dye-sensitized solar cells," *Phys. Chem. Chem. Phys.*, vol. 14, p. 816, 2012.
- 227 K. Zhu, N. Kopidakis, N. R. Neale, J. van de Lagemaat, A. J. Frank, "Influence of surface area on charge transport and recombination in dye-sensitized TiO₂ solar cells," *J. Phys. Chem. B*, vol. 110, p. 25174, 2006.

CURRICULUM VITAE

Nursev Erdoğan
Research&Teaching Assistant

Personal Information

Name : Nursev Erdogan **Lab Phone** : +90 (312) 210 78 91
Date of Birth : April 26, 1987 **Lab Fax** : +90 (312) 210 25 18
Gender : Female **Email** : nursevbilgin@gmail.com
Marital Status : Married
Driving Licence : B

Education

Ph.D, Metallurgical and Materials Engineering, METU (2011-2017).
Thesis Title: Hydrothermal synthesis of TiO₂ nanostructures for photocatalytic and photovoltaic applications

Master of Science, Metallurgical and Materials Engineering, YTU (2008-2010).
Thesis Title: Utilizing marble dust as additive in construction materials

Bachelor of Science, Metallurgical and Materials Engineering, YTU (2004-2008).

Work Experience

2011- On going METU, Research & Teaching Assistant
09.2009-10.2010 Tubitak MAM, Visiting Researcher
Summer Practice (2007) Mercedes Benz Turk, Intern
Summer Practice (2006) Erbakır Bakır mamuller A.Ş., Intern

Assisted Courses

- Mete206 – Materials Laboratory

- Mete215 – Materials Laboratory
- Mete208 – Chemical Principles of Materials
- Mete227 – Basic Concepts in Material Science
- Mete230 – Fundamentals of Materials Science and Engineering
- Mete306 – Chemical Metallurgy
- Mete451 – Ceramic Materials
- Mete478 – Non-destructive Testing of Materials
- Mete544 – Properties of Glasses
- SEM and XRD Operator

Skills

Language

- Turkish (Native)
- English (Advanced)
- German (Beginner)

Research Interests

- Wet chemical synthesis of semiconductor oxides
- Fabrication of dye sensitized solar cells
- Perovskite based solar cells
- Material characterization

Structural Characterization

- Conventional X-Ray diffraction analysis methods
- Rietveld refinement
- X-Ray photoelectron spectroscopy

Electron Microscopy

- Scanning electron microscopy.
- Transmission electron microscopy.

Mechanical Characterization

- Tensile and compressive test.

Electrochemical and Photovoltaic Characterization

- Impedans Spectroscopy.
- Solar simulator efficiency analysis

Softwares

- Operating System: Microsoft Windows, Mac OS.
- Office: MS Word, MS Excel, MS Powerpoint.
- Image Analysis: Adobe Photoshop CS5, ImageJ.

- Data Analysis: OriginLab, Minitab, Sigma Plot.
- Other: Carine, GSAS & EXPGUI, Digital Micrograph.

Conferences

- Erdogan, N., Park, J., Ozturk, A., “Synthesis of Molybdenum and Iron Co-Doped Nano Titania Powders By Hydrothermal Method and Their Enhanced Photocatalytic Activities”, New Trends In Solar Cells, Bratislava, Slovak Republic, 19-22 April 2016 (Oral presentation).
- Bilgin, N., Agartan, L., Park, J., Ozturk, A., “Synthesis of TiO₂ Nano-Structures via Hydrothermal Method”: “Healthcare & Electronics II”, Nanotechnology for Energy, Environment, Electronics, and Industry Symposium of MS&T’14, Pittsburg, PA, USA 12-16 October 2014 (Oral presentation).
- Bilgin, N., Park, J., Ozturk, A., “Production of TiO₂ nano-powders in various morphologies via hydrothermal method ” 17th International Metallurgy & Materials Congress, İstanbul, Turkey 11-13 September 2014 (Oral presentation).
- Bilgin, N., Park, J., Ozturk, A., “Investigation of the effect of porosities on the efficiency of DSSCS produced by using nano-sized TiO₂”, 37th International Conference and Expo on Advanced Ceramics and Composites, Daytona Beach, FL, USA 27 January-1 February 2013 (Oral presentation).
- Bilgin, N., Yeprem, H. A., Marsoglu, M., “Investigation of evaluating waste marble dust in construction industry”, 13th International Conference of the European Ceramic Society (ECERS XIII)”, Lemoge, France, 23-27 June, 2013 (Poster presentation).

Publications

- Erdogan, N., Ozturk, A., Park, J., 2016, “Synthesis and enhanced photocatalytic activity of molybdenum, iron, and nitrogen triple-doped titania nanopowders”, *Ceramics International*, 42, 15, pp. 16766–16774.
- Erdogan, N., Ozturk, A., Park, J., 2016, “Hydrothermal synthesis of 3D TiO₂ nanostructures using nitric acid: Characterization and evolution mechanism”, *Ceramics International*, 42, 5, pp. 5985–5994.
- Bilgin, N., Agartan, L., Jongee, P., Ozturk, A., 2015, “Synthesis of TiO₂ nanostructures via hydrothermal method”, *Advances in Materials Science for Environmental and Energy Technologies IV: Ceramic Transactions*, 253, pp. 177-186. ISBN: 978-1-119-19025-7.
- Bilgin, A., Yuceturk, G., Arslan, S., Bilgin, N., Polat S., 2013, “The effects of mineralogical and petrographical features of the Lake District rocks (Isparta, Turkey) on the quality of artificial marbles”, *Építőanyag*, 1, 21.

- Bilgin, N., Park, J., Ozturk, A., 2013, “Influence of particle size of TiO₂ powder on the energy conversion efficiency of dye-sensitized solar cell”, *Advanced Materials Research*, 650, pp. 39-43.
- Bilgin, N., Yeprem, H. A., Arslan, S., Bilgin., A., Gunay, E., Marsoglu, M., 2012, “Use of waste marble powder in brick industry”, *Construction and Building Materials*, 29, pp. 449-457.
- Bilgin, N., Yeprem, H. A., Günay, E., Marsoğlu, M., 2011, “Evaluating waste marble dust as floor tile”, *Materials Testing* 53, 5, pp. 290-294.

References

Dr. Abdullah Öztürk

Middle East Technical University
Metallurgical and Materials
Engineering Department E-220.
Phone: +90-312-210-59-32

Dr. Jongee Park

Atilim University Metallurgical and
Materials Engineering Department C-
111.
Phone : +90-312-586-83-21

Dr. H. Aygül Yeprem

Yildiz Technical University
Metallurgical and Materials
Engineering Department.
Phone: +90-212-449-16-59